Nano Structured Materials Studied by Coherent X-ray Diffraction

Dissertation
zur Erlangung des Doktorgrades
des Department Physik
der Universität Hamburg

vorgelegt von
Johannes Gulden

Hamburg
2013

Gutachter der Dissertation:	Prof. Dr. E. Weckert Prof. Dr. I. A. Vartaniants
Gutachter der Disputation:	Prof. Dr. E. Weckert Prof. Dr. H. N. Chapman
Datum der Disputation:	February 15th, 2013
Vorsitzender des Prüfungsausschusses:	Prof. Dr. G. Huber
Vorsitzender des Promotionsausschusses:	Prof. Dr. P. Hauschildt
Dekan der Fakultät MIN:	Prof. Dr. H. Graener

Abstract

Structure determination with X-rays in crystallography is a rapidly evolving field. Crystallographic methods for structure determination are based on the assumptions about the crystallinity of the sample. It is vital to understand the structure of possible defects in the crystal, because they can influence the structure determination. All conventional methods to characterize defects require a modelling through simulated data. No direct methods exist to image the core of defects in crystals. Here a new method is proposed, which will enable to visualize the individual scatterers around and at defects in crystals. The method is based on coherent X-ray scattering.

X-rays are perfectly suited since they can penetrate thick samples and buried structures can be investigated Recent developments increased the coherent flux of X-Ray sources such as synchrotrons by orders of magnitude. As a result, the use of the coherent properties of X-rays is emerging as a new aspect of X-ray science. New upcoming and operating X-ray laser sources will accelerate this trend. One new method which has the capacity to recover structural information from the coherently scattered photons is Coherent X-ray Diffraction Imaging (CXDI).

The main focus of this thesis will be the investigation of the structure and the dynamics of colloidal crystals. Colloidal crystals can be used as a model for atomic crystals in order to understand the growth and defect structure. Despite the large interest in these structures, many details are still unknown.Therefore, it is vital to develop new approaches to measure the core of defects in colloidal crystals. After an introduction in into the basics of the field of coherent X-ray scattering, this thesis will introduce a novel method, Small Angle Bragg Coherent Diffractive Imaging, (SAB-CDI) in chapter two. This new measurement technique which besides the relevance to colloidal crystals can be applied to a large variety of nano structured materials. To verify the experimental possibilities the third chapter will focus on experiments carried out at synchrotron sources showing the potential of applying SAB-CDI to colloidal crystals. An experiment on GaAs nano wires proves the prospects of this method for other nano structured materials. To investigate dynamics, especially on the ultrafast time scale, FEL sources are needed. The fourth chapter will therefore present two experiments performed at the FLASH facility in Hamburg, showing that SAB-CDI can also be applied at FELs on an artificial crystal and an experiment performed on colloidal crystals to investigate the ultra fast dynamics with a pump-probe experiment.

The technical advances in synchrotron radiation creation have opened the field to applications with the coherent part of the X-rays. The combination of iterative phase retrieval methods with crystallographic methods yields the unique opportunity to measure the internal structure of nano structured samples. This thesis will give an introduction into this exciting new field.

Zusammenfassung

Strukturbestimmungen mit Röntgenstrahlen stellen ein sich schnell entwickelndes Feld der Kristallographie dar. Die Methoden basieren auf Annahmen über die Kristalleigenschaften der zu untersuchenden Proben. Daher ist es entscheidend die Struktur möglicher Fehler im Kristallgitter zu verstehen. Alle üblichen Methoden zur Charakterisierung von Fehlern im Kristall benötigen eine Modellbildung auf Basis simulierter Daten. Hier wird eine neue Methode vorgeschlagen, welche es ermöglicht die individuellen Streuquellen rund um den Fehler im Kristallgitter direkt zu visualisieren. Die Methode basiert auf der Streuung kohärenter Röntgenstrahlen, welche sich hierfür, auf Grund ihrer hohen Eindringtiefe, hervorragend eignen.

Neuste Entwicklungen haben den Fluss kohärenter Röntgenstrahlen an Synchrotronquellen um mehrere Größenordnungen erhöht. Dadurch wurde die Anwendung der Kohärenzeigenschaften von Röntgenstrahlen ermöglicht. Die Nutzung von Röntgenlasern wird diesen Trend weiter beschleunigen. Eine der neuen Methoden, welche die Möglichkeit hat strukturelle Eigenschaften aus den gestreuten kohärenten Photonen abzuleiten, ist "Coherent X-ray Diffraction Imaging" (CXDI).

Das Schwerpunkt dieser Arbeit liegt in der Untersuchung der Struktur und der Dynamik von Kolloidkristallen. Kolloidkristalle eignen sich als Modelle für atomare Kristalle, um Wachstum und Kristallfehler zu verstehen. Daher ist es entscheidend, neue Herangehensweisen zu entwickeln, um den Kern der Störstelle zu untersuchen.

Nach einer Einführung in die Grundlagen der kohärenten Röntgenstreuung wird in dieser Arbeit eine neue Methode vorgestellt: "Small Angle Bragg Coherent Diffractive Imaging" (SAB-CDI). Dieses neue Messverfahren lässt sich auf eine Vielfalt von Materialien anwenden, welche auf der Nano-Ebene strukturiert sind. Um die experimentellen Möglichkeiten zu zeigen werden Experimente vorgestellt, welche an Synchrotronstrahlungsquellen an Kolloidkristallen gemessen wurden. Ein weiteres Experiment an GaAs Nano-Drähten belegt die potentielle Anwendung für andere Materialien. Um dynamische Prozesse, insbesondere auf ultra-schnellen Zeitskalen zu erforschen, wird ein FEL benötigt. Daher werden zwei Experimente vorgestellt, welche am FLASH in Hamburg gemessen wurden. Eines zeigt mit einem künstlichen Kristall, dass SAB-CDI auch an einem FEL möglich ist. Das andere untersucht in einem *pump-probe* Experiment die ultra-schnellen, dynamischen Prozessen in Kolloidkristallen.

Die technischen Neuerungen in der Erzeugung von Synchrotronstrahlen ermöglichen die Anwendung der kohärenten Röntgenstrahlen. Die Kombination von iterativen Algorithmen zur Phasenbestimmung und Messverfahren aus der Kristallographie erzeugt die einzigartige Möglichkeit die innere Struktur von nano-strukturierten Materialien zu vermessen. In der vorliegenden Arbeit wird ein Einblick in dieses faszinierende Forschungsfeld gewährt.

Contents

Introduction

Direct methods in crystallography [KH50, Gia02] have revolutionized the field of structure determination in crystallography. Based on the simultaneous measurement of Bragg peaks, while rotating a crystal and powerful computational phasing methods, the structure of proteins to atomic resolution have been revealed. Crystallographic methods for structure determination are based on the assumptions about the crystallinity of the sample. Unfortunately, structural defects in the form of vacancies, dislocations, and stacking faults are additional complications and therefore it is vital to understand the structure of defects in detail. All conventional methods require a modelling through simulated data. No direct methods exist to image defects in crystals. Here a new method is proposed, which will enable to visualize the individual scatterers around and at defects in crystals. The method is based on coherent X-ray scattering.

To highlight the advantages of X-rays for imaging, two other existing imaging methods should to be mentioned for comparison, optical microscopy and electron microscopy. The field of optical microscopy has for centuries been a driving force in biology. The newest addition to the broad variety of methods, which have developed over time, is confocal microscopy [Paw06]. Confocal optical microscopy is a point scanning microscopy technique, which images the locations of particular fluorescent dyes in a biological specimen, potentially in all three dimensions. A special dye is introduced into the sample, which on illumination by a laser starts to fluoresce with a given wavelength. Since different dyes only attach to specific features in the sample, the features of interest can be investigated with great detail, with a resolution better than 200 nm. Even though this method can be applied to living specimen, the dyes might change the relevant biological process. Additional constraints are the limited lifetime of the dye and the problem that only the dyed components are visible, while the remaining part of the system cannot be investigated. It should be noted that naturally this method is limited to samples transparent to visible light, whereas most crystalline samples are opaque.

The other method is electron microscopy, which has already solved many relevant questions in the nano world. Due to the very small De-Broglie wavelength of the electrons with high kinetic energy, electron microscopy methods are outstanding considering the lateral resolution reaching atomic resolution in many cases. However, due to the limited penetration depth of electrons in matter the sample preparation is the bottleneck for electron microscopy. Electrons can either be used to scan the surface of a sample, which is called scanning electron microscopy (SEM). This is a very convenient method to retrieve a direct image of a sample, but often requires to cover the sample with a conducting material, such as gold, which might destroy the important properties. Electrons with higher energy on the other hand can be used to penetrate and even be transmitted through a thin specimen. In this so-called transmission electron microscopy (TEM) the

electrons are detected behind the sample. In general, with TEM some methods relevant for X-rays can also be applied, like absorption contrast or even coherent scattering. But here the sample preparation is more challenging, since only ≈100 nm or thinner slices can be investigated with electrons. This limits the method to thin specimen. Thick samples have to be sliced into thin parts, which are then imaged independently. This clearly does not allow any in situ measurements and might even add additional unwanted artefacts.

This short excursion clearly points out the advantages of X-rays. Since they can penetrate thick samples, buried structures can be investigated and biological specimen can, for example, be measured in their natural habitat, which is normally water. In addition, the direct damage of X-ray photons in matter are less severe than the damage of electrons. Recent developments increased the coherent flux of conventional sources such as synchrotrons by orders of magnitude. As a result, the use of the coherent properties of X-rays is emerging as a critical, important aspect of X-ray science. New upcoming and operating X-ray laser sources will accelerate this trend. One method which has the capacity to recover structural information from the coherently scattered photons is Coherent X-ray Diffraction Imaging (CXDI).

The main focus of this thesis will be the investigation of the structure and the dynamics of colloidal crystals, which are a great model for atomic crystals in order to understand the growth and defect structure of crystals. Despite the large interest in these structures, many details are still unknown about the processes governing self-assembly, driving the crystal into its FCC structure. Most of what is known about the crystal structure is obtained either through surface methods such as scanning electron microscopy (SEM) or through bulk averaging methods, such as microradian X-ray diffraction or optical microscopy methods. However, these techniques only provide information about stacking sequences over large areas of a crystal or about the crystal surface structure, but neglect the local defect structure. The inner structure is of utmost importance for the optical properties and for the growth process. Therefore, it is vital to develop new approaches to measure these properties in colloidal crystals. After an introduction in chapter one into the basics of the field of coherent X-ray scattering, this thesis will introduce a novel method, Small Angle Bragg Coherent Diffractive Imaging, (SAB-CDI) in chapter two, which besides the relevance to colloidal crystals can be applied to a large variety of nano structured materials. The third chapter will focus on experiments carried out at synchrotron sources showing the potential to apply SAB-CDI to colloidal crystals and also to nano wires. To investigate dynamics, especially on the ultrafast time scale, FEL sources are needed. The fourth chapter will therefore present two experiments performed at the FLASH facility in Hamburg, showing that SAB-CDI can also be applied at FELs on an artificial crystal and an experiment performed on colloidal crystals to investigate the ultra fast dynamics with a pump-probe experiment.

All in all the technical advances in synchrotron radiation creation have opened the field to applications with the coherent part of the X-rays. The combination of iterative phase retrieval methods with crystallographic methods yields the unique opportunity to measure the internal structure of nano structured samples. This thesis will give an introduction into this exciting new field.

1 Theoretical Background

1.1 X-ray Sources

After the discovery of X-rays in the late 19th century, a broad variety of applications of this initially unknown radiation have been invented. The most successful methods among them are applied to crystalline materials based on von Laue's discovery of diffraction of X-rays by crystals. Many of them are limited by the photon flux and thus the discovery of synchrotron radiation as a source for X-rays provided the necessary boost for new methods to leap forward. The main principle for the generation of X-rays uses the concept, that an accelerated charged particle emits radiation. In an X-ray tube the electrons are slowed down and emit Bremsstrahlung. However, the strongest source for X-rays in an X-ray tube are the emitted photons from the transition of electrons from the L shell to the K shell. The electrons in the K shell are removed by the high energy electrons in the X-ray tube. Since often copper is used as material in the anode the characteristic radiation from an X-ray tube is about 8 keV at the Cu K_α emission. As illustrated in Figure 1.1 the emission from an X-ray tube is not directed, the radiation is emitted into all directions.

If charged particles pass through an electro-magnetic field, their path is changed into an arc or even a circle due to the Lorenz forces. Since a motion on a circular trajectory can be considered as an accelerated motion towards the center, charged particles will emit radiation. This happens in an atom every time, when an incident electron changes its trajectory due to the positively charged core of the atom, the emitted radiation is called Bremsstrahlung. But the process of charged particles emitting radiation on a bent path is even more common in storage rings and cyclotrons, where normally electrons or positrons are kept on a circular path. Storage rings were built for particle physics and have been around for a long time, however, with the need of bigger collision energies, the large circular colloiders have increased in size, also pushing the field of accelerator physics to accelerate particles to higher energies.

In the beginning synchrotron radiation was used parasitically on the big ring accelerators from high energy particle physics. Electromagnetic radiation from the infrared to the hard X-ray was extracted from the kinetic energy of the relativistic electron beam in the storage rings. However, soon the unique properties: the very high intensity, the tunability over a large range of the electromagnetic spectrum, the polarization properties, a pulsed time structure, and extreme collimation became overwhelming. These properties played a key role for the development of new experimental techniques. Soon the user demand increased and dedicated synchrotron facilities were build. The newly developed methods reached a considerable state of maturity and a high degree of automation, so that these techniques became available for a broad user community.

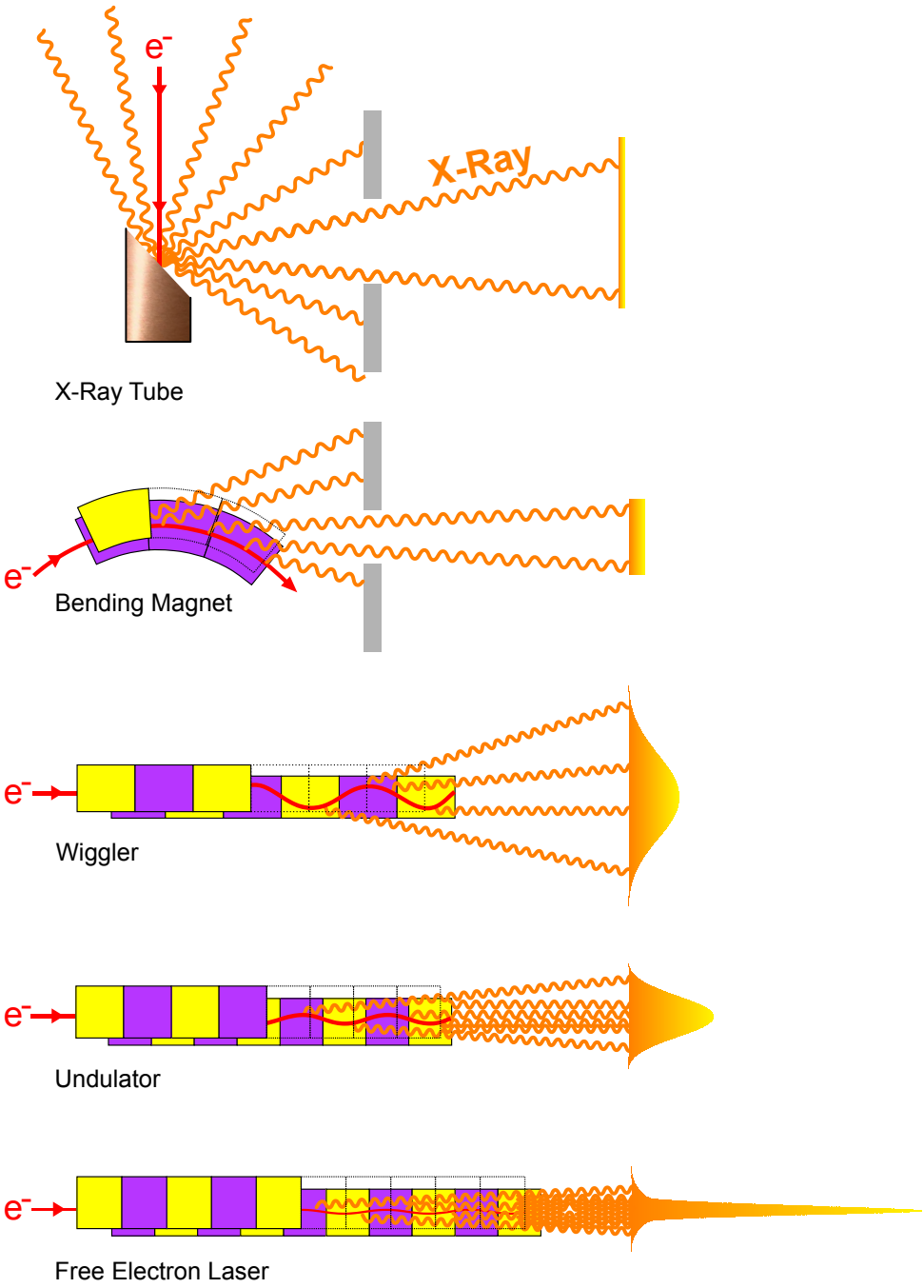

Figure 1.1: Different methods for the generation of X-rays, showing the difference between an X-ray tube, a bending magnet, a wiggler, an undulator and a Free Electron Laser. The electron beam is always marked in red and the X-rays are visualized here in orange. The different colors in the magnetic structures indicate the two different magnetic poles. The solid grey blocks represent slits.

1.1.1 Second and Third generation X-ray sources

A synchrotron radiation source is a storage ring in which the charged particles are kept on a steady trajectory. Dipole magnets are used to keep the particle on course. At each bending magnet the particles are deflected from their straight flight path and therefore, the bending magnets can also be used as a source for synchrotron radiation. In addition, a storage ring requires quadrupole magnets to focus the beam of charged particles and acceleration cavities to compensate for the energy loss on the circular motion. A whole field of science emerged to study the effects of different magnetic structures on electron beams as well as new techniques for the acceleration of the charged particles. Another crucial technological development is the function of electron guns, which are important to create the short electron bunches from a small source.

Assuming all the technological difficulties are overcome, a storage ring is an excellent source for strong electromagnetic radiation, reaching deep into the X-ray regime. Since a circular motion of the charged particles in a dipole field is an accelerated motion, the charged particles emit radiation, see Figure 1.1. Modern hard X-ray third generation synchrotron sources such as the European Synchrotron Radiation Facility (ESRF) in France, the Advanced Photon Source (APS) in the United States, and the Super Photon Ring-8 (SPring-8) in Japan operate with an energy at or above 6 GeV. The most recent addition to these is, since 2009, the Positron Elektron Tandem Ring Anlage (PETRA) III facility in Hamburg, Germany, also operating at 6 GeV.

The big milestone towards the third generation synchrotrons is the use of undulators as insertion devices. Their theoretical description reaches back until the late 1940s to early 1950s, by Ginzburg [Kul07] and Motz [Mot51]. An undulator is a periodic structure of dipole magnets. The magnetic field is alternating along the length of the undulator, which forces an oscillation onto the orbit of the electrons. This principle was first used in wigglers (see Figure 1.1) where the emitted radiation is N times the radiation from each magnet, where N is the number of magnets in the wiggler.

If the angular excursion of the particles is much smaller than the natural radiation width, the electromagnetic wave emitted in one turn interferes constructively with the field emitted in another turn and the magnetic structure is called an undulator. The interference occurs because a co-propagating radiation wavefront will always move ahead of the electrons. This interference results in a much smaller angular divergence, a smaller bandwidth, and the intensity can be as high as N^2 times more than from a bending magnet. The fundamental of resonance wavelength λ_1 in the emitted undulator spectrum is determined by

$$\lambda_1 = \frac{\lambda_u}{2\gamma_L^2}\left(1 + \frac{K^2}{2} + \gamma_L^2\theta^2\right), \tag{1.1}$$

here λ_u is the period of the magnets in the undulator and γ_L is the Lorentz factor, which is defined as $\gamma_L = 1/\sqrt{1+(v/c)^2}$, v is the velocity of the electrons, and c is the speed of light in vacuum. Furthermore λ_1 depends on K the undulator parameter, which is defined as $K = eB_0\lambda_u/2\pi m_e c$, where e is the elementary charge, B_0 is the magnetic field in the undulator, and m_e is the rest mass of the electron. For an undulator at a third generation synchrotron γ_L is in the order of 10^4 and λ_u is typically a few cm, this

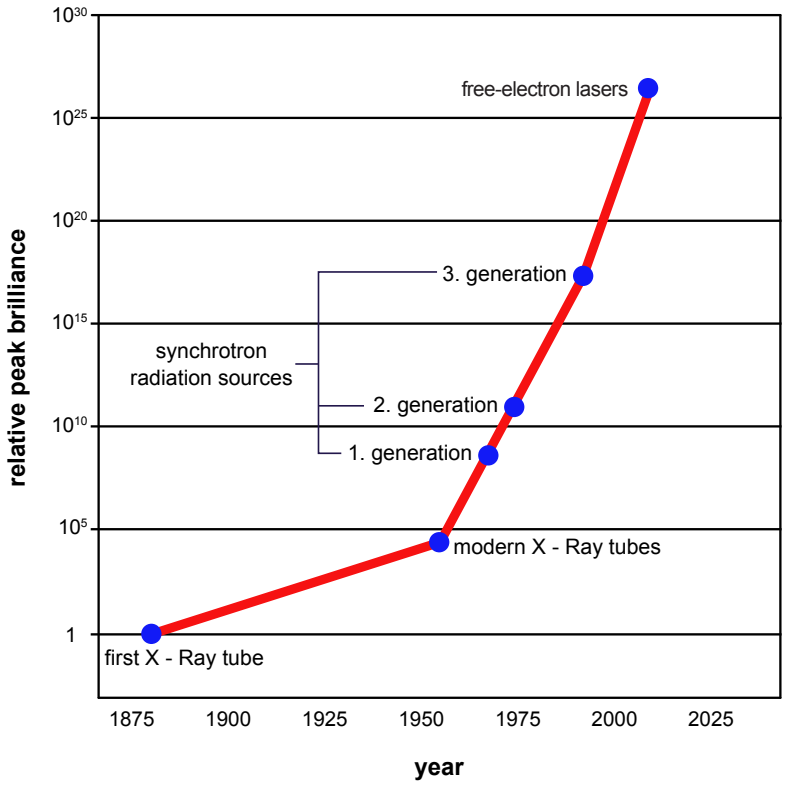

Figure 1.2: The development of peak brilliance of different X-ray sources as a function of the time [XFE]. The brilliance of a source is defined as the number of photons per second, divergence, source area, and 0.1% bandwidth. The brilliance of first, second, and third generation synchrotron sources are indicated as well as fourth generation sources (FELs). The peak brilliance values are normalized to the brilliance achieved from the first X-ray tubes.

results in λ_1 being in the order of Ångström. The shortest wavelength is observed on axis, whereas the wavelength off axis depends on the angle θ, due to the Doppler shift.

In the spectrum of the emitted radiation from an undulator higher harmonics λ_n can be observed [ANM01]. These appear due to the oscillations in the velocity of the electrons along the propagation direction ν_z. Since the total velocity of the electrons $\nu_e = \sqrt{\nu_x^2 + \nu_z^2}$ is preserved, a change in ν_x results in a change of ν_z. The electrons are forced into an oscillating path by the magnetic structure of the undulator and therefore ν_z also oscillates. These higher harmonics are an efficient source for high energy X-rays up to 100 keV and above.

The applications of these high brilliance X-ray sources stretch over almost all fields of science in particular atomic and cluster physics, condensed matter physics, chemistry, materials science, structural biology, crystallography, geo- and environmental science, and medical science. Many different methods have been developed over the years. Following the Technical Design Report (TDR) of the PETRA III facility [BBD$^+$04] some should be mentioned here, to point out the importance of third generation synchrotron sources, which deliver small parallel and intense X-ray beams.

Probably the most prominent application is protein crystallography [DG00]. For most of the relevant protein structures it is extremely difficult to grow bigger crystals. Furthermore, the complex structures lead to big unit cells and a very complicated, densely populated structure in reciprocal space, which requires a parallel and intense beam to solve the protein structure. Another method is high resolution diffraction from small sample areas [KD99]. For this application especially surfaces and interfaces of semiconductors are of interest and a small, parallel beam is needed here as well to measure the properties of the material in a very small, confined spot. Spectroscopy can be used to retrieve element specific information. The higher harmonics mentioned before are an excellent source for very small but intense photon beams of hard X-rays which are needed to penetrate large samples. Another technique, which is considered standard nowadays, is inelastic scattering [Sch07], which, together with nuclear resonant scattering [Sha95], is mostly limited by the available flux. This can be overcome by the available flux at third generation synchrotron sources. The mentioned methods gain a lot by the intense beams, but especially the increased coherent flux inspired new measurement methods, as for example X-ray photon correlation spectroscopy [BP08], which allows insight into dynamics of materials on time and length scales that are not accessible with other methods. But also methods formerly only known from visible light optics like phase contrast imaging[PWBD06], or holography[CN10] are now possible. Coherent X-rays open the route for lensless imaging on which this thesis focusses. This list is by no means complete but gives a short overview of the rich field of applications for third generation synchrotron radiation.

Even though third generation sources represent the frontier of modern science, fourth generation sources providing peak intensities $10^8 - 10^{10}$ times higher (see Figure 1.2) than other sources are already beginning to emerge. These X-ray free-electron lasers are opening up a new frontier across many areas of science.

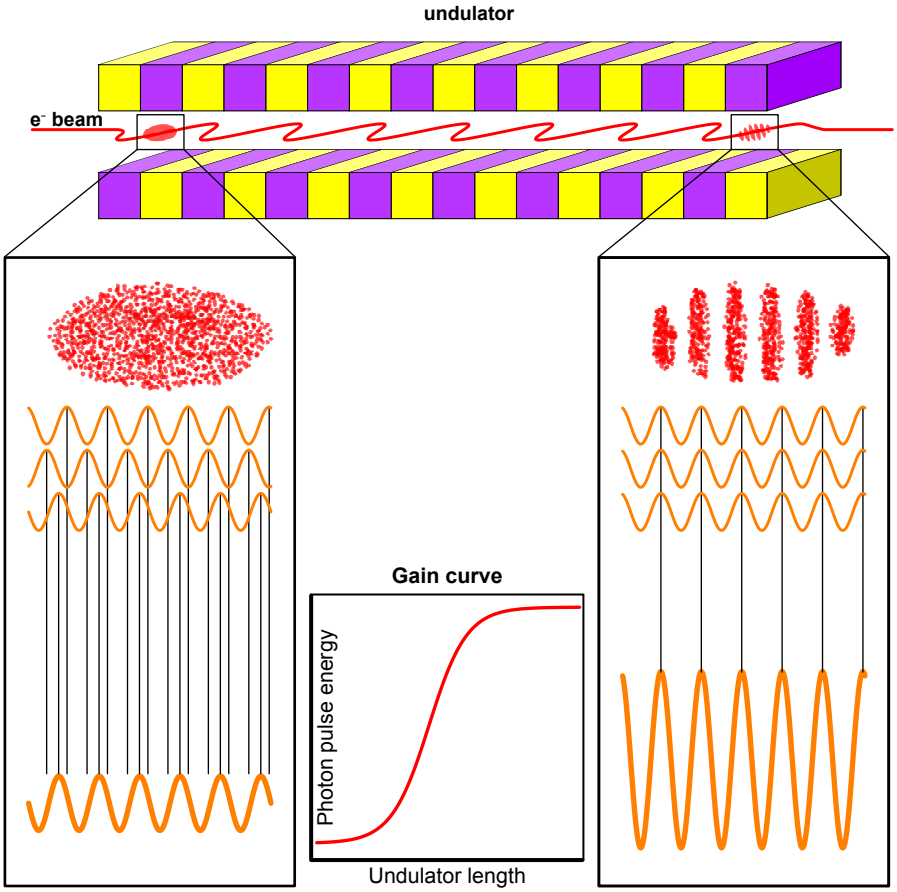

Figure 1.3: Illustrating the process of microbunching occuring when an electron pulse passes through an undulator in an FEL. The electron bunch travels from the left to the right and becomes structured. At the end of the undulator all micro bunches emitt coherently. The Figure is adapted from [MT10]

.

1.1.2 Fourth generation X-ray sources

It was proposed theoretically by Madey [Mad71] in 1971 to build a free-electron laser (FEL) that would generate X-ray radiation. The principle is based on the idea that in a long undulator the emitted electromagnetic field can become strong enough to influence the properties of the electron bunch [KS80, BPN84]. Then an exponential growth of the energy emitted by the particles is possible. This process is called Self Amplification of Spontaneous Emission (SASE). The short and simple description here serves to provide an overview to help the understanding of the phenomena relevant to this thesis. A detailed description of the SASE principle is given elsewhere [SSY00, MT10] and references therein.

The spontaneous radiation originating in an undulator is the basis for the SASE

process. Over the length of the undulator the electromagnetic field produced by the oscillating electrons gets strong enough to modulate the electron distribution within the electron bunch. The intense light imprints its wavelength onto the formerly smooth electron bunch, which becomes structured into several micro bunches (see Figure 1.3. Each of the micro bunches is narrower than the wavelength whereas the distance between the micro bunches is exactly the wavelength of the generated field. Through this interaction almost all electrons begin to emit coherent radiation in phase. Through constructive interference the intensity increases exponentially as the electron beam and the radiation co-propagate along the FEL undulator. This is illustrated in Figure 1.3, where the electron bunch is modulated into many micro bunches. It is also important to note that this process is taking place gradually throughout the undulator. This is shown in the gain curve in Figure 1.3. The SASE process starts in the low gain region at the start of the undulator. Then a region of linear gain is followed by the deep saturation regime, where all micro bunches emit coherently. A certain undulator length is necessary to reach saturation, therefore the undulator sections in the FELs are much longer than at synchrotron beamlines. The initial source of radiation originating from shot noise can be amplified by many orders of magnitude before the process saturates. The SASE process, in contrast to conventional lasers, does not rely on mirrors to create an oscillator cavity, which is hard to accomplish for X-rays. The FEL functions as a simple one pass amplifier, relying on a positive feedback process. The electrons emit radiation, which affects their position and thus causes them to emit with higher intensity (see Figure 1.3). The generated pulses reach peak powers of the order of 10^{12} Watts with a duration of ten to a few hundred fs.

As described in the TDR for the European XFEL [Ae06] this timescale is of particular importance because atoms in molecules oscillate around their equilibrium positions with typical periods of a few hundreds of femtoseconds. Furthermore, movements of atoms during the rearrangement of their positions in chemical reactions, or phase transformations also occur on such a timescales. The outstanding properties of FEL beams, namely the high degree of coherence, the ultra-high brilliance, the time structure as well as the development of appropriate detectors and instrumentation will allow for entirely new new experiments to be conducted.

According to the TDR these high intensities can also be used to produce highly ionised states of atoms, generating conditions and processes occurring in interstellar gases in a controlled environment. In conjunction with the ultra-short pulse duration this can be exploited in pump-and-probe experiments, where conventional laser pulses (pump) are used to trigger a reaction or a phase transition and the FEL pulses (probe) follow the pump pulse with a well determined delay from $\approx$50 fs up to nanoseconds and beyond. This can provide a movie of the atomic displacements and rearrangement of chemical bonds. In this way, catalytic mechanisms in chemical and biochemical reactions can be elucidated, fast reactions (e.g. combustion) can be subject to detailed investigation, nucleation of ordered phases at phase transitions can be imaged, and hitherto inaccessible states of matter can be brought to experimental investigation. If the pump pulse is sufficiently powerful to produce a plasma, the X-ray pulse can still penetrate the highly ionised medium which is opaque to visible light and provide information on the

propagation of the shock front.

The high degree of coherence in the FEL beam can be used for holographic and lensless imaging in material science[VR03] and biology [MYV10]. Spectacular possibilities open up as detailed theoretical studies and simulations predict that, with a single very short and intense coherent X-ray pulse from the FEL, a diffraction pattern may be recorded from a large macromolecule, a virus, or a cell, without the need for crystalline periodicity. This would eliminate a impedimental bottleneck for many systems of high interest, e.g. membrane proteins, viruses and viral genomes. Measurement of the over-sampled X-ray diffraction pattern permits phase retrieval and hence, structure determination. Although individual samples would eventually be destroyed by the very intense X-ray pulse, a three-dimensional data set could be assembled if copies of a reproducible sample were exposed to the beam one by one.

In addition to these decisive technical advantages, it will be possible to reduce the time necessary to complete experiments, which are now done at synchrotron sources, by two orders of magnitude. It should be noted here that the first results from the upcoming sources have recently been published. Among them a particularly interesting experiment, performed at the LCLS, should be mentioned here, where nanocrystals were measured and the diffraction pattern was inverted to retrieve the structure of a membrane protein complex [CFB$^+$11].

1.2 Coherence

One important property of laser light is the high degree of coherence, which can be exploited in several measurement methods. Coherence, in general, describes the properties of the correlation between the physical quantities of a wave. Interference is one of the most fundamental phenomena in physics and it can only occur due to coherence effects. The coherence properties of light can be distinguished into two kinds, the transverse coherence length, which is also called the spatial coherence, and the longitudinal coherence length or coherence time. First the spatial coherence should be discussed.

1.2.1 Spatial Coherence

The spatial coherence describes the ability for two points in space r_1 and r_2, of a wave field to interfere. Therefore, the spatial coherence is the correlation between two arbitrary points in a wave. A wave with only one amplitude value over an infinite length is spatially perfectly coherent. This is normally assumed when talking about plane waves.

Light can be expressed as a time- and space-varying electromagnetic field $E(\mathbf{r}, t)$, which is a complex function with amplitude and phase, where $\mathbf{r}$ denotes the position in three dimensional space and t is the time. According to its definition [Goo00, MW95] the first order correlation function for this field can be written as the so-called mutual coherence function

$$\Gamma(\mathbf{r}_1, \mathbf{r}_2, \tau) = \langle E(\mathbf{r}_1, t) E^*(\mathbf{r}_2, t + \tau) \rangle \,, \tag{1.2}$$

where τ is the time delay. Equation (1.2) is treated as an ensemble average over all

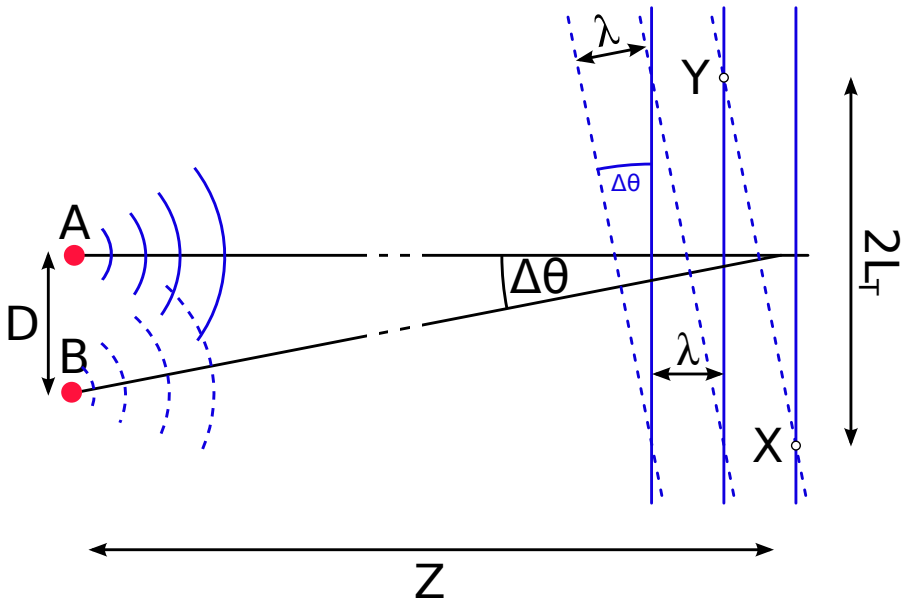

Figure 1.4: Showing the spatial coherence at a distance Z from an extended source with a size D. Two waves with the same wavelength interfere and the distance along the wavefront A until the waves are out of phase is called transverse coherence length L_T.

possible realizations of the field. Higher order correlation functions can be neglected since most X-ray sources obey Gaussian statistics [Sin12], and so the first order mutual coherence function completely defines the field. The degree of coherence of the wavefield is expressed by the normalized mutual coherence function that is called complex degree of coherence

$$\gamma_c(\mathbf{r}_1, \mathbf{r}_2, \tau) = \frac{\Gamma(\mathbf{r}_1, \mathbf{r}_2, \tau)}{\sqrt{\Gamma(\mathbf{r}_1, \mathbf{r}_1, 0)\Gamma(\mathbf{r}_2, \mathbf{r}_2, 0)}}. \tag{1.3}$$

It can also be written in an equivalent form

$$\gamma_c(\mathbf{r}_1, \mathbf{r}_2, \tau) = \frac{\langle E(\mathbf{r}_1, t)E^*(\mathbf{r}_2, t+\tau)\rangle}{\sqrt{\langle I(\mathbf{r}_1, t)\rangle \langle I(\mathbf{r}_2, t)\rangle}}. \tag{1.4}$$

If the time delay $\tau = 0$ this function is called the complex coherence factor.

A full experimental exploration of this coherence function would require two pinholes each exploring a two-dimensional surface, leading to an extremely demanding experiment resulting in a four-dimensional data set. An easy measurement of the spatial coherence is Young's double slit experiment [You07, Goo00, Sin12] (see section 1.2.3). It measures the degree of coherence between two points $(\mathbf{r}_1, \mathbf{r}_2)$ separated in space by analysing the contrast in the resulting interference pattern. In practice, the concept of a coherence length is used to express the degree of coherence of an X-ray source. The transverse coherence length for an incoherent source can be calculated from the following expression

[ANM01]

$$L_T = \frac{\lambda}{2\pi}\left(\frac{Z}{D}\right), \tag{1.5}$$

where λ is the wavelength, Z is the distance from the source and D is the spatial extent of the source. Figure 1.4 illustrates the transverse coherence length through the interference of two waves emitted from an extended source. The waves radiate from the edges (A and B) of the source. At a large distance Z compared to the size D of the source the two waves interfere. Here the distance along the wavefront A until the waves are in phase again is defined as twice the transverse coherence length L_T. The degree of coherence is defined as the ratio of the transversal coherence length to the beam size. Using equation (1.5) the spatial coherence and the degree of coherence of two different X-ray sources will be compared.

Some of the measurements discussed later in this thesis were performed at the P10 beamline at the PETRA III facility. At this end station the sample is located at a distance about $Z = 90$ m from the 5 m long undulator, which is the source of the X-rays. The typical size of the electron beam in this low β part of the PETRA III accelerator is $D = 6$ μm in vertical and 36 μm in horizontal direction, which defines the source size. For experiments carried out at 8 keV ($\lambda = 0.15$ nm) according to equation (1.5) this results in a coherence length of 358 μm in the vertical and 60 μm in the horizontal direction. Compared to the beam size, which at the sample position is about 390 μm vertically and 2520 μm horizontally [BBD$^+$04], this results in a degree of coherence of 0.91 vertically and 0.02 horizontally. It has to be noted that this is the coherence due to the source properties. For an experiment which needs a higher degree of coherence beam defining slits can be used close to the source to increase the degree of coherence at the sample. This, however, also decreases the photon flux at the sample.

As a comparison, the numbers for a measurement at FLASH as an example for free-electron laser radiation are given here. The sample is typically positioned 70 m downstream from the source. The most commonly used wavelength at FLASH is 13.5 nm. Assuming a source size of 68 μm as it is stated in [AAA$^+$07], according to equation (1.5) this results in a transverse coherence length of 2200 μm. The beam at a FEL is considered to be round. The divergence of 90 μrad leads to a beam size of 6.3 mm after 70 m, therefore the degree of coherence at the sample position is 0.34 in both directions. Compared to the values for PETRA the main advantage is a much higher degree of coherence in the horizontal direction, since the application of coherent scattering methods depends on the coherence in both directions. These examples show that at modern X-ray sources a very high degree of coherence can be reached with a very high photon flux. This makes coherent imaging techniques feasible.

1.2.2 Temporal Coherence

The longitudinal coherence length has to be introduced, since a real X-ray source is never perfectly monochromatic. This has an impact on the coherence time [ANM01]. In Figure 1.5 two waves (Red and Blue) are illustrated with slightly different wavelengths, λ and $\lambda + \Delta\lambda$. Both waves propagate from the same source parallel to each other. At a

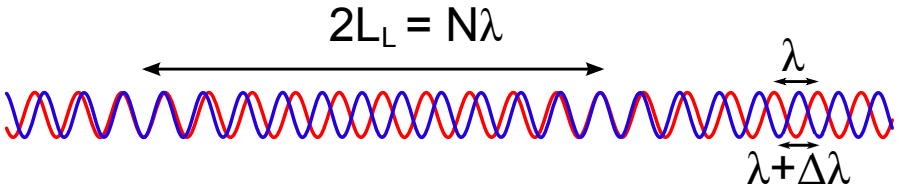

Figure 1.5: Showing the temporal coherence. Two waves with different wavelength are emitted in the same direction. The distance between 2 perfect phase matches is defined as $2L_L$.

specific point the two waves are exactly in phase. After a certain distance the waves are in phase again. This distance is defined as $2L_L$, twice the longitudinal coherence length. The distance $2L_L$ can be expressed as a multiple N of λ for the red wave in Figure 1.5, and for the blue wave it is equivalent $(N-1)$ multiples of $\lambda+\Delta\lambda$. Combining these two conditions yields

$$2L_L = N\lambda = (N-1)(\lambda+\Delta\lambda). \tag{1.6}$$

This equation implies that $(N-1)\Delta\lambda = \lambda$ and this yields $N \approx \lambda/\Delta\lambda$. This is used to express the longitudinal coherence length as a function of the wavelength and the bandwidth

$$L_L = \frac{1}{2}\frac{\lambda^2}{\Delta\lambda}. \tag{1.7}$$

This means that the temporal coherence is mainly defined by how monochromatic a source is. All the synchrotron experiments discussed in this thesis, were performed using monochromator crystals that achieve a monochromaticity better than $\Delta\lambda/\lambda \approx 10^{-4}$. Therefore effects which would occur due to partial temporal coherence do not have to be considered.

1.2.3 Youngs double slit experiment

To underline the importance of coherence the effects of partial transverse coherence have to be investigated. This can be understood best in the double slit scattering experiment originally performed by T. Young [You07]. The historical purpose of the experiment was to prove the wave theory of light and was compared in the original publication to the behavior of water waves. Today the complicated nature of light is largely understood [Gla63b, Gla63a]. With the discovery of the quantized nature of light, the need for statistical methods in optics increased dramatically [Goo00]. The coherence properties of light depend on many factors. It was stated in equation (1.5) that the transverse coherence depends on the source size for a distant incoherent source.

In Figure 1.6 the blue source is fully coherent whereas the light from the red source, due to its larger spatial extent, has a smaller degree of coherence. An X-ray source can be considered as a number of independent point sources statistically distributed over a source size D. Each of the point sources radiates a spherical wave. All independent waves superimpose on each other, still, at a distance Z a certain correlation is present.

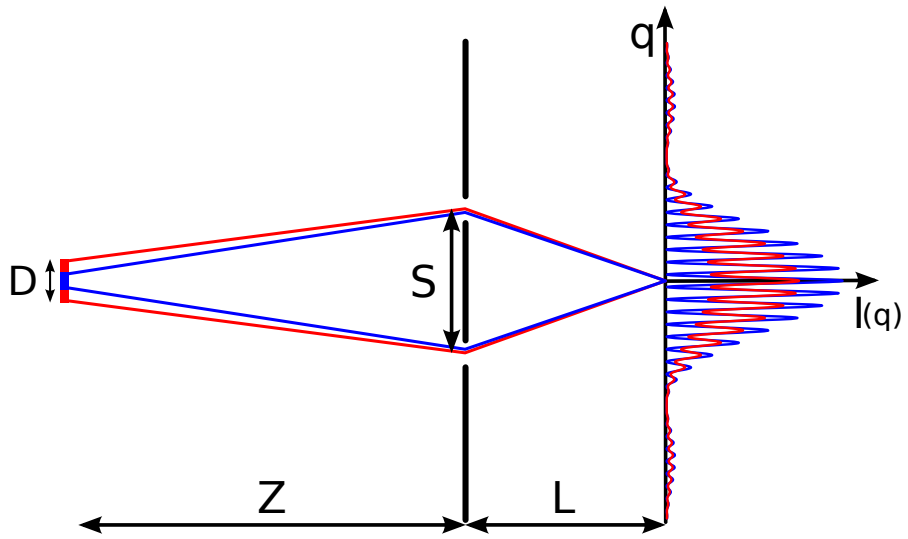

Figure 1.6: A schematic of the simple double slit scattering experiment. Two independent wavefronts from 2 sources (red and blue) each interfere behind a double slit. The resulting diffracted intensity strongly depends on the coherence of the light.

The light passes through either of the two openings, separated by a distance S. Due to the wave-like nature of light the two transmitted fields overlap in the detector plane after a distance L. The distinct interference pattern from a double slit can be expressed as [Goo00]

$$I(\mathbf{q}) = \mathrm{sinc}^2(\mathbf{q}) \cdot (1 + \gamma_c \cos(S\mathbf{q})), \tag{1.8}$$

where the sinc function is defined as $\mathrm{sinc}(x) = sin(x)/x$, $\mathbf{q}$ is the momentum transfer vector, γ_c is the complex coherence factor introduced in equation (1.4), and S is the separation between the slits. The intensities in Figure 1.6 plotted in blue represent the case for a fully coherent source, when $\gamma_c = 1$. Due to the destructive interference the intensity reaches zero and the contrast between the fringes is at a maximum. Assuming a bigger source (shown in red in Figure 1.6), that produces less coherent light resulting in a $\gamma_c < 1$, the contrast is considerably less.

For the experiments and methods described and used later in this thesis the contrast and in particular the zeros of the scattered intensities are of utmost importance, since these define the properties of the scattered intensities. The scattering pattern is a result of the interference of the two transmitted waves and as such, interference can, depending on the coherence, provide a superb measure of the phases of X-rays, which may carry detailed information about a source or a scattering object.

1.3 Kinematical Scattering

The previous section discussed various methods to create X-rays. Here the interaction of X-rays with matter will be described. Of major interest is the elastic scattering process on the electrons in the material. Due to the nature of the experiments in this thesis, which mainly focusses on small angle scattering, the polarization of light can be neglected.

The elementary scattering process is a single photon interaction with an electron. The electric field of the incident X-ray photon forces the charged particles to accelerate and radiate the scattered wave. In Figure 1.7 this process is illustrated. Due to energy and momentum conservation the electron cannot be seen as a free electron but rather has to be considered as a loosely bound electron. The scattering process is called *elastic* when the incident wavelength is identical to the wavelength of the scattered photon. The Compton effect should be mentioned here, which, following the quantum mechanical description, allows for a momentum and energy transfer with the result that the scattered photon has a lower frequency relative to that of the incident one. Following the idea that the wavelength is conserved the following classical description is enough to describe the discussed effects.

If the initial and scattered momenta of the X-ray photon are denoted as $\mathbf{k}$ and $\mathbf{k}'$ the scattering vector $\mathbf{q}$ can be defined as

$$\mathbf{q} = \mathbf{k} - \mathbf{k}' \tag{1.9}$$

Since only elastic scattering is considered $|\mathbf{k}|$ is equal to $|\mathbf{k}'|$. The magnitude of the scattering vector depends on the angle θ between the wave vectors, see Figure 1.7

$$|\mathbf{q}| = \left(\frac{4\pi}{\lambda}\right) \sin\theta, \tag{1.10}$$

where λ is the wavelength of the incoming and the scattered wave.

After introducing the fundamental concept of scattering, the term *kinematical* should be explained. The kinematical approximation is also known as the weak-scattering limit, since the cross section between the high energy photons and the material is very small. This implies that each photon scatters only once in the material, which leads to a considerable simplification in the description of the scattering process. Due to the high energy of the photons used in the experiments discussed later in this thesis, the kinematical approximation can be used.

This section is dedicated to the description of kinematical scattering and will firstly explain the scattering from atoms and crystals. Secondly, the influence of illumination with coherent X-rays on finite sized crystals is discussed. The last part will focus on the effects of defects and strain on the scattered intensities.

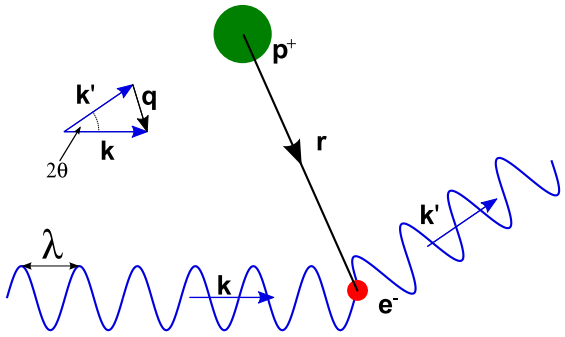

Figure 1.7: The scattering of a monochromatic X-ray wave, on the simple system of a weakly bound electron. The incident wave is labeled with the wavevector $\mathbf{k}$. The scattered wave propagates into the direction of the scattering wavevector $\mathbf{k}'$ and has the same wavelength λ. The difference between the two wave vectors is defined by the scattering vector $\mathbf{q}$.

1.3.1 Diffraction from Atoms and Crystals

Before discussing crystalline materials the scattering process from individual atoms should be introduced. The elastic scattering amplitude of X-rays on an assembly of electrons, for example the electron structure in an atom, can be written as [ANM01]

$$A(\mathbf{q}) = -r_0 \sum_{\mathbf{r}_j} e^{i\mathbf{q}\cdot\mathbf{r}_j}, \tag{1.11}$$

where r_0 is the Thomson scattering length and $\mathbf{r}_j$ are the positions of the electrons. The summation is carried out over the positions of all electrons.

The distribution of electrons in an atom can be expressed as a charge distribution, or electron density $\rho(\mathbf{r})$. The total number of electrons in the atom is given by the integral over the electron density. The scattering amplitude of an atom can be written as

$$A(\mathbf{q}) = -r_0 f(\mathbf{q}) = -r_0 \int \rho(\mathbf{r}) e^{i\mathbf{q}\cdot\mathbf{r}} d\mathbf{r}, \tag{1.12}$$

where $f(\mathbf{q})$ is known as the atomic form factor and the integration is performed over the entire volume. Equation (1.12) shows that the electron density is encoded in the scattered amplitude via a Fourier transformation (FT).

It has to be noted here that the relation in equation (1.12) is only valid for the far field scattering condition which is fulfilled when the Fresnel number [ST07]

$$N_f = \frac{d^2}{\lambda Z} \gg 1, \tag{1.13}$$

where d is the size of the scattering object, λ is the wavelength and Z is the distance at which the scattered amplitude is observed. Obviously, this condition is easily fulfilled

for small objects as individual atoms.

The previously assumed continuous energy distribution of electrons in the atom has been proven wrong by quantum mechanics. Instead the electrons stay in distinct quantum states with specific energies. If the absorption process is taken into account, the atomic form factor becomes energy dependent and two correction terms have to be introduced,

$$f(\mathbf{q}, \hbar\omega) = f^0(\mathbf{q}) + f'(\hbar\omega) + if''(\hbar\omega), \tag{1.14}$$

where f' is the real, and f'' is the imaginary part of the dispersion correction. A detailed derivation and a more thorough analysis of the interrelations can be found in [ANM01].

In a crystalline material all the atoms are placed on a regular grid. The three dimensional lattice can be defined by a set of vectors $\mathbf{R}_n$

$$\mathbf{R}_n = n_1\mathbf{a}_1 + n_2\mathbf{a}_2 + n_3\mathbf{a}_3, \tag{1.15}$$

where $\mathbf{a}_1$,$\mathbf{a}_2$, and $\mathbf{a}_3$ are the unit cell lattice vectors, and n_1, n_2, and n_3 are the corresponding integer factors. This is illustrated in Figures 1.8 and 1.9 for a two dimensional case. A unit cell is *indicated* for the lattice and via translations along the lattice vectors the entire crystal can be build up. Crystals are not restricted to atoms, as the basic structural unit, but rather complex structures can also be used to create crystals. A simple and well known example is NaCl where the basic structural unit is build up of a Na^+ ion bound to a Cl^- ion.

As it follows from equation (1.12), the scattering amplitude from a crystal can be written as

$$A(\mathbf{q}) = -r_0 \sum_n e^{i\mathbf{q}\cdot\mathbf{R}_n} \sum_j f_j(\mathbf{q}) e^{i\mathbf{q}\cdot\mathbf{r}_j}. \tag{1.16}$$

Here it is assumed that the position of each atom is given by $\mathbf{r} = \mathbf{R}_n + \mathbf{r}_j$, where $\mathbf{R}_n$ is the position of the unit cell and $\mathbf{r}_j$ is the position of the atom within the unit cell. The two sums are called the lattice sum and the unit cell structure factor, respectively.

Since the atoms are located in a regular grid in the crystal they form distinct families of planes. A given plane family is defined through the interception with the three points $a_1/h, a_2/k$, and a_3/l. The integers h, k, l are called the Miller indices, which are used in crystallography to describe crystal planes. It is important to note that all planes within one family are equally spaced by the lattice spacing d_{hkl}. For a simple cubic lattice this is defined by

$$d_{hkl} = \frac{a}{\sqrt{h^2 + k^2 + l^2}}, \tag{1.17}$$

the numerator a is called the lattice parameter, which, in a simple cubic lattice, is just $a = |\mathbf{a}_1| = |\mathbf{a}_2| = |\mathbf{a}_3|$. Figure 1.8 shows two plane families for the 2D case. The $h = 1$ and the $k = 0$ planes are marked in black, and the plane family corresponding to $h = 1$ and $k = 1$ are indicated as grey dotted lines.

When an incoming wave of X-rays is scattered by the atoms in the crystal the scattered waves from one family of planes can constructively interfere. In this case the scattering in one specific direction becomes very strong. The condition for constructive interference

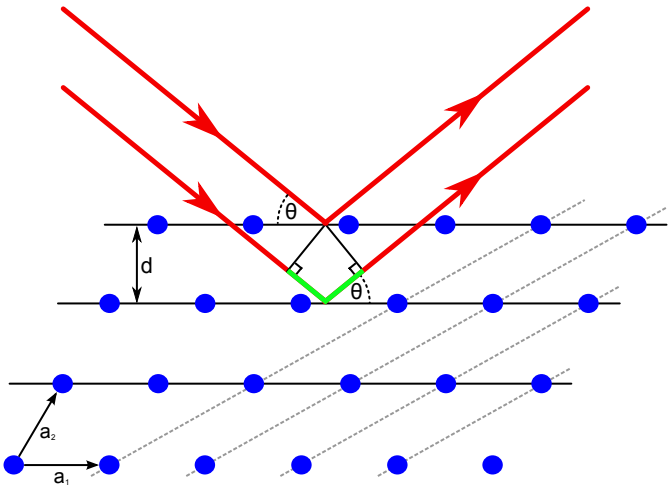

Figure 1.8: Braggs law illustrated for a 2D case. The (10) planes are indicated as black lines. The X-rays seem to reflect off these planes. If the path difference $2d\sin\theta$ (illustrated in green), is equal to an integer multiple of the wavelength λ the reflected waves will constructively interfere. The dotted grey lines indicate another plane family in the same crystal, the (11) planes.

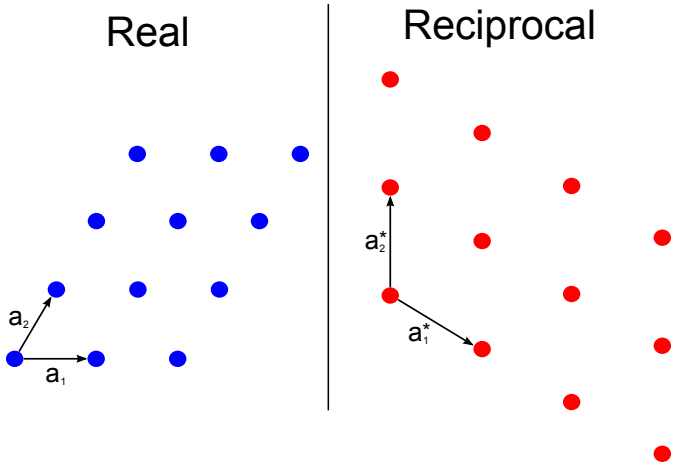

Figure 1.9: An example of the construction of a reciprocal lattice in two dimensions, which can easily be extended into the third dimension.

is illustrated in Figure 1.8 and is also known as Braggs law,

$$2d_{hkl}\sin\theta = n\lambda, \tag{1.18}$$

where d_{hkl} is the lattice spacing, θ is the angle between the incoming wave vector and the crystal planes, and λ is the wavelength of the X-rays. This describes that the condition for the constructive interference is fulfilled when the path difference between two waves ($2d\sin\theta$) is equal to a multiple of the wavelength. Since this condition can be fulfilled for many combinations of h, k, and l several Bragg reflections can appear. It should be noted here that Braggs law is universal and neither specific to X-rays nor crystals, but can be applied to multilayer systems as well as visible light and colloidal crystals.

On account of the regular translation periodicity in a crystal the Bragg reflections are on a regular grid as well, which is called the reciprocal lattice. The reciprocal lattice is formed by the three basis vectors

$$\mathbf{a}_1^* = 2\pi\frac{\mathbf{a}_2\times\mathbf{a}_3}{\mathbf{a}_1\cdot(\mathbf{a}_2\times\mathbf{a}_3)}, \quad \mathbf{a}_2^* = 2\pi\frac{\mathbf{a}_3\times\mathbf{a}_1}{\mathbf{a}_1\cdot(\mathbf{a}_2\times\mathbf{a}_3)}, \quad \mathbf{a}_3^* = 2\pi\frac{\mathbf{a}_1\times\mathbf{a}_2}{\mathbf{a}_1\cdot(\mathbf{a}_2\times\mathbf{a}_3)}. \tag{1.19}$$

This is also shown in Figure 1.9, where, for the 2D case, a crystal lattice and the corresponding reciprocal lattice are shown.

Similar to equation (1.15) any point in the reciprocal lattice can be expressed as

$$\mathbf{g} = h\mathbf{a}_1^* + k\mathbf{a}_2^* + l\mathbf{a}_3^*, \tag{1.20}$$

where h, k, and l are the Miller indices.

Another geometrical explanation to help the understanding of scattering, is the Ewald construction. It is shown for the 2D case in Figure 1.10. This construction elucidates in reciprocal space the relationship between the reciprocal lattice of the crystal $\mathbf{g}$, the diffraction angle for a given reflection θ, and the wavevectors of the incident and diffracted X-rays. The wave vector of the incident field is denoted as $\mathbf{k}$, whereas the diffracted wave is expressed by the wave vector $\mathbf{k}'$. In the case of elastic scattering both their length are equal to $2\pi/\lambda$. The scattering vector must lie on the circumference of a circle with the radius $|\mathbf{k}|$. For the three dimensional reciprocal lattice this circle is expanded into a sphere,which is commonly known as the Ewald sphere.

In an experiment the wavelength will always have a certain bandwidth. This bandwidth can be visualized in the Ewald construction through the thickness of the circle line, see Figure 1.10. This shows that for a very broad bandwidth more Bragg peaks will be measured. This, however, is mostly not desired, since in this case the interpretation of the diffraction pattern becomes very difficult. Also the width of the Bragg peaks can differ from the ideal delta function. For example, defects in the crystal lattice, as they will be explained in the next subsection, can broaden Bragg peaks.

Several different crystal structures exist, the most common ones for mono atomic crystals are simple cubic, body centered cubic (BCC), and face centered cubic (FCC). Apart from the cubic structures a wide range of other crystal structures occur in nature, among them triclinic, orthorhombic and hexagonal structures [Kit06]. However, most

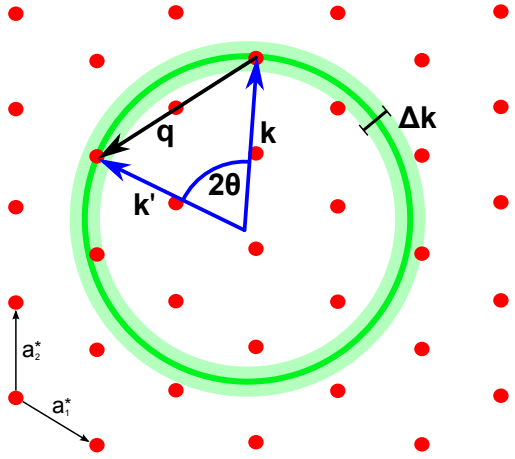

Figure 1.10: The Ewald circle in two dimensions. Monochromatic incident radiation specified by $\mathbf{k}$ can be scattered to any wavevector $\mathbf{k}'$ terminating on the dark green circle with the radius $|k|$. The bandwidth of the incident radiation Δk is indicated by the thickness of the light green circle, which touches more Bragg peaks (red dots) in the reciprocal lattice.

materials without directional bonds prefer to crystallize in a closed packed state, since it uses the least space and also minimizes the free energy in the system. To illustrate crystal structures atoms are often simplified as hard spheres. Closed packing of hard spheres is identical to the stacking of cannon balls. For such a system there are two different possible arrangements. Figure 1.11 shows the two possible solutions of stacking three layers of hard spheres. In both configurations the bottom most layer (**A**) is a dense arrangement where each atom has six neighbours. On top of the first layer the second plane (**B**) is positioned in the holes created by the first layer, forming a dense layer. The third layer now has two possible positions to be located, either directly on top of the first layer, in which case a hexagonal close-packed (HCP) structure is created. The third layer is again denoted with (**A**), since in this layer all atoms sit at the same positions except for the vertical displacement, as in the first layer, resulting in the sequence (**..ABABAB..**). The other possible stacking of the third layer occurs when all three planes are shifted relative to each other. The fourth layer is positioned directly over plane **A** and the sequence is repeated. The third layer can then be denoted as **C** and a sequence of (**..ABCABC..**) arises, which is then repeated. For ideal crystals either of the sequences is repeated throughout the entire crystal. However, it is easily possible that one of the layers slips and instead of a pure HCP or FCC stacking a random mixture of either occurs. This stacking is called random hexagonal close packed (RHCP). It still fulfills the closest stacking conditions, where the maximum packing fraction $\Phi = \pi/3\sqrt{2} \approx 74\%$ of the volume is filled. The packing fraction is defined as the ratio of the total volume of a set of objects packed into a space to the volume of that space [Dic05].

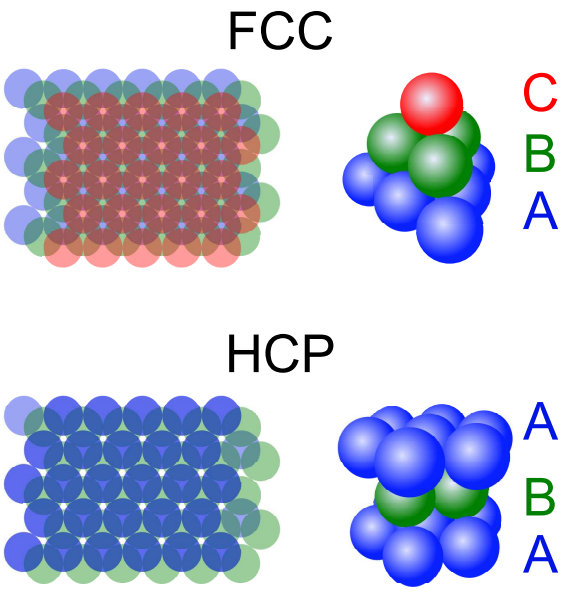

Figure 1.11: Illustrating the possible stacking of three layers of hard spheres, which can stack in FCC or in HCP.

1.3.2 Coherent Scattering on Finite Size Crystals

In the previous sections it was always assumed that the crystal has an infinite extent, or that the transverse coherence length is much smaller than the size of the crystalline sample. Now the case of a finite crystal illuminated by coherent X-ray radiation will be considered, where the coherence length exceeds the size of the crystalline sample. This is especially important since the coherence length at modern synchrotron sources can easily be larger than the size of a crystal, in which case completely different interference effects occur.

For a crystalline material the electron density can be written as a sum over all N unit cells

$$\rho(\mathbf{r}) = \sum_{n}^{N} \sum_{j} \rho_{nj}(\mathbf{r} - \mathbf{R}_{nj}), \tag{1.21}$$

as it was already applied in equation (1.16).

For the modification towards finite sized crystals the shape function $s(\mathbf{r})$ also called the Ewald function [Ewa40] has to be introduced. it describes the size and shape of the crystal. It is defined as unity inside the volume V_0 of the crystal and as zero outside

$$s(\mathbf{r}) = \begin{cases} 1 & \text{for} \quad \mathbf{r} \in V_0 \\ 0 & \text{for} \quad \mathbf{r} \notin V_0. \end{cases} \tag{1.22}$$

The infinite ideal lattice of the crystal is defined through

$$\rho_\infty(\mathbf{r}) = \sum_{n=1}^{\infty} \delta(\mathbf{r} - \mathbf{R}_n), \tag{1.23}$$

where $\mathbf{R}_n$ denotes the position of the unit cell, see equation (1.15). The electron density of one unit cell within the crystal is expressed as

$$\rho_{uc}(\mathbf{r}) = \sum_j \rho_j(\mathbf{r} - \mathbf{r}_j), \tag{1.24}$$

where $\rho_j(\mathbf{r})$ is the electron density of the individual atoms in the unit cell. Now the electron density for a finite size crystal can be deduced

$$\rho(\mathbf{r}) = [s(\mathbf{r}) \cdot \rho_\infty(\mathbf{r})] \otimes \rho_{uc}(\mathbf{r}), \tag{1.25}$$

where $\otimes$ stands for a convolution.

Using equation (1.12) and substituting the electron density of a finite crystal the scattering amplitude

$$A(\mathbf{q}) = F(\mathbf{q}) \cdot [P_\infty(\mathbf{q}) \otimes S(\mathbf{q})] \tag{1.26}$$

of a finite crystal can be deduced using the convolution theorem. The function

$$F(\mathbf{q}) = \int \rho_{uc}(\mathbf{r}) e^{-i\mathbf{q}\cdot\mathbf{r}} d\mathbf{r} = \sum_j f_i(\mathbf{q}) e^{-i\mathbf{q}\cdot\mathbf{r}_j} \tag{1.27}$$

is the structure factor of the unit cell containing the atomic scattering factor

$$f_j(\mathbf{q}) = \int \rho_j(\mathbf{r}) e^{-i\mathbf{q}\cdot\mathbf{r}} d\mathbf{r}, \tag{1.28}$$

of the j-th atom. The integration is carried out over the volume of the unit cell. It is assumed here that the structure factors of the different unit cells are all identical. In the same equation $P_\infty(\mathbf{q})$ is the Fourier transform of the lattice function, which reduces to the sum of δ-functions in reciprocal space

$$P_\infty(\mathbf{q}) = \int \rho_\infty(\mathbf{r}) e^{-i\mathbf{q}\cdot\mathbf{r}} d\mathbf{r} = \frac{(2\pi)^3}{V_u} \sum_n \delta(\mathbf{q} - \mathbf{g}_n), \tag{1.29}$$

where V_u is the volume of the unit cell and $\mathbf{g}_n$ is the reciprocal space lattice vector. The summation in equation (1.29) is carried out over all the reciprocal lattice points. The function $S(\mathbf{q})$ introduced in equation (1.26) is the Fourier transform of the shape function $s(\mathbf{r})$.

In summary, in the frame of the kinematical approximation the scattering amplitude $A(\mathbf{q})$, originating from the scattering of coherent X-rays on a finite-size crystal, is the FT of the periodic electron density of the crystal. It was, furthermore, shown in [VR01a]

that the shape function is encoded in the scattering signal around each Bragg peak. It can be represented in the following form [VR01a, VR03]

$$A(\mathbf{q}) = \frac{F(\mathbf{q})}{V} \sum_n S(\mathbf{q} - \mathbf{g}_n), \tag{1.30}$$

where $F(\mathbf{q})$ is the form factor of the electron density of a crystalline particle sampled at the Bragg position $\mathbf{g}_n$ defined by the 3D reciprocal lattice vectors $\mathbf{g}_n$, and $S(\mathbf{q})$ is the FT of the shape function $s(\mathbf{r})$ of the crystalline sample. The method of coherent diffractive imaging, which will be introduced in the following section, can invert scattered intensities, which will provide a 2D projection of the position of the atomic columns in the sample as well as the shape function $s(\mathbf{r})$. This information is encoded in the Bragg peak positions $\mathbf{g}_n$ and in the function $S(\mathbf{q})$.

When the crystal is of a certain size, the formfactor $S(\mathbf{q})$ has appreciable values for the magnitudes of $\mathbf{q}$ that are much less than the reciprocal lattice parameters. Therefore the experimentally measured intensity from a finite crystal will be determined by a sum over the reciprocal lattice points

$$I(\mathbf{q}) = \frac{|F(\mathbf{q})|^2}{V^2} \sum_n |S(\mathbf{q} - \mathbf{g}_n)|^2 \tag{1.31}$$

where the small cross terms are neglected [GYWV11]. In the vicinity of a reciprocal lattice point, for which the Laue condition $\mathbf{q} = \mathbf{g}_n$ is fulfilled the intensity distribution is given just by one term of this sum and represents the FT of the shape function. It is important to note here the difference between a strained and an unstrained crystal. For an unstrained crystal the intensity distribution around the Bragg peaks is locally centrosymmetric, and has the same shape for every reciprocal lattice point $\mathbf{g}_n$, which is explained in detail in [VR01a]. The next section will give an overview on strain which is mainly induced by defects in a crystalline material.

1.3.3 Influence of Defects and Strain

The previous parts concentrated mainly on perfect crystals. If the regular crystal structure has discontinuities they are called defects. This subsection will focus on different defects that can occur in crystals and the influence of strain induced, for example, by defects. Due to thermo-dynamics, it is very hard to find perfect crystals in nature. The defect structure can define the physical properties of the material, like strength, electrical-, and thermal conductivity. Defects in crystals can be divided into three main groups, point defects, line defects, and plane defects.

Point defects are defects that only occur around a single lattice point. One example for a point defect is a vacancy, where a lattice site, which would be occupied in a perfect crystal, is empty, see Figure 1.12(b). An atom might also be located at a position that is not within the regular lattice. Such a defect is called an interstitial defect and is also visualized in Figure 1.12(b). A vacancy can also be occupied by an atom from another

type, then the defect is called an impurity. This is exploited in semiconductors, where for example the important pn-junction is created by different doping of crystals. All of these point defects result in a change of the diffraction pattern. Due to the break of the perfect crystal lattice the interference is not perfect and forbidden peaks as well as diffuse scattering can appear. Depending on the density of the defects Bragg peaks can be less intense or broadened.

A defect is called a line defect when atoms are misaligned along a defect [HL82]. There are two types of line defects edge dislocations and a screw dislocation. An edge dislocation is a defect, where one crystal plane stops in the middle of the crystal. The neighbouring planes are slightly distorted, but the crystal structure is still perfectly ordered on either side, as can be seen in Figure 1.12 (c). To characterize dislocations the Burgers vector is introduced. The Burgers vector is a measure for the extent of the deformation of the lattice. It is constructed considering a perfect crystal lattice, where a closed circuit is drawn starting at a random particle and taking n steps of the lattice constant. For the case that this circuit surrounds a dislocation after n steps a gap remains. The vector, which is required to close this gap is the Burgers vector **b**. For the described edge dislocation the Burgers vector is perpendicular to the defect. In Figure 1.12(c) the Burgers vector is shown in red. The other type of line defect is a screw dislocation, where the dislocations are happening around the defect line in a helix shaped fashion. For a screw dislocation the Burgers vector is parallel to the defect. A line defect distorts the diffraction pattern and a distinct plane with high intensities appears in reciprocal space.

common 2D defect are grain boundaries, which are called plane defects. In a grain boundary the crystallographic direction of the lattice changes abruptly, which happens, when two crystals meet during growth. Another relevant plane defect is a stacking fault. Stacking faults will be explained here using the example of a close packed structure as introduced in section 1.3.1. A break in the stacking of the layers, for example **ABCA-CABC**, where a **B** layer is missing, is called an intrinsic stacking fault, in contrast to an extrinsic stacking fault, where an extra layer would be introduced into the lattice. This is shown in Figure 1.12(d). It is common in layered structures to encounter stacking faults, but they rarely occur in isotropic structures. Stacking faults can be described as a displacement (slip) of an entire plane of atoms perpendicular to the fault plane, so that the fault is described by two vectors: the stacking vector (perpendicular to the fault plane) and the slip vector, describing the displacement direction of the plane of atoms. The slip vector plays a similar role as the Burgers vector in the characterisation of defects. The diffraction pattern of a crystal containing a plane defect will have strong streaks connecting the corresponding Bragg peaks. The surface of a crystal is an obvious imperfection, and, due to the extend in two dimensions, can be called a plane defect. For the scattering off the surface where the crystal is truncated the streaks in reciprocal space are called crystal truncation rods CTR [Rob86, AAF$^+$86].

All defects induce some strain in the crystal lattice, which means that the lattice is distorted and shear forces influence the material behavior. Strain can also be induced when a crystal from a material (e.g. Ge) is grown on top of another material (e.g. Si). In this case, at the boundary, the difference in the lattice parameter has to be compensated.

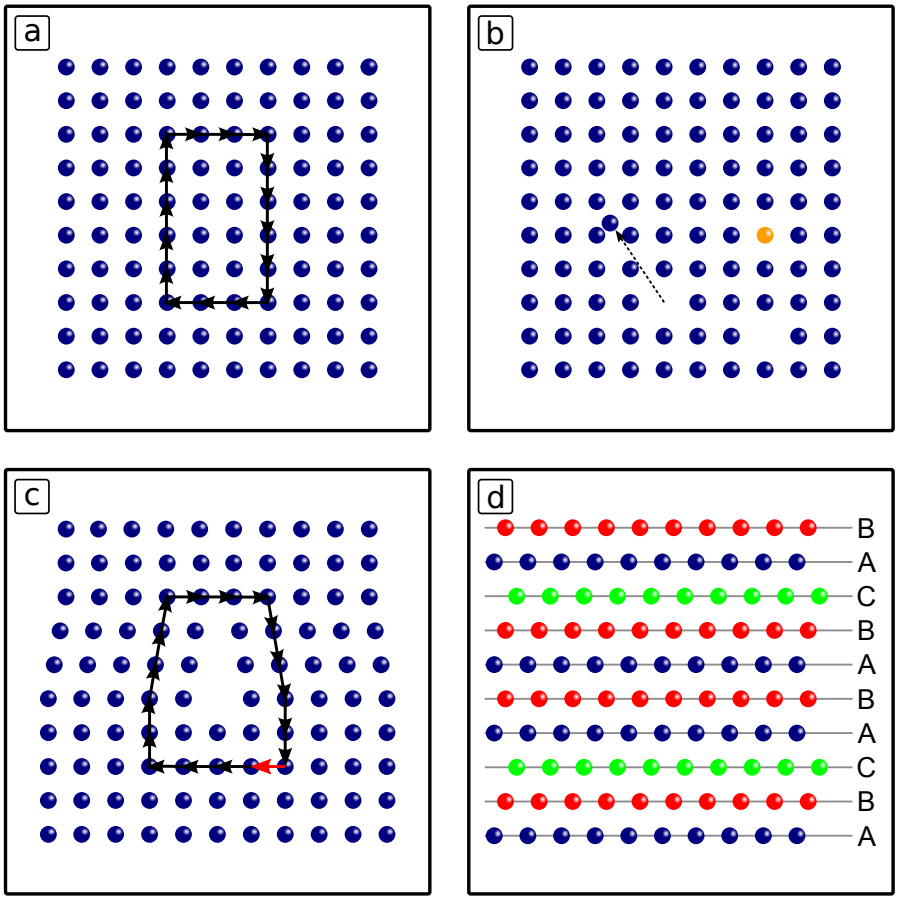

Figure 1.12: A schematic illustration of defects in a crystal, looking along the crystal axis, each sphere represents a column of atoms. (a) shows a flawless crystal. (b) shows different point defects, for example, showing a vacancy defect indicated by a missing atom. The misplaced atom is illustrating an interstitial defect, the yellow colored atom represents an atom of a different kind and shows an impurity. (c) visualizes a line defect, the shown defect propagates along the entire column of atoms. In addition, the Burgers vector is drawn, compare to panel (a). (d) shows a stacking fault as a break in the regular crystal planes.

Depending on the strain in the crystal the intensity distribution around Bragg peaks can become asymmetric. The local measurement around a selected Bragg peak can reveal a continuous distribution of the electron density and strain inside a crystal, as it was demonstrated in [PWV$^+$06].

To examine the impact of strain in a crystal on the diffraction signal the following explanation is a helpful guide. The electron density of a strained crystal is expressed as a sum of terms corresponding to the individual atoms (compare with equation (1.21))

$$\rho(\mathbf{r}) = \sum_{n=1}^{N} \sum_{j=1}^{S} \rho_{nj}(\mathbf{r} - \mathbf{R}_{nj} - \mathbf{u}(\mathbf{R}_{nj})), \tag{1.32}$$

where as before $\mathbf{R}_{nj} = \mathbf{R}_n + \mathbf{r}_j$ and $\mathbf{u}(\mathbf{R}_{nj})$ is the displacement from the ideal lattice point. The summation is carried out over all N unit cells, which are coherently illuminated. This electron density is substituted in equation (1.12) and the corresponding variables are changed, then the scattering amplitude becomes

$$A(\mathbf{q}) = \sum_{n=1}^{N} F_n(\mathbf{q}) e^{-i\mathbf{q}\cdot\mathbf{u}(\mathbf{R}_n)} e^{-i\mathbf{q}\cdot\mathbf{R}_n}, \tag{1.33}$$

where $F_n(\mathbf{q})$ is the structure amplitude of the n-th cell. It is also assumed in equation (1.33) that all atoms in the unit cell are displaced equally $\mathbf{u}(\mathbf{R}_{nj}) \equiv \mathbf{u}(\mathbf{R}_n + \mathbf{r}_j) = \mathbf{u}(\mathbf{R}_n)$. This equation is very general and can now be applied to finite sized crystals using the same approach as before. The scattering amplitude can be written as [VR01b]

$$A(\mathbf{q}) = F(\mathbf{q}) \sum_{n=1}^{\infty} \sigma(\mathbf{R}_n) e^{-i\mathbf{q}\cdot\mathbf{R}_n}, \tag{1.34}$$

where a complex valued shape function

$$\sigma(\mathbf{r}) = s(\mathbf{r}) e^{-i\mathbf{q}\cdot\mathbf{u}(\mathbf{r})}, \tag{1.35}$$

has been introduced. It has the amplitude $s(\mathbf{r})$ (the shape function as defined in equation (1.22)) and the phase $\phi(\mathbf{r}) = \mathbf{q} \cdot \mathbf{u}(\mathbf{r})$, which contains the deformation field $\mathbf{u}(\mathbf{r})$.

As before this is substituted into equation (1.26) and for a crystal with macroscopic dimensions this results in the periodic function

$$A(\mathbf{q}) = \frac{F(\mathbf{q})}{V} \sum_{n} S(\mathbf{q} - \mathbf{g}_n), \tag{1.36}$$

where $S(\mathbf{q})$ is the FT of the complex shape function $\sigma(\mathbf{r})$. Here each term gives the intensity values close to a reciprocal lattice point. When the Laue condition is fulfilled for the selected Bragg peak the scattering amplitude reduces to

$$A(\mathbf{q}) = \frac{F(\mathbf{q})}{V} \int s(\mathbf{r}) e^{-i\mathbf{h}\cdot\mathbf{u}(\mathbf{r})} e^{-i\mathbf{q}\cdot\mathbf{r}} d\mathbf{r} \tag{1.37}$$

This expression indicates that the scattering amplitude is directly connected to the complex shape function $\sigma(\mathbf{r})$. The phase factor, due to strain, in this expression is a source of an asymmetric intensity distribution at the Bragg positions. The phase of the reconstructed electron density can then be attributed to the strain field inside the crystalline material. This has been shown in [PWV+06] where by inverting the three-dimensional distribution of the diffracted intensity around a Bragg peak the shape and strain field inside a crystalline lead particle was obtained with 40 nm resolution.

X-ray diffraction is a useful technique to characterize defects in crystals. A broad field of science has emerged from the knowledge of the inner structure of matter. Several methods have been developed to model diffraction patterns from crystals containing different defects. Up to now, however, there is no direct (model free) approach to visualize and measure the location of defects in a crystal as well as the positions of the individual unit cells around the core of the defect.

1.4 Coherent Diffraction Imaging

In this section a brief introduction into the field of coherent diffraction imaging also known as lensless imaging is presented. Various physical aspects related to the method, including the phase problem, resolution, and different phase retrieval algorithms, will be introduced. Coherent X-ray Diffractive Imaging (CXDI) is a relatively novel imaging method that can produce an image of a sample without using any optics between sample and detector. Using phase retrieval algorithms an image of the sample can be reconstructed. This differs from conventional microscopy schemes, which use objective lenses to produce an image of the object. Since it is very difficult to produce lenses for hard X-ray energies, the lensless approach surpasses this problem. The lenses are substituted by powerful algorithms which reconstruct an image of the sample.

Figure 1.13(a) shows the most basic concept for a small angle X-ray coherent scattering experiment. A coherent plane wave of X-rays passes through the sample and is disturbed by the electron density, thus behind the sample an exit surface wave is created. This disturbed wave field now contains information about the sample. The amplitude of this field can be attributed to the projected electron density of the sample and, as described in the previous section, the phase to the strain field. The propagated wave field will be recorded in the far field by a 2D detector. First proof of principle experiments showed the great potential of this method on a test object [MCKS99] as well as on biological samples [MHI+03], where a resolution better than 50 nm was demonstrated. This was achieved with an experimental setup as simple as shown in figure 1.13(a).

Another milestone was the application to crystalline samples. Crystalline samples produce, as discussed before, a periodic scattering pattern. As shown in section 1.3.3 around each Bragg peak the local scattering pattern contains information about the shape and the strain of the crystalline sample. It was also explained that this information is encoded through a Fourier transform of the projected complex electron density of the sample into the direction of the Bragg peak. Figure 1.13(b) schematically shows the experimental idea of measuring the coherent scattering pattern around a certain Bragg

peak, also called Bragg CDI. Again it is assumed that a coherent plane wave passes through the now crystalline sample and the Fourier transform of the exit surface wave (ESW) is now measured at a certain Bragg angle α. The diffraction pattern can be measured at any of the possible Bragg peaks, depending on the orientation of the sample. One advantage of this method is the possibility to measure without a beamstop, since the direct beam does not hit the detector. This enables to measure all low frequency data in reciprocal space which is normally missing in a coherent small angle scattering experiment. This approach has been experimentally proven first in [PWV$^+$06], where the strain field inside a lead nano crystal near the melting point was measured. Here another virtue of this method comes into play. The Bragg peaks of the randomly orientated lead islands appear at different positions and for a certain Bragg peak only the scattering from a single island is measured. This can be done even though the rather large X-ray beam illuminates a substantial part of the substrate, with several of the lead island. The method of Bragg CDI has been extended later to other objects like nano rods [NHR10]. Here different Bragg peaks from the sample were inverted independently revealing the strain field in several directions inside the nano rod.

1.4.1 Phase Retrieval

Before explaining phase retrieval the phase problem has to be introduced. A measurement will always yield the scattered intensities $I(\mathbf{q}) = (A(\mathbf{q}))^2$, therefore all phase information of the scattered amplitude is lost, this is called the phase problem. If the phases in the reciprocal space are known a simple back transformation will reconstruct the projected electron density of the sample. It is however possible to retrieve these phases, for example, through iterative algorithms, which will be introduced and explained here.

The minimum requirement for the iterative phase retrieval algorithms is a sufficiently sampled diffraction pattern. This means that in reciprocal space the smallest features which correspond to the largest size in the real space have to be known at least at two points within one oscillation period. According to the Nyquist theorem these two points are sufficient to uniquely identify the oscillation frequency. For practical purposes a higher sampling rate is preferred, since it increases the number of known variables, which can be used to solve for the unknowns. The unknowns are the phases of the diffraction pattern. An iterative scheme was first proposed by Gerchberg and Saxton [GS72] and later developed by Fienup [Fie82]. Over the decades several numerical phase retrieval methods have been implemented [Mar07].

Figure 1.14 schematically shows the principle of the iterative reconstruction algorithm. The iterative phase retrieval approach was originally introduced in astronomy and electron microscopy. The first iterative phase retrieval algorithm proposed in 1972 [GS72] is called the Gerchberg & Saxton (GS) algorithm.

To explain this procedure it is assumed that the incoming X-ray beam is expressed by the plane wave front $E_{in} = A\exp(i\Phi)$. This wave is then modified while propagating through the sample by the electron density $\rho(\mathbf{r})$ of the sample and finally the exit wave has the form $E_{EW}(\mathbf{r}) = A(\mathbf{r})\exp(i\Phi(\mathbf{r}))$, where $\mathbf{r} = x, y$ are the coordinates in real space. By propagating the exit wave to the far field ($Z \gg D^2/\lambda$) the wave field at the

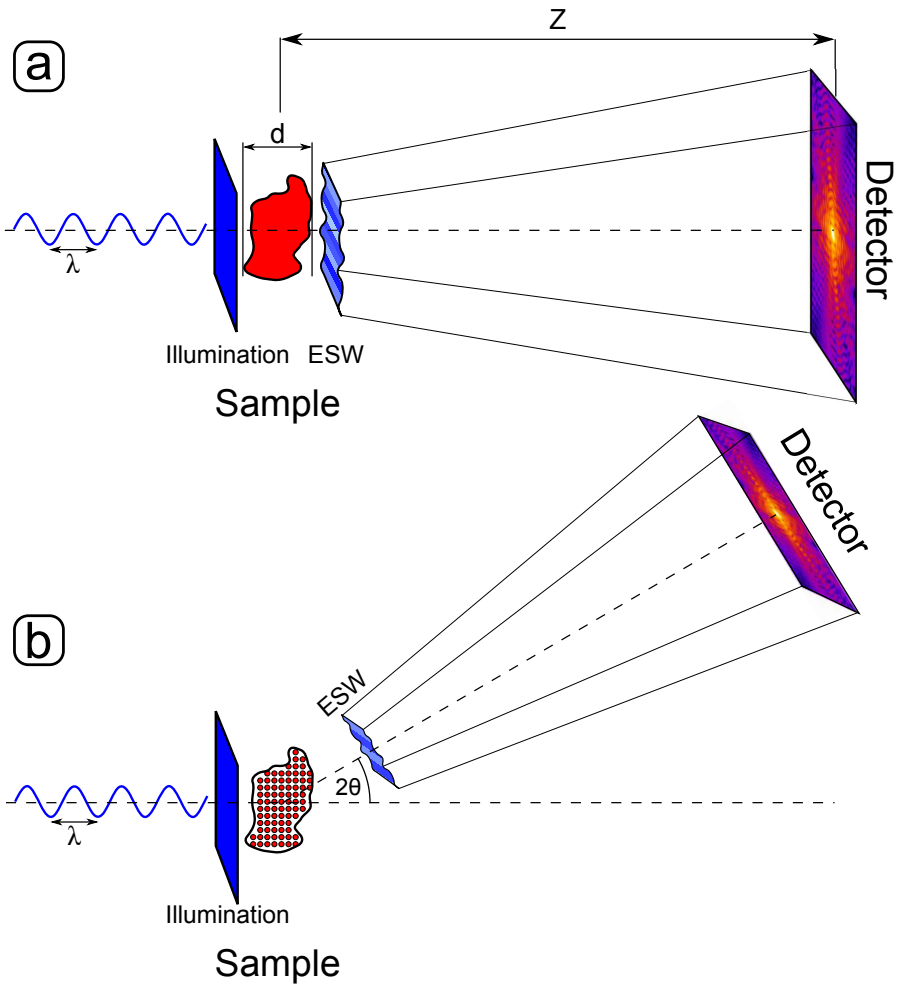

Figure 1.13: The concept of coherent scattering experiments. (a) - small angle CDI, a coherent plane wave illuminates the sample. The coherence length of the X-rays has to be larger than the extent d of the sample. A two dimensional diffraction pattern is measured after a distance Z under far field conditions. (b) - Bragg CDI. For the case of a crystalline sample a diffraction pattern around a Bragg peak can be measured at the Bragg angle α.

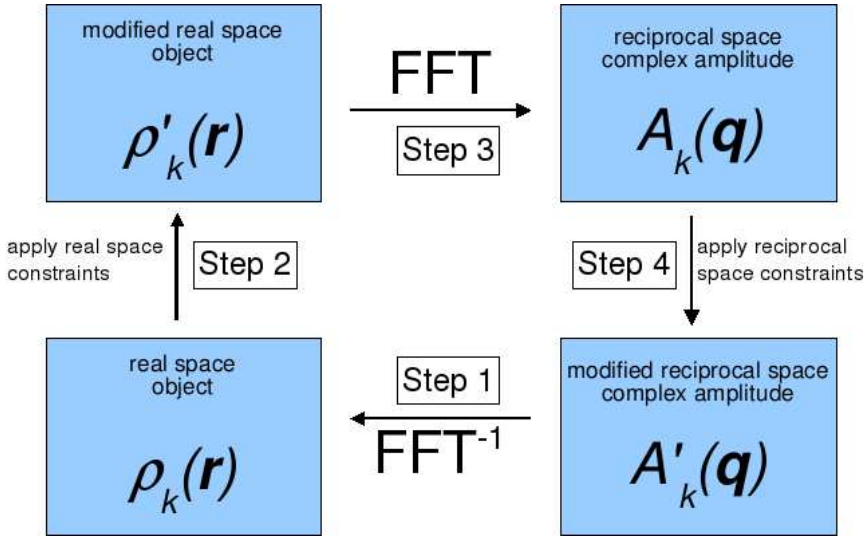

Figure 1.14: The iterative phase retrieval scheme.

detector can be expressed by the Fourier transform of the exit wave

$$A_{det}(\mathbf{q}) = \mathcal{F}\{E_{EW}(\mathbf{r})\}, \tag{1.38}$$

where $\mathcal{F}$ denotes the 2D Fourier transformation and $\mathbf{q} = q_x, q_y$ are the coordinates in reciprocal space. A laterally displaced object and the inverted complex conjugated object, the so-called twin image, have the same modulus of the Fourier transform and yield the same diffracted intensities. These trivial solutions also solve the inverse problem as described in [Bat82], this will be explained in more detail later.

The iterative process of phase retrieval starts with the measured intensities $I_M(\mathbf{q}) = |A_{det}(\mathbf{q})|^2$. The goal is to recover the entire complex wave field in reciprocal space

$$A_{det}(\mathbf{q}) = |A_{det}(\mathbf{q})|\, e^{i\phi_{det}(\mathbf{q})},$$

of which, up to now, only the amplitude is known. To seed the algorithm a random set of phases $\phi_{rnd}(\mathbf{q})$ is assigned to the measured amplitudes

$$A_{fg}(\mathbf{q}) = \sqrt{I_M(\mathbf{q})} \cdot e^{i\phi_{rnd}(\mathbf{q})}. \tag{1.39}$$

This, now complex, diffraction pattern is called the *first guess (fg)* and is transformed by an inverse Fourier transformation to a *first guess* of the object in real space

$$\rho_1(\mathbf{r}) = \mathcal{F}^{-1}\{A_{fg}(\mathbf{q})\}. \tag{1.40}$$

Step 1

On the next step constraints in real space are applied. These constraints can be derived

from a priori knowledge about the sample. They modify $\rho_1(\mathbf{r})$ in a non-linear way and yield a modified $\rho_1'(\mathbf{r})$. Step 2 is also known as the support constraint.

The properties of $\rho_1'(\mathbf{r})$ are closer to the actual properties of the object. With the Fourier transformation in the next step the diffraction pattern of $\rho_1'(\mathbf{r})$ is calculated,

$$A_1(\mathbf{q}) = |A_1(\mathbf{q})| \cdot e^{i\phi_1(\mathbf{q})} = \mathcal{F}\{\rho_1'(\mathbf{r})\}. \tag{1.41}$$

Step 3

The amplitudes in reciprocal space are known from the measurement. The measured amplitudes are multiplied with the phase information $\phi_1(\mathbf{q})$ obtained in the previous step

$$A_1'(\mathbf{q}) = A_{det}(\mathbf{q}) \cdot e^{i\phi_1(\mathbf{q})}. \tag{1.42}$$

Step 4

This is called the reciprocal space constraint and can be of a more complicated nature. This fourth step concludes the cycle. A *second guess* of the object is obtained by repeating step one:

$$\rho_2(\mathbf{r}) = \mathcal{F}\{A_1'(\mathbf{q})\} \tag{1.43}$$

These four steps are repeated for a finite number of iterations.

A limitation of this method is the convergence for a given diffraction pattern. The convergence might be very slow, depending on the starting phases and input, and might even stagnate before converging to the solution. To increase the performance of the algorithm more sophisticated constraints in real space can be applied.

1.4.2 Error Reduction Algorithm

The very general GS algorithm has been modified by Fienup into the so called Error Reduction (ER) algorithm [Fie82]. The ER algorithm uses the information that the object is isolated and of finite size. A support S is defined with the same dimensions as the object. In Step 2 the support is applied as the constraint in real space. Outside the support all reconstructed real space amplitudes are set to zero. With the ER algorithm in each iteration the modified real space object $\rho_k'(\mathbf{r})$ is calculated by

$$\rho_k'(\mathbf{r}) = \begin{cases} \rho_k(\mathbf{r}), & r \in S \\ 0, & r \notin S \end{cases} . \tag{1.44}$$

This means that for a successful reconstruction with the ER algorithm the size and shape of the object have to be known beforehand. An estimate for the size might be derived from the speckle size. The shape of the sample can be retrieved from the autocorrelation function. When the object is considered to be real, all phases in real space are set to zero in Step 2 as well. This neglects all refraction effects in the scattering process. Most objects have to be treated as fully complex since they alter the phase of the passing X-

ray wave field. The reconstruction of a fully complex object normally converges slower. A very tight support helps the algorithm to converge, since only a limited number of solutions will satisfy this support constraint.

The ER algorithm performs well if a known tight support is applied. The solution strongly depends on the chosen support and will result in a faulty reconstruction if the support is not very close to the actual object. The main disadvantages are that the algorithm tends to stagnate in local minima and the convergence is very fast for the first few iterations after which the error only very slowly decreases.

1.4.3 HIO Algorithm

To overcome the problem of stagnation in local minima and slow convergence the error reduction algorithm can be extended by introducing a memory from the previous iteration step. One of these algorithms is the hybrid-input-output (HIO) algorithm first introduced by Fienup [Fie82]. In this algorithm the current object guess $\rho_k(\mathbf{r})$ is considered as the input of a non-linear operation driving the output $\rho'_k(\mathbf{r})$. This can be achieved when the second step described above is replaced by:

$$\rho'_k(\mathbf{r}) = \begin{cases} \rho_k(\mathbf{r}), & \mathbf{r} \in S \\ \rho_k(\mathbf{r}) - \beta\rho'_{k-1}(\mathbf{r}), & \mathbf{r} \notin S \end{cases} \tag{1.45}$$

The parameter β satisfies the condition $0 \leq \beta \leq 1$ nd for $\beta = 1$ the HIO algorithm is identical to the ER algorithm. Best results are typically achieved with $\beta \approx 0.8$ [Fie82, MS97]. In these papers it was also reported that, due to the less prescribed properties of the real space constraint, this algorithm converges faster in the case of the ER method either stagnating or failing to find a solution. Since the HIO allows real space amplitudes apart from zero outside the support it is useful in practice to use both algorithms ER and HIO in alternation [RVW$^+$01]. The ER algorithm cleans up the result of the HIO algorithm, which in turn helps to escape local minima.

Even though a large variety of variations of the standard iterative method exist, and not all can be covered here, one in particular should be mentioned. It was used in the work presented later and is known as the Guided Hybrid Input-Output (GHIO) method [CMWL07]. It uses the fact that usually several reconstructions are run in parallel anyway to verify a reconstruction result. After running N reconstructions in parallel, the best result is chosen through convergence criteria which is then used to seed a subsequent set of reconstructions through the expression

$$s^{g+1,n}(\mathbf{r}) = \sqrt{s^{g,template}(\mathbf{r}) \times s^{g,n}(\mathbf{r})}, \tag{1.46}$$

where n denotes a given family in the reconstruction and g is the generation. For the next generation again N iterative phase retrieval runs are started. This process is repeated several times until the desired convergence criteria are met. The GHIO algorithm still adheres the disadvantage that a very precise support has to be known a priori.

1.4.4 Shrink-Wrap Method

A main disadvantage of the methods described before is the need to know the size of the object beforehand. The real space support is the key parameter in the reconstruction algorithm. If this real space constraint converged during the reconstruction to the size of the object, this problem would be solved. In 2003 Marchesini et al. [MHC$^+$03] proposed an extension to the algorithms described before, the so called shrink-wrap algorithm. For the first few iterations a support is derived from the autocorrelation function. Even an arbitrarily chosen support can be used. Every M iterations the support is updated. Typical values for M are 20 to 50 iterations, whereas M can also be varied throughout the reconstruction process. The new support is deduced from the current estimate of the object. By convolving $\rho(\mathbf{r})$ with a Gaussian function the object guess is smeared to avoid artifacts. Then the pixels with an absolute value larger than a threshold are defined as inside the support. This threshold is normally set between 10% and 20% and defines the support progressively during the iterative process. The shrink-wrap method does not work for objects with smooth edges, where the electron density of the object slowly falls off to zero, and also has problems with objects that inhabit vacancies, since the algorithm seems to increase the size of the holes. The number of reconstruction iterations used between the application of the shrink-wrap algorithm can differ and has to be chosen manually for each case to receive the best results. Recently, it has been proven viable to vary the width of the Gaussian function used for smearing. The width should decrease in each step. The field of phase retrieval algorithms is very dynamic and new algorithms emerge regularly. A good review of recent work can be found in [Mar07, MYV10]. However, it is still limited to isolated objects or finite illumination functions. For further applications, for example in biology, extended objects are relevant.

1.4.5 Resolution

The resolution in CDI is theoretically only limited by the wavelength of the photons that take part in the scattering process. Practically however, the limit is set by the biggest scattering angle where a significant signal can be measured. Consequently the resolution is limited by the signal to noise ratio or the size of the detector. However, the phase retrieval algorithms do not always converge to the highest resolution image. Therefore the resolution is also limited by the quality of the reconstruction.

One way to quantify the resolution is to determine the correlation between phases retrieved from independent random starts of the phase retrieval algorithm. Due to the ability to start an almost infinite number of reconstructions this is not a feasible measure for determining the resolution. A commonly accepted way to compare the resolution of different reconstruction algorithms is the phase retrieval transfer function (PTRF). The PRTF computes the average of the independent complex reconstructions and the squares of the Fourier amplitudes of this average are compared with the measured diffraction intensities [CBM$^+$06]. The average $<>$ of several reconstructions is calculated

$$\bar{\rho}(\mathbf{r}) = \langle \rho_j(\mathbf{r}) \rangle \tag{1.47}$$

where $\rho_j(\mathbf{r})$ is the result of the j-th independent reconstruction. The PRTF is then defined as

$$\mathrm{PRTF}(\mathbf{q}) = \frac{|\mathcal{F}[\bar{\rho}](\mathbf{q})|}{\sqrt{I_M(\mathbf{q})}}, \tag{1.48}$$

where $\mathcal{F}$ denotes the Fourier transform and $I_M(\mathbf{q})$ are the measured intensities at the detector. This yields a very good way to evaluate the fidelity of a reconstruction, now including all effects from the maximum scattered angle, over the artifacts in the detector, to the quality of the reconstruction algorithm.

1.4.6 Uniqueness

There is no direct method to determine the phase information in reciprocal space. Therefore the uniqueness of the solutions of the phase retrieval algorithms has to be addressed. In general, it is difficult to verify the correctness of the reconstructed object. In practice, SEM, or optical microscopy images, are used to verify the reconstruction. It has to be proven that the reconstructed phases by the iterative phase retrieval algorithms are in fact the only (correct) solution to the phase problem.

For a measured set of scattered intensities $I(\mathbf{q})$ the general properties of the Fourier transformation give three possible real space solutions. The correct solution shall be $\rho(x, y)$, but the shifted object $\rho(x + x_0, y + y_0)$ also has the same modulus of the Fourier transformation. In addition, the modulus of the Fourier transform of $\rho^*(-x, -y)$ and $e^{i\varphi}\rho(x, y)$ are identical to the measured scattered intensities from $\rho(x, y)$. This can cause problems in the reconstruction procedure since, either the correct object, a lateral displaced object, the inverted complex conjugated object, or the object multiplied with a constant phase factor can be the result of the reconstruction [Bat82]. The physical interpretation of the result is important to distinguish different cases.

Clearly the displaced object cannot be reconstructed once the support is tight enough to define the position of the object. A constant offset of the phase of the reconstructed object also does not hinder the interpretation of the physical meaning of the sample. This only causes problems when trying to compare different reconstructions, where an absolute phase value is needed. Of particular importance is the inverted complex conjugated object, which is also known as the twin image. For very symmetric objects it is possible that a superposition of the object and its twin image is reconstructed. Normally this can be prevented by using an asymmetric support, which pushes the reconstruction towards one solution. To sum up, except for very rare cases, the reconstruction algorithms always converge to the unique correct solution [Bat82, MS97].

1.4.7 Ptychography and Other Algorithms

For the sake of completeness other phase retrieval methods, that have not been used in this work, should be mentioned. The most prominent one is ptychography, which uses a finite illumination on an extended object. The illumination can be achieved using an aperture in front of the sample, or a nano/micro focused X-ray beam, which only illuminates a part of the sample. This is illustrated in Figure 1.15(a), where the sample

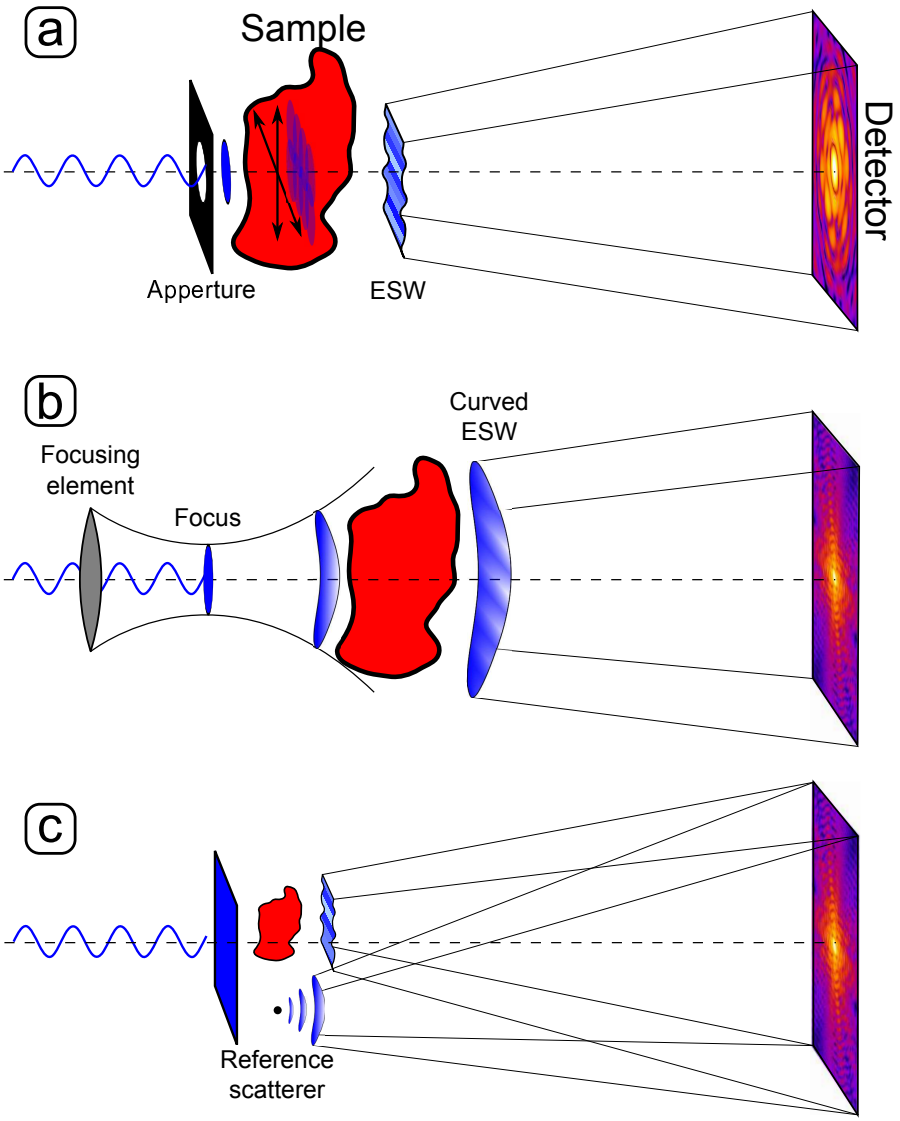

Figure 1.15: Three different phase retrieval methods. (a) Ptychography, an aperture is scanned across the object with overlapping illuminated regions. (b) FCI, a strongly divergent beam is used to carry the phase information. (c) FTH, a scatterer near the object creates a reference wave.

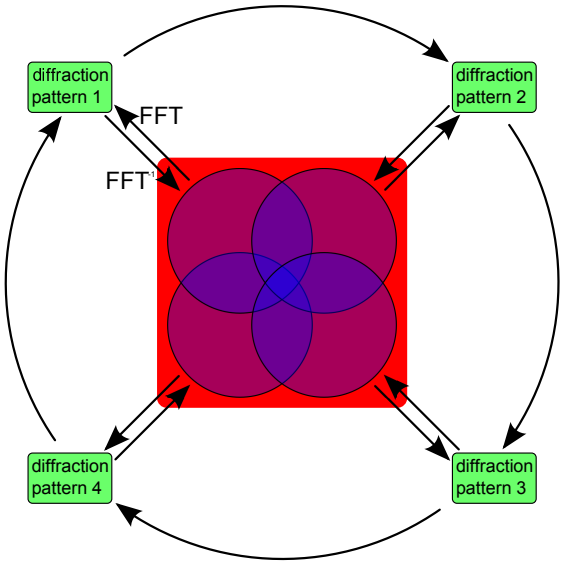

Figure 1.16: A shematic graph of the ptychographic reconstruction algorithm.

is illuminated at different locations by a round illumination function indicated by the blue circles. By scanning the illumination over the object several diffraction patterns can be collected, which correspond to different regions on the sample. The crucial constraint is that the individual scan points are separated by less than the illuminated area. This supplies redundant information about the area where two illumination functions overlap. This constraint can be used as a real space constraint Step 2 since one part of the reconstructed object is already known from another reconstruction. By applying this constraint on each iteration step and also looping over all the scan points, an image of the sample will be reconstructed. In this method all the scan points on the sample are reconstructed simultaneously. Figure 1.16 schematically shows how the ptychography algorithm works. Here the double arrows represent a single iteration of the classical CDI algorithms. The big outer circle represents the big loop over all scan positions on the sample. This method was first proposed for coherent electron diffraction [RF04], but was quickly picked up by the X-ray community. First results showed the extremely fast and robust convergence of the algorithm [RHC$^+$07, TDM$^+$08, DBK$^+$08]. One of the most remarkable results has been the three dimensional reconstruction of bone structure [DMT$^+$10], where not only the osteocyte lacunae and the interconnective canalicular network were clearly seen with a resolution of 100 nm in 3D, but also the recovered electron density map provided a contrast high enough to estimate the nanoscale bone density variations with less than one per cent.

An additional advantage besides the very good convergence of the ptychography algorithms, is the automatic reconstruction of the illumination function [TDM$^+$08]. This can be exploited by using a well known and simple object to characterize a beam profile, e.g. of a nano focused beam with very good resolution [SBF$^+$10], which otherwise could

not be accessed by other means. Since a bigger overlap, with more redundant information leads to better results, a compromise between resolution and radiation damage has to be found. However, it is important to note that due to the necessary overlap most regions of the sample are illuminated more than once, exposing these areas to a higher dose of lethal radiation. The disadvantage of a higher dose is often overcome by the advantage of the extended scan regions, allowing the measurement of micron samples with nano focused X-ray beams, assuming that the sample does not change over time. The size of the scan region is only limited by the stability of the setup, but also becomes very demanding on computational methods, since many diffraction patterns have to be reconstructed in parallel.

Another method for phase retrieval is Fresnel Coherent Diffractive Imaging (FCDI). A strongly focused X-ray beam is used to create a diverging wave front, which is illustrated in Figure 1.15(b). The sample is located behind the focus and is illuminated by the significantly curved wave. This allows the divergent beam to carry the diffracted information, which assists in the iterative reconstruction of the sample's exit surface wave, provided that the incident field is well characterized. FCDI can of course be combined with scanning techniques e.g. ptychography. This modification also removes the restriction of imaging only finite objects by creating a finite illumination with the focused beam allowing to image parts of objects embedded within larger samples. Even scanning is an option to a increase the field of view. FCDI has been demonstrated for a variety of samples, including biological samples like a malaria infected red blood cell [WHP$^+$08].

The last coherent imaging technique to be mentioned here is holography. The distinctive feature of holography is to artificially encode the phase information in the diffraction pattern. Different methods have emerged, but they all rely on the high degree of coherence. One way of encoding the phase information uniquely in the diffraction pattern is to use a reference scatterer near the object. This is shown schematically in Figure 1.15(c). The reference wave interferes with the diffracted wave from the object. The reference scatterer can be an aperture near the object or another small, strongly scattering object. Then a simple back Fourier transform of the diffraction pattern reveals the object. This method is known as Fourier Transform Holography (FTH). The constraints on this method are, however, rather strict. The reference scatterer has to be positioned farther away than the lateral dimensions of the object itself, the diffracted intensities from the reference scatterer have to be of similar magnitude as the scattered intensities from the object, and the resolution is limited by the size of the reference scatterer. However, especially due to the simplicity of the very robust Fourier inversion method several results have been obtained at synchrotron [SGA$^+$09, CSC$^+$10] and free-electron laser [MGS$^+$10, ELS$^+$04] sources.

The use of coherent photons from modern X-ray sources has just begun. By overcoming the phase problem many interesting questions in physics, but also in biology and other fields of science, can be answered with hitherto unknown precision. Now it is important to apply these robust and successful algorithms to many new samples to prove the diversity of the possible applications. One field, though, is completely left out by the techniques discussed so far, namely the imaging of crystalline samples with

defects. Some of the methods mentioned before even rely on the crystallinity of the sample (Bragg CDI) but are not able to depict the core of the defects. That is the possibility to image the individual unit cells in the crystal, especially around defects, to better understand the process of growth and strain in the sample. The following chapter will present a completely new method, which, by combining small angle CDI and Bragg CDI, allows to exactly address these questions.

2 Small Angle Bragg - Coherent Diffractive Imaging

The measurement method introduced in this thesis is novel in the sense that the classic two kinds of CDI, small-angle CDI and Bragg CDI see Figure 1.13 are performed at the same time. Due to the ability to measure the Bragg peaks under a relatively small angle together with the coherent scattering signal between the peaks, this method was named Small Angle Bragg Coherent Diffraction Imaging (SAB - CDI). This type of CDI is extremely interesting for all nanostructured materials, e.g. assemblies of block copolymers, micelles, colloids, nanoporous materials, nanoparticles or in other words, for all samples that feature superlattice Bragg peaks in the small-angle scattering region. CDI permits to investigate what is hard to do with scattering alone, namely obtaining information on the 3D object shape, morphology, and defect structure. This thesis opens a new window of opportunity for the field of coherent scattering for the investigation of matter.

If a sample has some internal regular structure in the scattering signal Bragg peaks will appear, as discussed before for crystals. This, however, still applies for all nanostructured samples. The Bragg peaks are observed on top of the small angle scattering signal of the sample, and thus enhance the signal for high q values. This results in a higher resolution in the reconstruction. The new synchrotron radiation sources, which have only become available very recently, inhibit coherence lengths, which exceed those of older sources significantly. This opens up the opportunity to measure the coherent interference signal of the size and shape of the crystal together with the Bragg peaks from the internal regular structure.

An inversion of the diffraction pattern around a single (111) Bragg peak of a Pb crystal was used in [PWV$^+$06] to reconstruct the shape and strain field in a submicron particle. These local measurements around a selected Bragg peak can reveal only a continuous distribution of the electron density and the strain inside a crystalline sample. Here it is proposed, instead, to measure diffraction patterns originating from a nanocrystaline sample with several Bragg peaks and the coherent scattering signal between the peaks. This can be inverted to an image of the crystal, revealing the positions of the atomic columns.

In practice, the experimental realization of these ideas is not quite as straightforward. It is desirable to measure several Bragg peaks simultaneously on one detector, for a fixed position of the sample requiring short wavelength X-rays. With typical atomic distances in crystalline materials this will require energies in the range of 100 keV [Gul08]. High energy electron beams can also be used to image the structure of nanocrystals with this coherent imaging technique [HZJ$^+$09, DLS$^+$09]. Still, as for most electron scattering

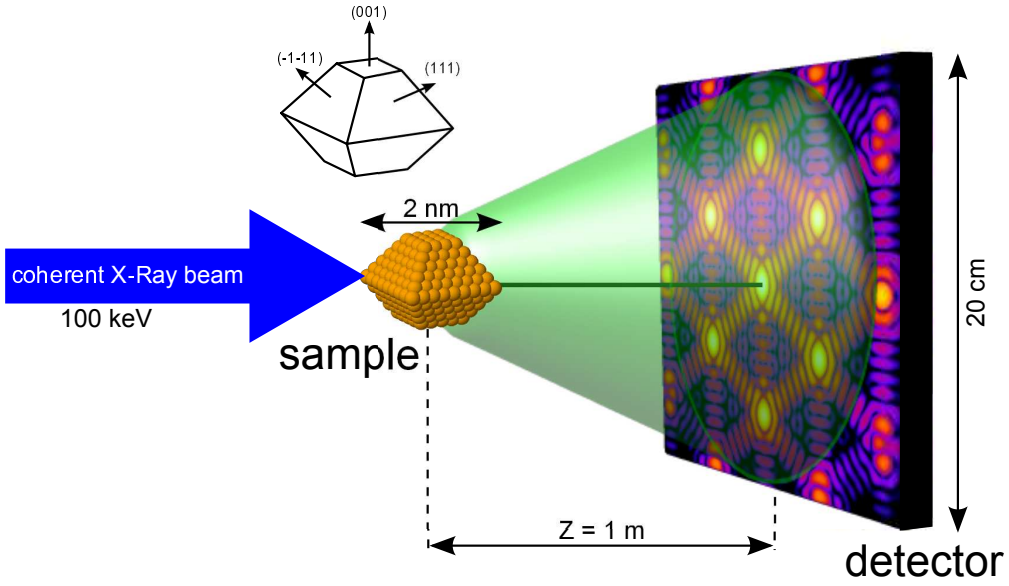

Figure 2.1: A schematic view of the experiment and parameters used in the simulations.

methods, this approach is limited to small samples in the range of few tens of nanometers. One possible approach for X-ray scattering methods is to use long periodic structures. This is conveniently provided by nature in the form of colloidal crystals with a period in the range of a few hundred nanometers. Illuminating such samples with hard X-rays produces a diffraction pattern with many Bragg peaks mapped simultaneously on a two-dimensional (2D) detector [PDA+03] and provides a convenient way to study the arrangement of colloidal particles.

The following simulations prove the applicability of the basic concept, that a diffraction pattern, which contains several Bragg peaks as well as the coherent scattering signal between them, can be inverted to reveal the individual scatterers in the crystalline sample.

2.1 Simulations on Pd Nano Crystals [GYWV11]

For these simulations [GYWV11] the experimental parameters similar to those used in the experiment [NSK+08] were considered (see Figure 2.1). The sample is located one meter upstream of the detector, which has a pixel size 200×200 μm^2 and consists of 1000 by 1000 pixels.

Pd nanocrystals of different sizes were used as samples in the simulations with a shape restricted by {111} side facets and (00±1) top and bottom facets (see Figure 2.1). The direction of the incident beam was taken along the (100) crystallographic direction. Diffraction patterns were simulated by the `MOLTRANS` code assuming kinematical scattering conditions. `MOLTRANS` calculates the scattering amplitude by coherently summing

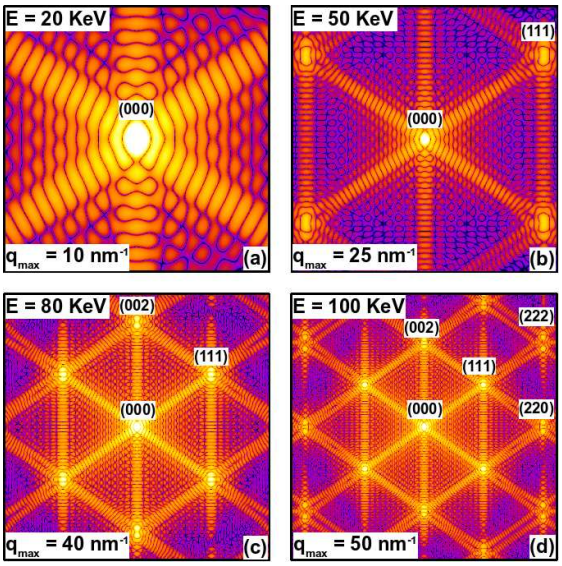

Figure 2.2: Diffraction patterns simulated for a 6 nm Pd nanocrystal for the different incoming photon energies, (a) 20 keV, (b) 50 keV, (c) 80 keV, and (d) 100 keV. All diffraction patterns are presented on a logarithmic scale.

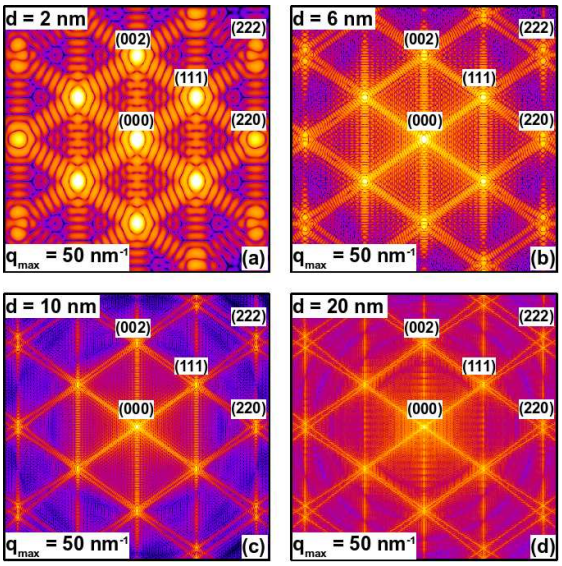

Figure 2.3: Diffraction patterns simulated for the incoming X-ray energy of 100 keV and different sizes of Pd nanocrystals, (a) 2 nm, (b) 6 nm, (c) 10 nm, and (d) 20 nm

up the spherical waves emitted by each individual scatterer. Throughout the simulation a fully coherent plane wave illumination was assumed.

First, diffraction patterns for scattering of X-rays from a 6 nm Pd nanocrystal at different incident energies from 20 keV to 100 keV were calculated in the simulations (see Figure 2.2) to prove the importance of the use of high energy X-rays. For photon energies below 50 keV in the experimental conditions Bragg peaks are not observed on the detector (see Figure 2.2(a)). However, when the incoming energy is becoming higher, an increasing number of Bragg peaks can be mapped simultaneously on the same detector (see Figures 2.2(b-d)). It is interesting to note that due to the curvature of the Ewald sphere some of the Bragg peaks at high $q-$values are split into two peaks (see 222 Bragg peak in Figure 2.2(d)).

Another important parameter in the simulations is the size of the Pd nanocrystals. Therefore, the lateral dimensions of the crystals were varied in a range from 2 nm to 20 nm, assuming the same photon energy of 100 keV (see Figure 2.3). It is clearly seen from these diffraction patterns that the positions of the Bragg peaks do not change, since the size of the unit cell is the same for both small and large crystallites. At the same time, the structure along the crystal truncation rods (CTR), that originate from the scattering from the facets of the nanocrystals [VR01b], is different, depending on the size of the particle. The fringe spacing P can be easily determined from $P = \lambda Z/d$, where λ is the wavelength, Z is the sample detector distance, and d is the size of the nanocrystal. It is evident that the fringe spacing in Figure 2.3 is smaller for larger particles. In order to perform a reconstruction from these diffraction patterns the sampling rate should be at least two pixels per fringe. This condition is not fulfilled for the largest crystal size. In the 10 nm case the fringes are sampled with about 3 pixels per fringe.

The diffraction patterns obtained from the simulations at 100 keV were used to reconstruct a projected electron density of the nanocrystals. The ER (50 iterations) and the HIO (100 iterations) algorithms were applied alternatingly to obtain real space images of the particles. The rectangular support (shown in Figure 2.4 (a,c)) was used as a constraint in the real space domain for all reconstructions presented in this chapter. The final results after 1500 iterations for particles of 2 nm and 10 nm in size are shown in Figure 2.4 (a,c). The shape and atomic structure of the nanocrystals is well-reproduced in these images. For comparison the initial model used in the simulations is shown in Figure 2.4 (b,d). It should be noted that the intensity in the middle of the reconstructed images is stronger, indicating a thicker part of the nanoparticle. Due to the chosen shape the projected electron density along the middle columns is higher. In fact, these results are similar to the images obtained in a high energy transmission electron microscopy.

To emphasise the importance of measuring several Bragg peaks simultaneously the reconstruction algorithm was also applied to a part of the diffraction pattern, obtained for the scattering of 100 keV radiation from the 10 nm Pd nanocrystal. It was assumed that only a smaller part of reciprocal space is measured (see Figures 2.5(a, c)), where only the masked part was used for the reconstruction. The white part was left to evolve freely throughout the reconstruction. It is well-seen from the results that, if only the central part of the diffraction pattern in forward direction is measured without Bragg peaks (Figure 2.5(a)), then a smooth distribution of electron density is obtained

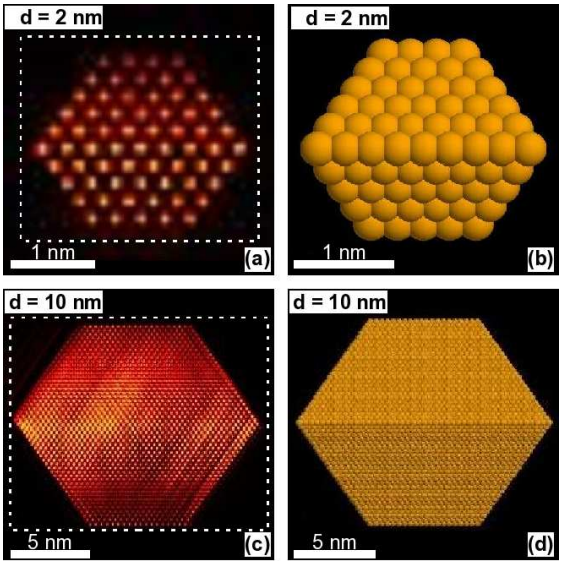

Figure 2.4: (a, c) Results of reconstruction of the projected electron density of Pd nanocrystals of 2 nm (a) and 10 nm (c) size from the simulated diffraction patterns shown in Figs. 2.3(a, c). The support used in the reconstruction is shown by the dashed line. (b, d) The initial model used in the simulations.

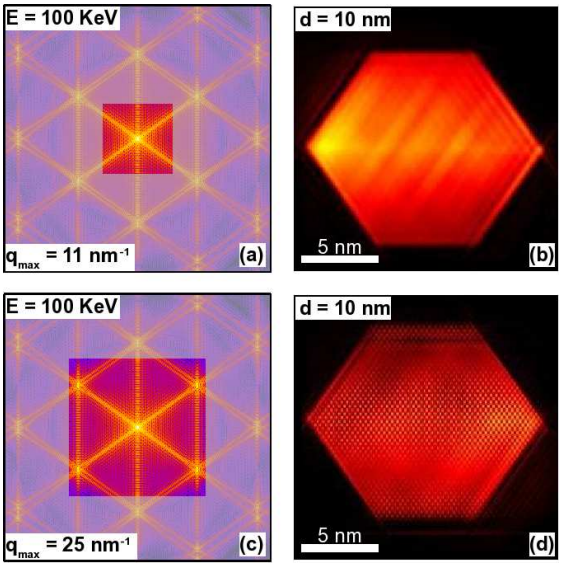

Figure 2.5: (a, c) Part of reciprocal space used for the reconstruction of electron density of Pd nanocrystal 10 nm in size (a) $q_{max} = 11$ nm^{-1}, (c) $q_{max} = 25$ nm^{-1}. (b, d) The reconstructed images obtained from the diffraction patterns (a, c) correspondingly.

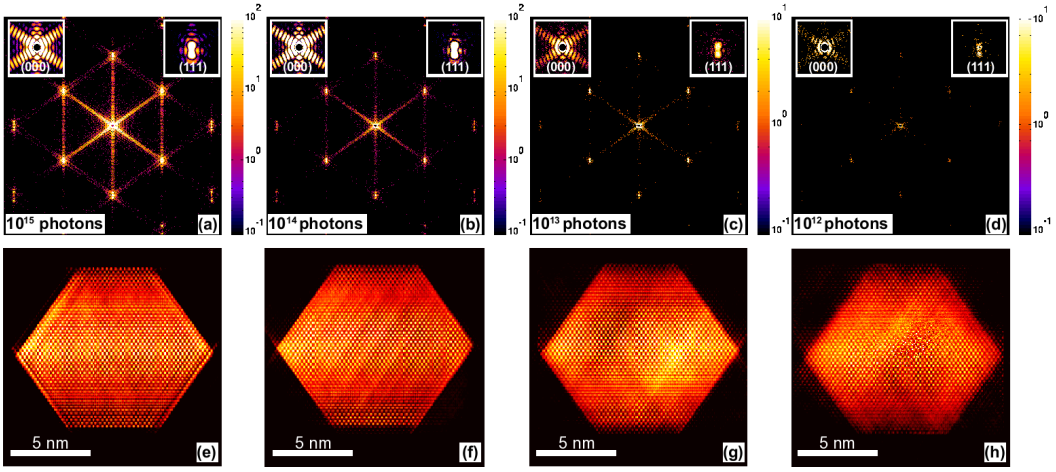

Figure 2.6: (a-d) Diffraction patterns calculated for different incoming photon flux focused to a spot of 100 nm and scattered from a 10 nm Pd nanocrystal. The insets on the left side show the scattering around $\mathbf{q} = 0$ and on the right side the enhanced scattering around the 111 Bragg peak. (e-h) Results of reconstructions from these diffraction patterns.

(Figure 2.5(b)), comparable to the result in [TNT$^+$09, TZN$^+$10]. The correct shape of the particle is reconstructed as well as a hint of the gradient representing the varying thickness of the sample. However, when the closest to $q = 0$ set of (111) Bragg peaks is included in the reconstruction (Figure 2.5(c)), it immediately results in a different image of the projected electron density, that reveals the regular crystal structure of the particle (Figure 2.5(d)) with atomic resolution. The small artifacts present in the reconstructions in Figures 2.4 and 2.5 can be attributed to the Ewald sphere curvature. Test simulations with a flat Ewald sphere have shown perfect reconstructions producing the same image as the input model. Experimentally, flat Ewald sphere conditions can be achieved by measuring a small tilt series of diffraction patterns. Another source of artifacts is the cut intensity at the edge of calculated diffraction patterns. These aliasing effects normally are not observed under experimental conditions, where the diffracted intensity is usually zero at the edge of the detector.

To simulate more realistic experimental conditions, the diffraction patterns were calculated with a finite incoming photon flux shown in Figure 2.6, assuming Poisson statistics. The incoming beam was assumed to be focused to a 100 nm spot in which the 10 nm crystal was positioned. Additionally, a 2×2 mm^2 beamstop was included in the simulations in the front of the detector, blocking the central part of the beam. In Figure 2.6, the diffraction patterns calculated for different incoming photon fluxes from 10^{15} down to 10^{12} photons in the focal spot are presented. The corresponding reconstruction of the projected electron density is also shown in the same figure. Down to a photon flux of 10^{13} photons the quality of the reconstruction is almost identical to the reconstruction obtained with infinite photon flux. Even for the lowest incoming flux of 10^{12} photons considered in these simulations, a reasonable reconstruction was obtained (see

Figure 2.6(h)). Approximately 200 photons scatter in this case in the position of the (111) Bragg peaks (see inset in Figure 2.6(d)), which is still enough to reveal the atomic planes in the reconstructed image (Figure 2.6 (h)). Since the signal along the CTRs is very low in this case, most information about the shape of the nanocrystal is lost. As a result, the edges of the nanocrystal obtained in the reconstruction are blurred. A tighter support would have been necessary to obtain better results in this specific case. A tight support could be obtained, for example, through the shrink-wrap algorithm. Another method to obtain the shape of the sample can be a reconstruction of the scattered intensities around an isolated Bragg peak, since around each Bragg peak the scattering amplitude contains all the information about the shape function of the crystalline part of the sample.

In summary, after performing realistic simulations, the possibility of imaging nanocrystaline materials at atomic resolution was demonstrated, using coherent hard X-rays up to the energy of 100 keV. With the start of operation of the new high-brilliance storage ring PETRA III [BBD$^+$04] and the upgrade of the ESRF as well as the APS this can be an exciting project for these facilities. This method can easily be extended for the three dimensional case, which is shown later in this thesis. First experiments have been performed with high energy X-rays on a sample containing a large amount of nanoparticles on the surface of a Si wafer[Gul08]. The experiment was performed at the ESRF at an X-ray energy of 90 KeV, measuring several Bragg peaks simultaneously in the far field on a single detector. However, the size and strain distribution in the illuminated area were the main limiting factors for the successful realisation of such a pilot experiment. In addition, the stability of the experiment in order to achieve atomic resolution is challenging. Another approach, which also enables measuring Bragg peaks at small angles, is using large unit cells. This is conveniently provided by nature in the form of colloidal crystals with a period in the range of a few hundred nanometers. The following chapter will present first results of the application of SAB CDI to colloidal crystals.

3 Experiments on Synchrotron Sources

This chapter will cover the experiments relevant to this thesis, which were carried out at synchrotron sources. The idea of SAB CDI, which was introduced in the previous chapter, has for the first time been applied experimentally. Obviously the advantages of synchrotron radiation in contrast to FEL radiation are the higher energies which are available. Future FEL sources will allow similar measurements, opening the route to ultrafast time resolved measurements. The idea to measure several Bragg peaks together with the coherent interference pattern between the Bragg peaks, relies on the use of high energy X-rays. The advantage of large crystal unit cells can be exploited by using colloidal crystals.

The first section will therefore describe colloidal crystals and their growth. Firstly it is explained what colloids are in general. Secondly some of the problems that can occur when growing colloidal crystals are addressed, especially the process during nucleation, where small grains of crystals are formed, from which the entire crystal grows.

The second section of this chapter describes an experiment where two different 2D projections of a thin colloidal crystal are measured. The positions of the individual scatterers are reconstructed, giving insight into the internal crystal structure. For one of the projections a defect in the form of a stacking fault is found and additional simulations confirm this result.

The third section extends this idea into the third dimension. By using the concept of tomography several projections of a colloidal crystal grain were measured in a rotational series. Combining the diffraction patterns the entire 3D reciprocal space of the crystal grain can be obtained. The simulations presented in that section show that such a data set can be used to reconstruct the entire crystal grain, revealing the internal structure. The simulation model also contained a stacking fault, which was reconstructed, assuming realistic experimental conditions.

One more application of CDI is presented in the last section of this chapter, which describes the application of coherent X-ray diffraction to nano wires. The diffraction signal of a single isolated nano wire is measured in the Bragg CDI geometry. By a detailed analysis of the scattering signal around a Bragg peak conclusions about the inner structure of the nano wire can be drawn. Again, 3D information was measured by rotating the sample and measuring diffraction patterns at each small incremental step.

After all, the high energies and the high degree of spatial coherence on synchroton sources available nowadays render it possible to measure several Bragg peaks from a nano structured sample together with the coherent scattering signal around and between the Bragg peaks. The analysis or even reconstruction of these diffraction patterns allow for an extraction of new knowledge about the internal structure of these materials.

3.1 Colloidal Crystals

High resolution 3D imaging of the internal structure of mesoscopic materials, such as colloidal crystals, by X-ray methods is a challenging problem [BSNS10, vSHP$^+$11]. The development of new approaches towards imaging, based on coherent X-ray scattering methods, are quite important for understanding the internal structure of such novel materials. Self-organized colloidal crystals can be used as the basis for new functional materials, such as photonic crystals, which may find applications in future solar cells, LEDs, lasers, or even as the basis for circuits in optical computing and communication. For these applications crystal quality as well as and monitoring the defect structure of these real colloidal crystals is essential [Say52, BCG$^+$00, SHE03, VAB$^+$00, YSM01, RMRC05, HAS$^+$09].

3.1.1 Colloids

A substance is classified as a colloid when it is microscopically dispersed evenly throughout a solution. The particles have to be significantly larger than the molecules of the solvent to be called colloids. This is important because otherwise the solvent could not be treated as a homogeneous, smooth background.

On the other hand, colloid particles must be small enough to comply the Brownian forces [Bro28]. The Brownian motion is a result of unbalanced momentum from collisions with solvent molecules at any given time . The resulting random motion was theoretically explained by Einstein [Ein05] and later proven experimentally by the Nobel laureate Jean Baptiste Perrin [Per09, Per14]. The two size conditions leave a range of about 1 nm to 1 μm in which a particle has to fall with at least one dimension to be defined as a colloid.

The fact that colloids perform Brownian motion enables them to redistribute their (kinetic) energy into thermal motion of the solvent molecules. This is important because through this interaction a colloidal system can reach a thermodynamical equilibrium. That is why colloidal systems exhibit an analogous phase behavior as atoms and molecules. For example, a dispersion of colloids with a hard sphere interaction potential can form a liquid phase, a crystalline phase, and even a glassy phase [PvM86]. In many ways colloids behave very similar to atoms or small molecules, only at a much slower time scale. This makes colloids an ideal model system to study atomic behaviour on a length and time scale, which is much more accessible. In some cases these model systems can indeed be observed at the single particle level and in real time, leading to the understanding of fundamental processes at the smallest scale [Poo04].

The hard sphere system is a simple model to describe a colloidal system. In this system the particles have an infinitely large repulsive potential for inter particle distances closer than their own diameter [Ons49]. Beyond that, interactions are absent. In the solid phase such systems form crystals, which were found to be promising candidates for the production of cheap photonic crystals [DSSS05].

Photonic crystals are nanostructured materials with periodic variations in the refractive index, due to which the motion of photons in a certain energy range is similarly affected as electrons in a semiconductor or X-rays in a crystal close to Bragg scattering

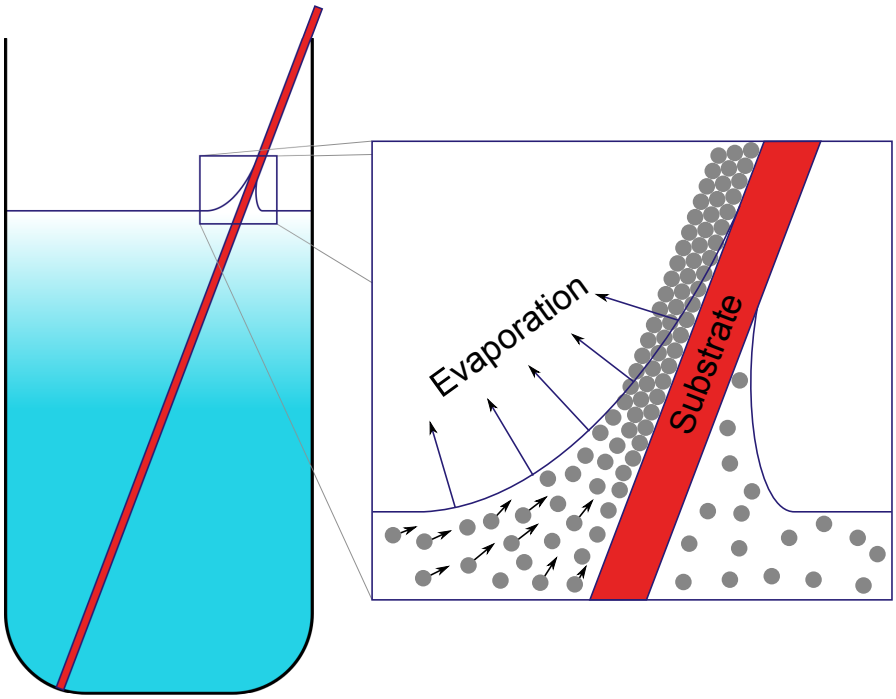

Figure 3.1: Colloidal crystals form when a saturated solution with colloidal particles slowly evaporates. The particles are pulled together by capillary forces, forming a close packed system.

conditions. Most importantly, photonic crystals inhabit a band gap structure. A naturally occurring photonic crystal is opal. Nano structured materials are promising for applications as low-loss optical fibers [Rus03, Kni03], low-threshold lasers [PLS+99], and even optical circuitry [SLJF03]. It should be noted here that none of the direct colloidal crystal structures that have been grown until now possess a full photonic band gap. The structure that shows the most promise is the FCC structure, but for a band gap to open up in this structure, the crystal voids have to be infiltrated with a high refractive index material and the colloidal particles have to be etched away [VJLL97, WV98]. However, the growth process of such colloidal crystals is rather complicated.

3.1.2 Nucleation and Growth of Colloidal Crystals

The ability of colloidal particles to self-assemble into a variety of crystalline phases lies at the heart of many materials-science studies, especially in the fields of photonics [HDVvB02]. Although colloidal photonic crystals can be grown quickly and cheaply, there are several hurdles to be taken to optimize the properties. Firstly, a method has to be found to reproducibly grow structures with robust, full band gap, since the uncontrolled formation of defects destroys most optical characteristics, for instance, by broadening and doubling of Bragg peaks. Secondly, control over the inclusion of defects

has to be obtained to reduce unwanted disorder and add functionality where it is required [Hil12]. The controlled incorporation of defects may be useful, for instance, by creating localized defects.

Colloidal crystals form when a saturated solution with colloidal particles slowly evaporates (see Figure 3.1). Only the molecules from the solution evaporate, leaving the colloidal particles behind, which are pulled together by capillary forces. Since the particles can find a thermodynamic equilibrium state, they try to fill the least space. If a crystallization nucleus is found the particles can arrange into regular lattices. This method is called convective assembly technique [JBHC99, VBSN01, NAM+04]. Another commonly used growth technique is sedimentation, where the colloidal particles slowly settle at the bottom of the solution. Colloidal crystal growth through sedimentation is mainly applied to smaller particle sizes (<400 nm).

Considerable research has been devoted to the creation of such materials, but much less work focuses on the occurrence of defects. Recent literature discusses the influence of stacking faults, the most common type of defect in hard-sphere-like colloidal crystals, on the photonic properties of colloidal inverse-opal materials [VAB+00, YSM01]. Crystallisation always happens around a nucleation point. Crystal nucleation is a well-studied phenomenon, yet the rate at which it occurs remains difficult to predict. Classical nucleation theory makes the assumption that the (pre-) critical nuclei are effectively spherical and have the same structure as the stable crystal bulk phase that is nucleating. Homogeneous nucleation occurs when small crystalline regions form from structural fluctuations in a supersaturated solution. The growth of these regions depends on the decrease in bulk energy, which favors growth, and the increase in surface energy, which favors shrinkage. Small crystals form continually from the fluctuations but then typically re-dissolve because of the high surface energy. Crystal growth however becomes energetically favorable when the size r of the crystallites exceeds a critical value. The competition between surface energy and bulk energy is reflected in the free energy for a spherical crystallite

$$\Delta G = 4\pi r^2 \gamma_f - \frac{4\pi}{3} r^3 \Delta\mu n, \tag{3.1}$$

where r is the radius of the nuclei, γ_f is the free energy of the crystal-liquid interface per unit area, $\Delta\mu$ is the difference between the liquid and the solid chemical potentials, and n is the number density of particles in the crystallite [KG10]. The size of the critical nucleus is

$$r_c = \frac{2\gamma_f}{\Delta\mu n}, \tag{3.2}$$

corresponding to the maximum of ΔG. These observations are not limited to colloidal crystals, they are rather general. There is little knowledge about these early states of crystallisation, primarily because of the difficulty of directly observing the nuclei in real space. Therefore, the observations done on colloidal model systems [GWS+01] give an important insight into the physics of nucleation and crystallisation.

The growth process after the nucleation strongly depends on the properties of the nucleus. Hence, it is of utmost importance to understand the structure of the nucleus.

The process of crystal nucleation and growth can be investigated through simulations [AF01] or direct measurements [GWS+01]. Both methods however come to the same conclusion, namely that already in this early phase a combination of FCC and HCP stacking occurs. The free volume for ordered spheres with a maximum packing volume fraction of 74 % is greater than that of disordered spheres, where the maximum packing is only around 64% and, according to this, the entropy is lower in the crystalline state. In fact, the FCC - HCP free-energy difference is so tiny that small hard-sphere crystals will always contain an equilibrium concentration of stacking faults. The FCC crystal is the most stable structure, but the difference is so small that stacking faults can easily occur. This situation is different from ordinary atomic crystals, which choose for one of the two close packed crystal structure with a small density of stacking faults. This mixture of FCC and HCP stacking is commonly referred to as RHCP (see section 1.3.1). There is a finite number of stacking faults, but the overall stacking parameter has a large tendency towards FCC [HDVvB02]. It is usually assumed that the origin of the RHCP stacking is purely kinetic. Although this may be correct for larger crystals, in the early stages of nucleation and for small crystallites the RHCP structure is simply more stable than FCC [AF01]. Since the growth process of the crystal depends on the structure of the nucleation grain the stacking faults have to be well characterized. It is also desirable to visualize the positions of each colloidal particle in the grain to understand the nucleation and growth process. The following sections present experiments which show the potential of SAB CDI as a tool to retrieve the desired information.

3.2 Coherent X-ray Imaging of Defects in Colloidal Crystals [GYM+10]

Real crystalline materials, in contrast to an idealized picture of perfect crystals, contain a broad spectrum of defects. These defects determine most of the mechanical, optical, and electronic properties of the crystals [AM76]. Different methods are used to reveal these defects and their distribution in the material, either directly, or indirectly. X-rays are a very attractive probe due to their high penetration depth and are used routinely for investigating defects in different materials. For example, X-ray topography [Aut01] was one of the first X-ray imaging methods to visualize defects in crystals. Using this approach, defects are imaged indirectly by the induced strain fields. Presently, well-developed tomographic methods can reliably reveal the three-dimensional (3D) distribution of defects in materials [Ban08], but the resolution is typically limited to a few microns. Unfortunately, most of the present X-ray methods fail to visualize the defect core down to the atomic level in a bulk material. Here it is proposed to use CXDI to map such defects in colloidal crystals.

3.2.1 Experiment at ID06 at ESRF

In this coherent imaging experiment a thin film of a colloidal crystalline sample on a glass substrate was used. It was grown by the convective assembly technique [JBHC99,

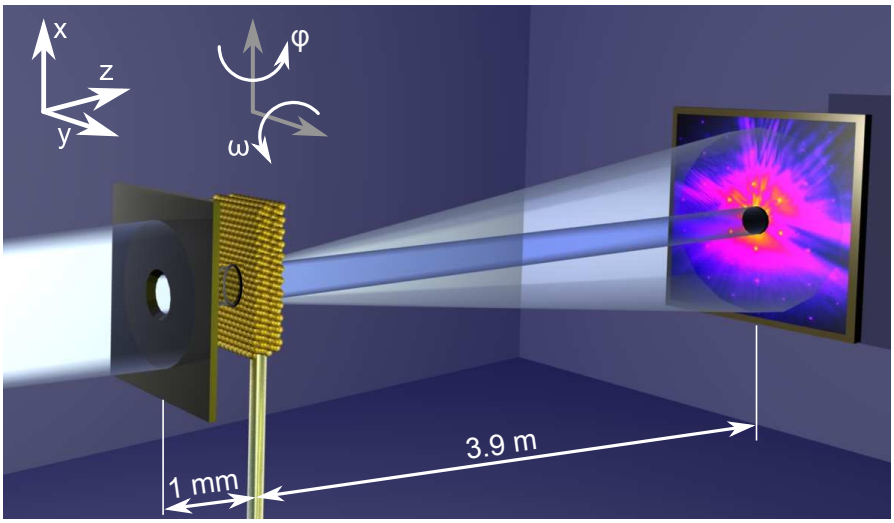

Figure 3.2: Schematic view of the experiment, showing the pinhole close to the sample and the detector.

BCG+00] using polystyrene microspheres with a diameter of 425 nm and a relative standard deviation in the diameter of less than $< 5\%$. The spheres were synthesized by emulsifier-free emulsion polymerization of styrene, using potassium persulphate as an initiator [GHHO74]. Glass microslides were immersed in an aqueous suspension of microspheres with a volume fraction of about 0.5%. The temperature of the film growth was 50°C. The grown crystalline films have a FCC structure [HAS+09] and are typically 20 to 30 layers thick. Figure 3.3(e) shows an SEM image of the surface of a colloidal crystal, grown with the described method.

The experiment was performed at the microoptics test bench at ID06 beamline of the ESRF with an incident X-ray energy of 14 keV. The geometry of the experiment (see Figure 3.2) allows rotation of the sample around the vertical axis perpendicular to the incident X-ray direction. The pinhole was positioned in front of the sample to create a finite illumination area. Several pinholes were installed and pre-characterized by measuring the diffraction pattern from the pinhole itself. The apertures were produced by laser drilling in a 250 μm thick Pt foil. The final shape has a tapered profile with a minimum thickness of 7 μm. Due to the roughness of the edges in the aperture (see Figure 3.3(a,b)) the pinholes were etched by a focused ion beam (FIB)[1] to clean the edges. Clearly the pinholes much more resemble a circular aperture after the cleaning process (see Figure 3.3(c,d)). After the characterization through the investigation of the diffraction patterns a 6.9 μm pinhole was chosen and positioned as close as possible in front of the colloidal crystal.

For the measurements with the sample the initial orientation of the sample (with azimuthal angle $\varphi = 0°$) corresponds to the direction of the incident X-rays along the

[1]The etching was performed by Daniel Stickler from the group of Prof. Oepen at the University of Hamburg.

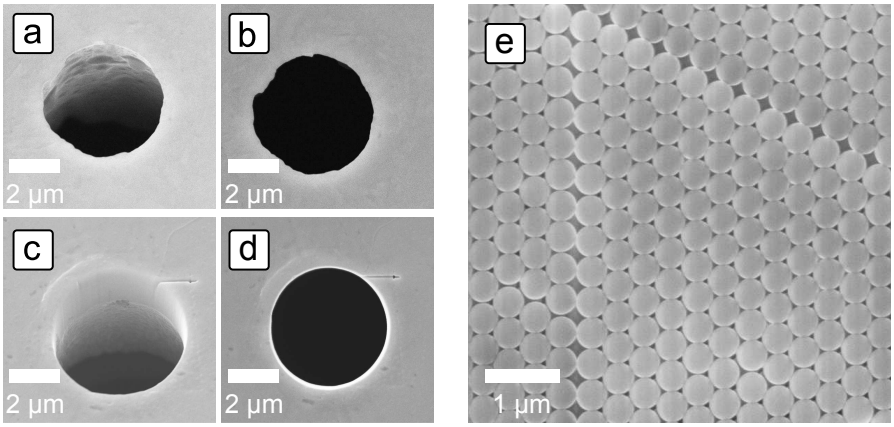

Figure 3.3: SEM Images, (a,b) show the pinhole after the laser drilling, from two different view angles, (c,d) show the aperture after the FIB cleaning process. (e) is an SEM image of the surface of a colloidal crystal grown under the same conditions as the used sample.

[111] direction of FCC colloidal crystal and was perpendicular to the surface normal of the sample (see Figure 3.2). The pinhole to sample distance was <1 mm. The sample was scanned in the x, y - directions perpendicular to the incident beam with the possibility to locally map different positions of the sample. Depending on the position of the sample the diffraction pattern changed. In the disordered regions of the sample only Debye-Scherrer rings were measured similar to powder diffraction. In other parts of the sample very clear Bragg peaks were seen in the diffraction pattern, indicating an ordered part of the sample. Sometimes the Bragg peaks were twinned, which led to the conclusion that two grains with different orientation were illuminated, giving rise to two sets of Bragg peaks.

The diffraction data were recorded using a Photonic Science 12 bit Charge - Coupled Device (CCD) with 4005×2671 pixels, each 9×9 μm^2 in size. An evacuated tube was positioned between the sample and the detector to reduce air scattering. The detector was placed at a distance 3.9 m behind the sample with a corresponding resolution of Δq=0.16 μm^{-1} per pixel. Due to saturation of the detector by the high intensities at the position of the Bragg peaks, short (10 s) and long (30 s) time exposures were used and each were repeated 10 times to enhance the signal to noise ratio. These images were carefully superimposed for the phase retrieval. The dark field background was subtracted from all diffraction patterns. Typical diffraction patterns are displayed in Figure 3.5, showing the strong oscillations of the Airy pattern due to the round aperture. On top of the diffraction pattern from the pinhole several orders of Bragg peaks could be observed. Depending on the rotation of the sample different kinds of streaks were seen. In the center of each diffraction pattern the beamstop blocked the intense direct beam.

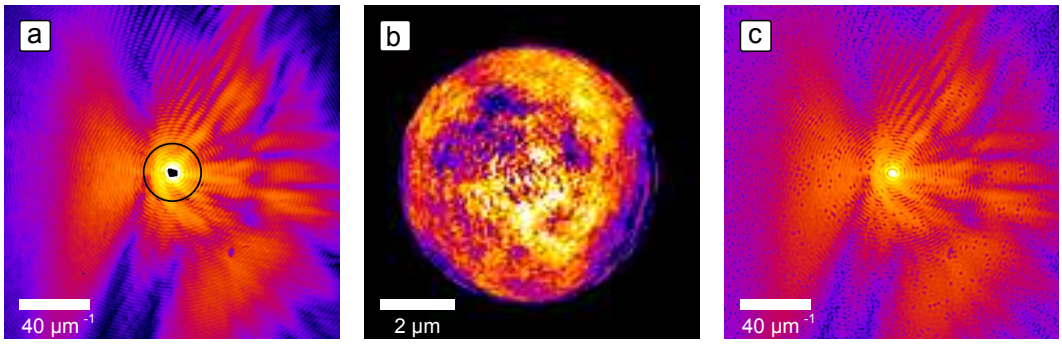

Figure 3.4: Results of the measurement of the pinhole alone. (a) shows the measured diffraction pattern, (b) the resulting reconstruction, and (c) the reconstructed reciprocal space.

3.2.2 Results and Discussion

Pinhole characterization

Prior to the measurements with the sample the pinholes had to be characterized. The diffraction pattern from the pinhole without the sample is shown in Figure 3.4(a). This diffraction pattern is a combination of data measured with a large beamstop, indicated by the black circle, and several diffraction patterns measured with a small beamstop, moved transversely to different positions close to the center of the diffraction pattern. Measurements with the large beamstop enable long exposure times, resulting in a diffraction pattern with high statistics. All these measurements were scaled according to the exposure times and then superimposed on each other. The result is shown in Figure 3.4(a). Strong fringes typical of an Airy pattern [BW00] from a circular aperture are clearly seen in this diffraction pattern. Due to the high quality of the pinhole many diffraction orders can be identified in this diffraction pattern. The resolution in reciprocal space is sufficient to resolve the fringes about 7 pixels per fringe for the 6.9 μm pinhole. Despite cleaning the aperture with a FIB an unavoidable diffuse background due to imperfections contaminates the diffraction data, which is much stronger for uncleaned pinholes. Figure 3.4 shows the best results from the measured pinholes.

Due to the high sampling rate, the small amount of missing data, and the big number of measured fringes several attempts to reconstruct the wavefront after the pinhole were performed. Unfortunately, all of them were inconclusive, Figure 3.4(b) shows the real space result of the best reconstruction. It can be seen that the wavefront after the aperture seems to inhabit many disturbances. However, all of them were artifacts that were not reproduced, when the reconstruction process was seeded with a different set of random phases. It can be seen more clearly in the reconstructed reciprocal space, which is shown in Figure 3.4(c). Here, the reconstructed amplitudes are shown before the reciprocal space constraint is applied, therefore the shown amplitudes correspond directly to the shown real space reconstruction. The large amount of vortices in the

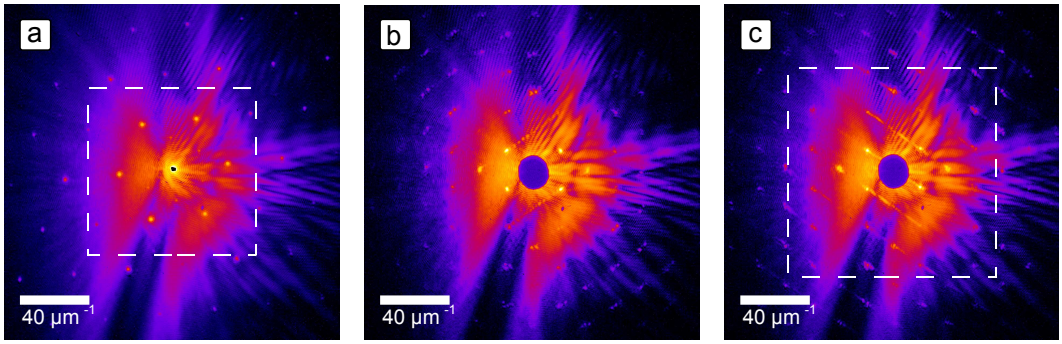

Figure 3.5: Measured diffraction patterns, (a) for the sample rotation of $\varphi = 0°$, (b) and (c) for $\varphi = 35°$. The difference between (b) and (c) is a slight tilt in ω by one degree. The white squares correspond to the area used for the reconstructions.

reconstructed diffraction pattern verifies the conclusion that the reconstruction inhibits artifacts. Due to the simple nature of the shape of the object the shrink-wrap algorithm was comparably successful and a very good round support was reconstructed even when starting from a bigger square support.

The reconstruction shown in Figure 3.4(c) was obtained by combining the ER and the HIO algorithms. After 600 iterations of HIO 50 iterations of ER were used to push the algorithm towards a solution. This scheme was repeated 7 times and eventually another 150 iterations of the ER algorithm were used to clean up the reconstruction, resulting in a total of 4700 iterations. The reconstruction was performed with a very tight support, which was deduced from the fringe spacing. One issue with this measured dataset is the relatively bad contrast of the fringes, which can occur due to a small degree of coherence of the beamline, or due to the fact that the pinhole was not completely opaque on the edges. The latter is the more probable conclusion. At an X-ray energy of 14 keV the 7 μm of Pt only absorbs ≈93% of the radiation.

Measurements at azimuthal angle $\varphi = 0°$

Positioning the sample just after the aperture yields a similar set of fringes as in the previous case. In addition, due to the long range order in the colloidal crystal several orders of Bragg peaks are easily visible in the diffraction patterns (see Figure 3.5). The strongest is the hexagonal set of 220 Bragg peaks typical of scattering from a FCC structure. Figure 3.6(a) shows a part of the diffraction pattern where all six 220 Bragg peaks are easily visible. The shown region is indicated in Figure 3.5(a,c), as a white square. Each of the Bragg peaks contains a few orders of diffraction fringes similar to those at $q = 0$, due to the finite aperture in front of the sample, as it was explained in section 1.3.2. In addition to the allowed 220 Bragg peaks much weaker forbidden peaks were observed. These were identified to be $\frac{1}{3}$ 224 peaks. They are also seen in Figure 3.6(a). The appearance of forbidden peaks is an indication of defects in the crystal. Such peaks could also be attributed to scattering from X-rays with higher energies, e.g.

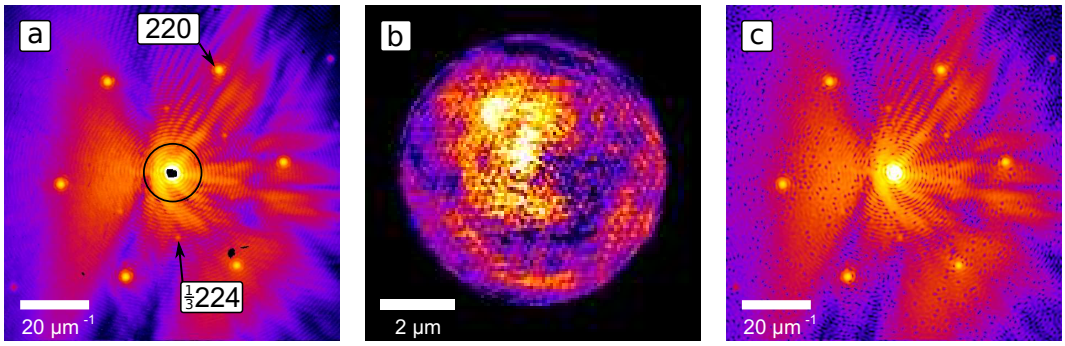

Figure 3.6: Results of the measurement of the pinhole together with the sample. (a) the measured diffraction pattern, (b) the best reconstruction in real space, and (c) the reconstructed reciprocal space.

the third harmonics from the undulator, however, the simulations later showed similar peaks as a result from defects.

The measured diffraction data were inverted by applying the GHIO algorithm [CMWL07]. Starting with eight parallel runs with random initial phases, five generations were used, with 1000 iterations of HIO [Fie82] and one iteration of the ER algorithm at the end of each generation. In all reconstructions the positivity constraint was enforced.

The first attempts to reconstruct the sample from the measured diffraction pattern shown in Figure 3.6(a) have identified that the actual signal from the colloidal sample was strongly suppressed by the high level of the varying background. Again the diffraction pattern shown is the result of the combination of several measurements in order to minimize the missing data. Figure 3.6(b) shows the result of the reconstruction. Similar artifacts as in the reconstruction of the pinhole data can be observed. In addition, a regular structure can be observed on the varying background. However, the reconstructed reciprocal space (see in Figure 3.6(c)) clearly shows a similar vortex structure as obtained in the reconstructions of the pinholes. Together with the fact that reconstructions with different random starting phases did not provide consistent results this leads to the conclusion that further treatment of the data has to be done.

The failed reconstructions were attributed to the strong smooth incoherent background originating from the pinhole. To improve the quality of the reconstruction a scaled diffraction pattern of the pinhole (Figure 3.4(a)) was subtracted from the diffraction pattern of the sample (Figure 3.6(d)). A scaling factor of 1.3 was found to be efficient to remove artifacts from the reconstructed images. The 220 Bragg peaks, and especially the fringes around them, were well distinguished on a reduced background (see Figure 3.7(a)). Negative values, shown as black regions in the difference diffraction pattern in Figure 3.7(a), were left to evolve freely in the reconstruction procedure. Reconstructions performed from these data sets were not stable due to the large amount of missing data, especially in the low q region [TEJ$^+$06]. To stabilize the reconstruction process the central region (with $q < 5.44\ \mu\text{m}^{-1}$) of the reconstructed diffraction pattern was fixed

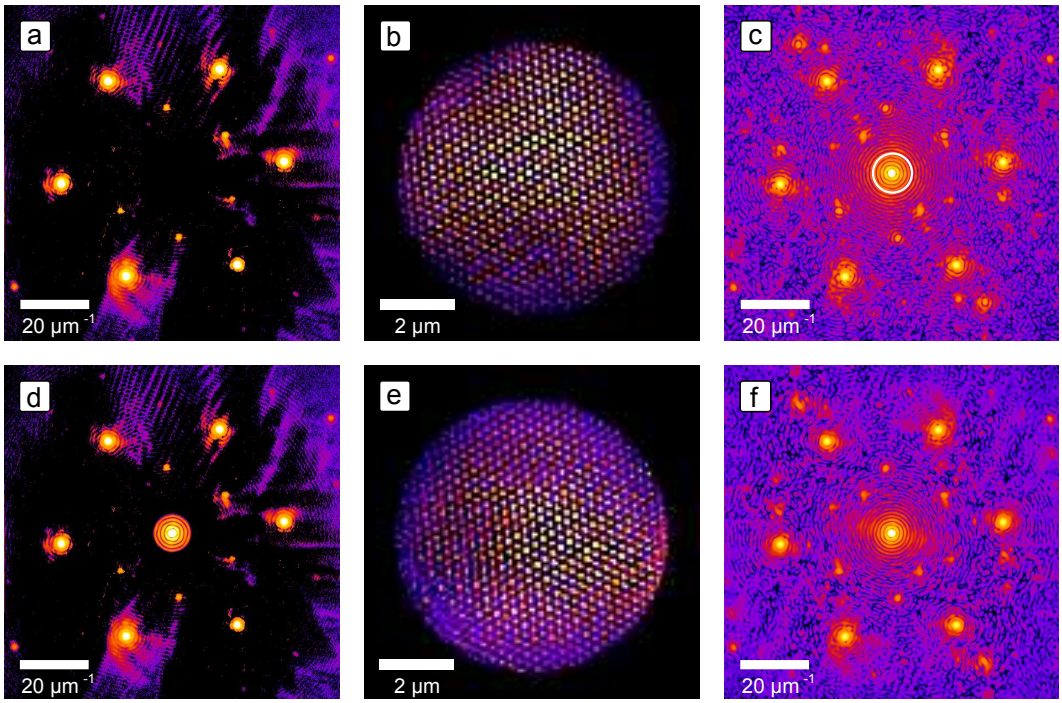

Figure 3.7: (a) Diffraction pattern after the subtraction of the scaled pinhole diffraction pattern. (b) Reconstructed real space image after 20 iterations and (c) corresponding reciprocal space reconstruction. (d) The diffraction pattern used for the final result, where the center was filled from (c). (e) the final result of the reconstruction after 5000 iterations and (c) the corresponding reciprocal space reconstruction.

after 20 initial iterations (see marked region in Figure 3.7(c) and center in Figure 3.7(d)). Proceeding with these fixed low q values resulted in stable reconstructions. The results became very reproducible, almost independent from the reconstruction procedure used. Figure 3.7(e) shows the final result of the reconstruction after 5000 iterations. This image represents a *projection* of the 'atomic' structure of the colloidal crystal along the [111] direction. The hexagonal structure is clear across the whole illuminated region with only slightly lower intensity values of the image around the edges of the pinhole aperture. Due to projection imaging, the periodicity does not correspond to the colloidal interparticle distance d in a single crystalline layer. In this projection all three possible positions (A, B and C) of a hexagonal layer in a FCC crystal contribute to the signal, resulting in a reduced periodicity of $d/\sqrt{3}$.

The major differences from the results of previous work with CXDI on crystalline samples [PWV$^+$06] are clearly demonstrated in Figure 3.7(e). Instead of a continuous shape and strain field, reconstructed from the measurements of diffraction patterns around a single Bragg peak, the hexagonal structure reconstructed in Figure 3.7(e) provides the projected positions of the colloidal particles. This can be easily understood by the arguments given in chapter 2. It becomes clear that the form-factor $F(\mathbf{G_n})$ of the colloidal

sphere is sampled by only a few points in reciprocal space and modulates the values of the Bragg peaks [HAS+09]. In this specific case the area of reciprocal space for reconstruction was limited by including only the strongest 220 Bragg peaks which have a similar intensity [2]. The form-factor $F(\mathbf{G}_{220})$ (see equation (1.30)) at the position of the 220 Bragg peaks can be taken out of the sum in the scattering amplitude giving

$$A(\mathbf{q}) = F(\mathbf{G}_{220}) \sum_n S(\mathbf{q} - \mathbf{G_n}). \tag{3.3}$$

The inversion of this expression can provide the 2D projection of the positions of the colloidal particles and the shape function of the illuminated region $s(\mathbf{r})$ encoded in the Bragg peak positions $\mathbf{G_n}$ and in the function $S(\mathbf{q})$, as was explained in section 1.3.3. However, information about the shape of individual colloidal particles (encoded in the form-factor $F(\mathbf{G_n})$) can not be retrieved. Following this analysis the finite size of the particles in the reconstruction can be attributed to a finite resolution and not to the reconstruction of the colloidal particle shape function. The smearing of individual particle positions can be attributed to a small shift in the positions of the colloidal particles in the projected lattice (there are about 20-30 layers in the z direction). A line scan through the reconstructed image in Figure 3.7(e) gives a resolution of about 95 nm, obtained as an average full width half-maximum (FWHM) of the colloidal particles' positions.

Measurements at azimuthal angle $\varphi = 35°$

Following these first measurements the sample was rotated around the vertical axis by about 35°. Rotating the sample around the x-axis allows the measurement of different sets of diffraction planes. The direction of the incident X-rays along the [110] direction of the colloidal sample lattice at $\varphi = 35°$ is of particular importance. At this position the set of (111) planes is aligned along the incident beam. The experimental setup was adjusted (see Figure 3.8). In this geometry the pinhole sample distance was increased to 25 mm due to geometrical constraints.

Diffraction patterns measured at an angle of $\varphi = 35°$ (see Figure 3.5(b,d)) were especially intriguing. They show strong streaks with varying intensity originating at the Bragg peaks with an angle of $-55°$ (Figure 3.5(b)) and $+55°$ (Figure 3.5(c)) to the horizontal direction depending on the specific location on the sample. The direction of the streaks depended on the rotation of the sample around the horizontal axis. A variation of a few tenth of a degree in ω were enough to completely change the diffraction pattern. It is well known from previous studies [HAS+09] of similar colloidal systems that such streaks in reciprocal space are induced by stacking faults in the FCC structure in (111) planes. The diffraction patterns were reconstructed as described before. The final result of this reconstruction (from the data shown in Figure 3.9(a)) is presented in Figure 3.9(b). The regular crystal structure of the colloidal crystal sample is very well reconstructed. In addition, a stacking fault (indicated by arrows in Figure 3.9(b))

[2] The small contribution of the forbidden 1/3[224] reflections can be neglected here.

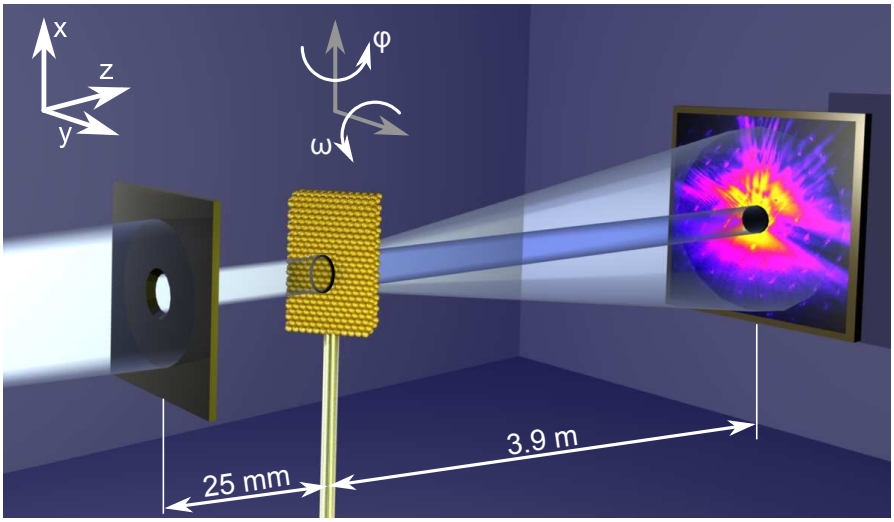

Figure 3.8: Schematic view of the experiment, showing the rotated sample, now located slightly further downstream from the aperture.

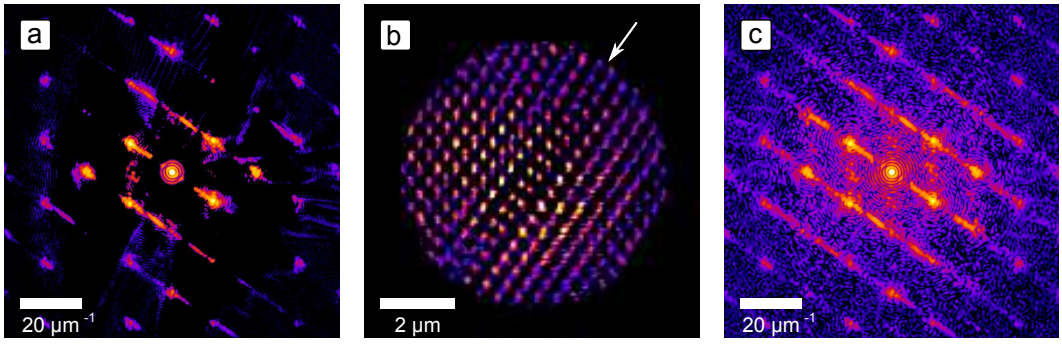

Figure 3.9: Results of the reconstruction from the measurements at $\varphi = 35°$. (a) Result after the subtraction of the scaled pinhole diffraction pattern from the measured data. (b) Reconstructed real space image after 5000 iterations and (c) the corresponding reciprocal space.

appears as a break in the 'correct' **ABC** order [War90]. Colloid self-assembled crystals are known to be prone to stacking disorder. Often a RHCP structure is observed [PvMB$^+$89, LA94, Ver95, ART$^+$00, SFK$^+$06, DPA$^+$05], which consists of a random mixture of FCC and HCP planes as explained earlier in sections 1.3.1 and 3.1.2. The reconstructed image in Figure 3.9(b) shows a very distinct situation. A stacking fault inbetween and two FCC domains with the same stacking direction can be seen. The effect of the stacking fault in this case is two FCC crystals sliding relative to each other. This sliding can be seen in Figure 3.9(b) as a 'break' of the lines of bright spots at the defect. It was recently suggested on the basis of X-ray diffraction over large (submillimeter) sample area that these double stacking defects consisting of two HCP planes, are a common imperfection in convectively assembled colloidal crystals [NSG$^+$09].

Simulations

To support the results of the reconstructions simulations were performed on a FCC structure. As a model a sphere filled with point scatterers ordered in a FCC lattice (see Figure 3.10(a)) was used. The spherical shape represents the round part of the colloidal sample defined by the pinhole. Using a sphere instead of a cylindrical shape suppresses edge artifacts in the calculations. All other parameters of the simulation have been chosen to scale according to the experimental conditions. The simulated diffraction patterns resulting from this structure (see Figure 3.10(b)) have the same significant features as the measured data (compare with Figure 3.6(a)). When rotating the model by 35 degrees the HCP planes are clearly visible (see Figure 3.10(c)) and the resulting diffraction pattern shows the corresponding Bragg peaks (Figure 3.10(d)). A classical stacking fault [War90] as a defect in the model structure was introduced (see Figure 3.10(e)). The simulated diffraction pattern (Figure 3.10(f)) shows the corresponding streaks, but in this case every third streak is missing in reciprocal space, which was not supported by the measurements (see Figure 3.5(b,c)). Since the real space reconstruction from the experimental data shows an additional narrowing of the two layers (see Figure 3.9(b)) the distance between the two adjacent planes surrounding the stacking fault was changed to 2/3 of the nominal (111) distance in the model simulations (Figure 3.10(g)). The resulting diffraction pattern (Figure 3.10(h)), calculated corresponding to the azimuthal angle $\varphi = 35°$ in the experimental conditions, concords very well with the measurements (compare Figure 3.5(c) and 3.10(h)).

For the simulations presented here point scatterers were used in the model. A colloidal crystal however consists of particles with a finite size. The resulting form factor was not taken into account, since the modulations of the diffraction signal, due to a form factor, were not observed in the measurement. To perform simulations closer to realistic experimental conditions, where the positions of each individual scatterer vary slightly from the ideal crystal lattice, a random shift in the positions of the point scatterers was introduced. This results in diffraction patterns with less contrast, as shown in Figure 3.11(a,c), similar to the measurements. These simulated diffraction patterns inhibit characteristics similar to a form factor. The inversion of these diffraction patterns (Figure 3.11(b,d)) resulted in strong resemblance to the reconstruction results of the

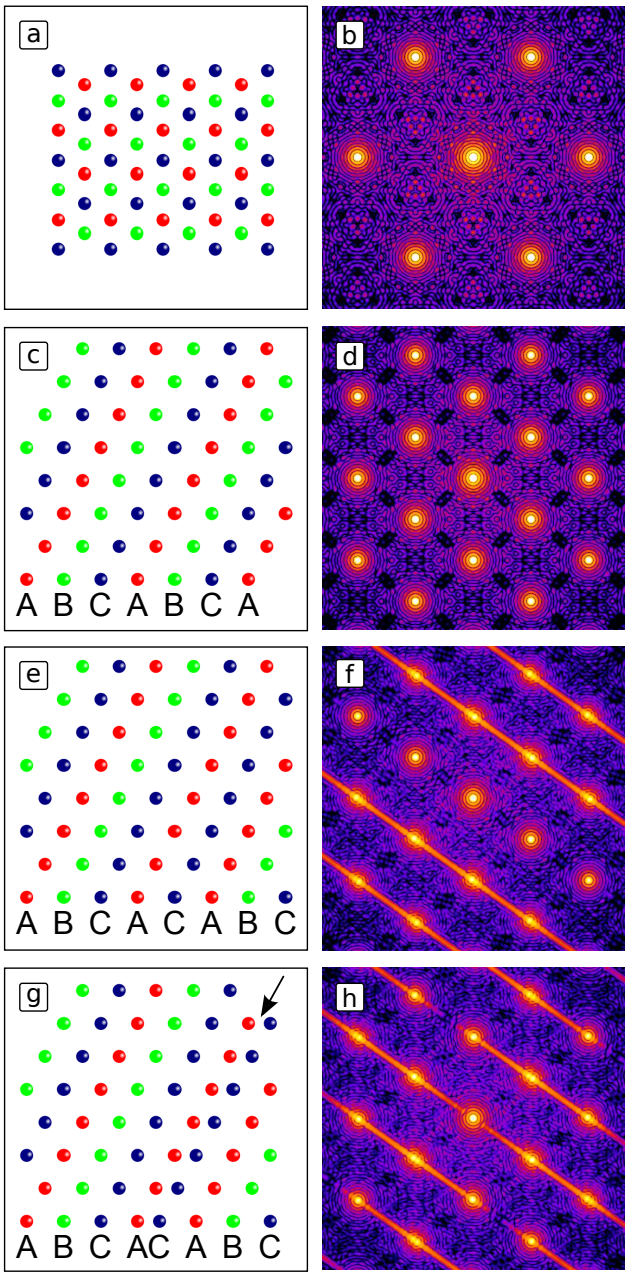

Figure 3.10: Model simulations, showing the model in the left column, and the corresponding diffraction pattern in the right column. The four different cases are (a,b) a FCC crystal along the [111] direction, (c,d) the same crystal along the [110] direction, (e,f) the same view as before, but now the crystal has a stacking fault, and (g,h) the two planes surrounding the stacking fault have a reduced distance to each other.

experimental data. In particular, the two planes with the reduced distance between them are very well visible.

In Figure 3.3(e) the SEM image of the crystal surface of a similar colloidal crystal was shown. The morphologies of the SEM image, the reconstructed image in Figure 3.9(b), and the model simulations correspond well, indicating that the reconstruction is indeed a 2D projection of a stacking fault measured along the [110] direction. It should be noted here that the SEM image only provides information about the top layer of the crystal, while the CXDI image is a projection of the 3D crystal structure. This demonstrates the high sensitivity of the proposed CXDI technique with the possibility of mapping the core of the defect structures in convectively assembled colloidal crystals. For example, coherent imaging can reveal small effects such as the presence of displacements between layers containing a stacking fault. Therefore, through a combination of CXDI with tomographic methods the full 3D structure of the crystal can be reconstructed, which will be demonstrated in the next section.

3.3 Three-Dimensional Structure of a Single Colloidal Crystal Grain Studied by Coherent X-ray Diffraction [GYM+12]

Measuring diffraction patterns from a coherently illuminated, finite-sized crystalline sample locally around a selected Bragg peak gives information about the shape and a uniform distribution of strain in this particle, as discussed in section 1.4. This method was extended to image a finite region of a two-dimensional (2D) colloidal crystal (see previous section). In this proof-of-principle experiment it was demonstrated that an inversion of the coherent diffraction pattern containing several Bragg peaks reveals the projection of the position of individual scatterers (colloidal spheres in this case) as well as the core structure of the defects in the sample. In this section these findings are extended to a single 3D grain of a colloidal crystal illuminated by coherent X-rays. First results of the experimental realization of Sayre's original idea of collecting 3D crystallographic data and measuring the scattered intensity not only at the Bragg peaks but also in the regions between the Bragg peaks are presented. Reconstruction of that data can provide 3D information about the actual positions of the scatterers in the colloidal crystals, including possible structural defects, which will be shown in simulations.

3.3.1 Experiment at P10 at PETRA III

The coherent X-ray scattering experiment was performed at the Coherence Beamline [3] P10 of the PETRA III facility at DESY in Hamburg during commissioning time. The incident energy of the X-rays was chosen to be 7.9 keV in order to have a high penetration depth through the colloidal crystal under investigation and to map several Bragg peaks onto a single 2D detector.

[3] http://hasylab.desy.de/facilities/petra_iii/beamlines/p10_coherence_applications/index_eng.html (status 2012)

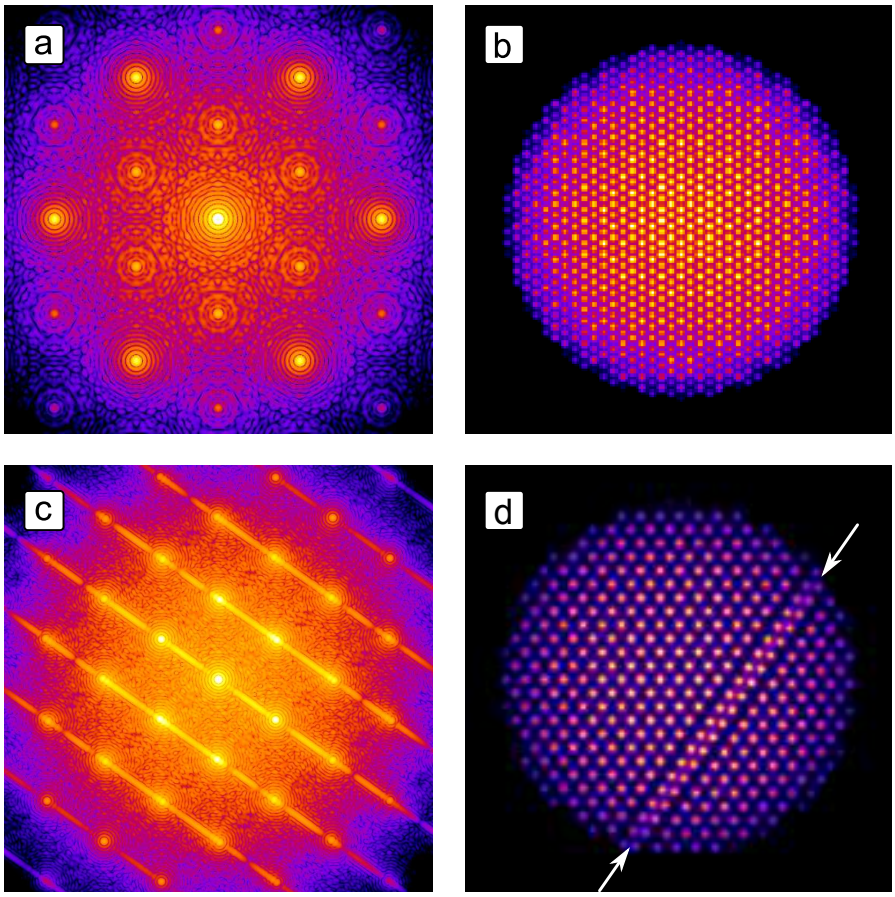

Figure 3.11: Results of the simulation. (a),(c) The diffraction patterns of the model with a stacking fault and a small random shift in the positions of the scatterers. (b),(d) The inversion of the diffraction patterns show similar features as the reconstructions from the measurements.

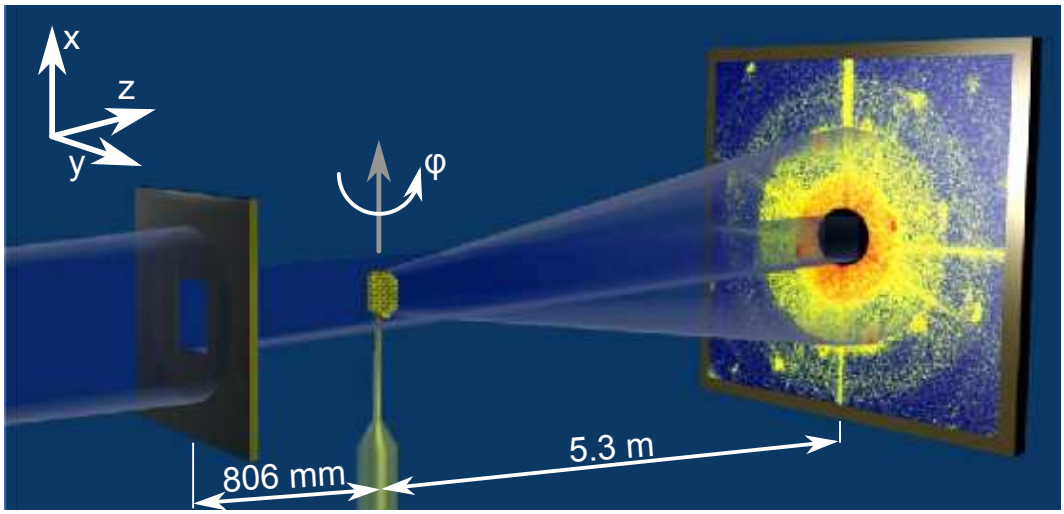

Figure 3.12: Schematic view of the CXDI experiment, showing the beam defining slits, the colloidal sample, and the detector.

Silica microspheres were synthesized and coated with 1-octadecanol to provide steric stabilization as described in [VvB94]. The particle diameter of about 230 nm was determined by small-angle X-ray scattering in a dilute suspension, using the separation between the form-factor minima [PDAV04] and for the sedimentary colloidal crystals from the position of the Bragg peaks [PAD$^+$02]. The particle size polydispersity of 4.1% was determined by transmission electron microscopy. To grow colloidal crystals the microspheres were dispersed in cyclohexane, placed in a vial, and kept vertically for sedimentation and self-organization. The solvent slowly evaporated on the time scale of several months. The top layer of the dry sediment (of about 5 mm thickness) showed characteristic optical Bragg reflections under white light illumination. A piece of this dry sediment was mechanically crushed to yield a powder of small grains. Individual grains of such colloidal crystals were picked up manually, using a micromanipulator (PatchMan NP2). They were attached by an adhesive to the tip of a 10 μm diameter carbon fiber, which was mounted on the sample holder. Afterwards they were characterized, using an optical microscope (Leica M165C). Several grains with varying sizes (from 3 to 10 μm in diameter) were prepared, using this method for characterization by coherent X-ray scattering.

The scattering geometry of the experiment is shown in Figure 3.12. It includes a pair of coherence defining slits, located at a distance of 80.6 cm in front of the colloidal sample. Guard slits were positioned 29 cm in front of the sample to cut off the strong scattering signal, produced by the first set of slits. The colloidal crystal grain was mounted on a goniometer, which allows rotation of the sample around the vertical axis. An evacuated tube was positioned between the sample and the detector to reduce air scattering. The detector was positioned 5.3 m downstream from the sample. The diffraction data were recorded, using a charge-coupled device (CCD) detector (Roper Scientific, PI-LCX) with

a pixel size of 20×20 μm^2 and 1300×1340 pixels with a total field of view of 26×26.8 mm^2. The maximum detector resolution in this geometry was $q_{max} = 98\ \mu\text{m}^{-1}$. To protect the detector from the direct beam a round beamstop with a diameter of 2.5 mm was used.

Several individual grains of colloidal crystals were measured in azimuthal angular scans. In total, 180 diffraction patterns were obtained for each sample in one degree increments, covering the entire reciprocal space. For each angular position 10 to 100 diffraction patterns were measured to increase the dynamic range and to improve the signal to noise ratio. The exposure time ranged from 0.2 s up to 30 s per image, depending on the scattered intensity, to avoid oversaturation of the detector. The measured diffraction patterns at each angular position were averaged and the corresponding dark field images were subtracted. In addition, to measure detailed information about the shape of the crystalline part of the sample, fine scans with a step size of 0.2° were performed around selected Bragg peaks.

3.3.2 Results and Discussions

Typical diffraction patterns measured at different relative azimuthal angles of rotation φ from two different colloidal crystal grains are shown in Figure 3.13. Several Bragg peaks are clearly visible in these diffraction patterns. A very strong and distinct set are the hexagonal 220 Bragg peaks typical of the scattering on a FCC structure. Due to the finite size and internal structure of the crystal grains each of the measured Bragg peaks breaks into a complicated speckle pattern (see inset in Figure 3.13(c)). In addition to the Bragg peaks strong speckles over the entire diffraction pattern were observed, which are typical for coherent scattering experiments on colloidal samples [LMN$^+$08].

A strong q-dependence of the diffraction pattern, due to the variation of the form-factor of the individual colloidal spheres is observed in Figure 3.13 as well. The finite size distribution of these spheres does never let the q-dependence of the form-factor reach zero. But an enhancement of the speckle pattern in the range of the zero-order of the form-factor compared to the higher q-values can be seen in Figure 3.13. The strong flares in each diffraction pattern appear due to parasitic scattering from the slits located in front of the sample and scattering from the carbon fibers. Since the carbon fiber sample holders were not oriented vertically in the beam the scattering produced by them changed with the variation of the azimuthal angle φ.

The diffraction patterns produced by scattering of a coherent X-ray beam from two different colloidal grains look similar (Figure 3.13). However, there is one major difference in the observations. For one grain strong streaks through the Bragg peaks at a relative rotation angle of $\varphi = 80°$ (see Figure 3.13(b)) can be seen, which are similar to the earlier findings for a 2D film of colloidal crystal. Yet, no streaks were observed in the diffraction patterns during the entire scan for the other grain (see Figures 3.13(c) and (d)). Such streaks are an indication of defects in the crystalline sample [HAS$^+$09]. Based on this result, the conclusion could be drawn that the first grain contains structural defects and the second one does not. Such a conclusion about the structure of the sample, deduced only from the analysis of the 2D diffraction patterns, can be misleading, as will be explained later on.

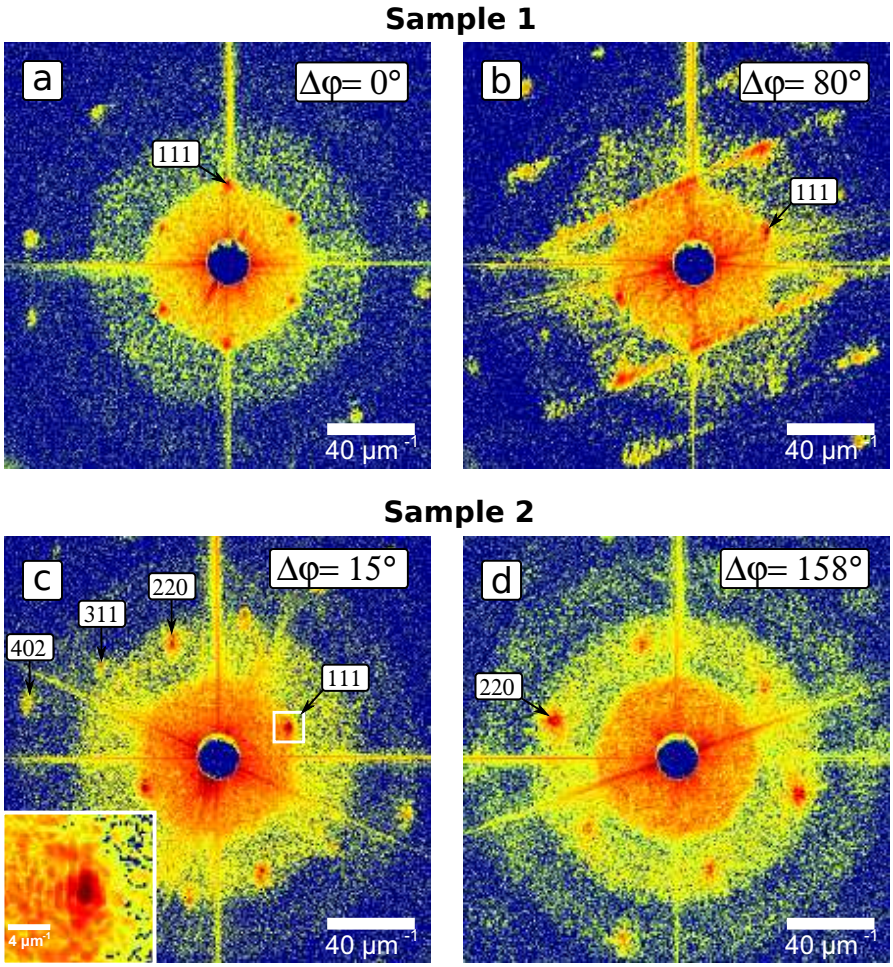

Figure 3.13: Selected diffraction patterns measured at different relative angles $\Delta\varphi$ of the azimuthal rotation for the colloidal grain one (a, b) and the colloidal grain two (c, d). The inset in panel (c) presents a magnified view of the region around the Bragg peak, shown by the white square.

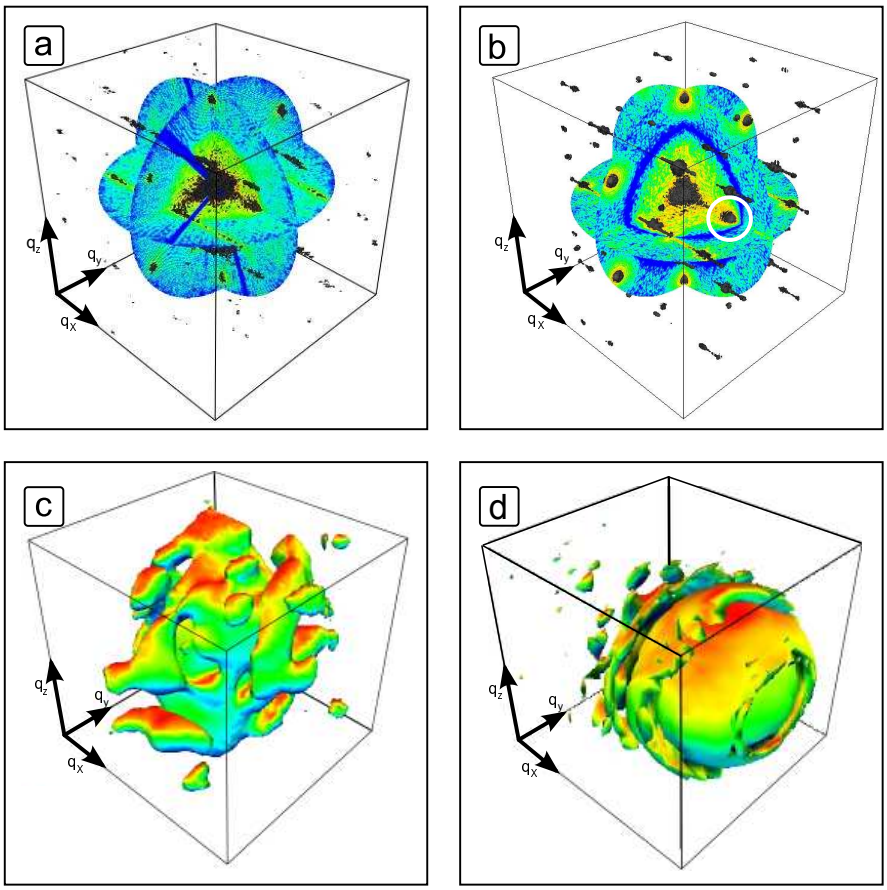

Figure 3.14: (a, b) A 3D representation of the measured (a) and simulated (b) scattered intensity, showing three orthogonal planes and an isosurface. The length of the arrows corresponds to 30 μm^{-1}. (c, d) An isosurface of measured (c) and simulated (d) scattered intensities around a 220 Bragg peak. The length of the arrows corresponds to 2.5 μm^{-1}.

All the 2D diffraction patterns measured from the second grain were combined into a 3D data set, using nearest-neighbor interpolation. Figure 3.14(a) shows a representation of the measured data in 3D, showing three orthogonal planes (cuts) through reciprocal space on a logarithmic color scale as well as an isosurface of the scattered intensity. In Figure 3.14(c) the 3D structure of the scattered intensity in the vicinity of a 220 Bragg peak for the same sample, obtained as a result of the fine angular scan, is presented. A complicated 3D intensity distribution can be observed in this figure. This implies that the 3D shape of the crystalline part of the colloidal grain under investigation is also complicated.

In the 3D representation of the coherent scattering from the second grain (see Figure 3.14(a)) streaks became visible indicating the presence of a defect in this sample as well. By analyzing the structure of the coherently scattered intensity already certain conclusions about the type of the defect can be made. The additional features in the 3D diffraction pattern have the shape of thin rods passing through the 111 Bragg peaks which clearly indicates that the colloidal grains contain a plane defect in a (111) plane. This cannot be a line defect, for example a linear dislocation, because that would produce additional scattering in reciprocal space in the form of a plane (see, for example [VZM$^+$08], where crystal truncation planes were observed in reciprocal space due to scattering on the line edges of the sample). These additional rods observed in the 3D intensity distribution can be attributed to scattering on a stacking fault present in the grain. In order to confirm these observations, simulations were performed based on a model of a colloidal sample similar to the one used in the experiment. The results of these simulations are presented in the following subsection.

3.3.3 Model Simulations

Diffraction patterns of coherent X-ray scattering at 7.9 keV incident photon energy for a model colloidal sample were simulated. The model was composed from colloidal spheres made from silicate with a diameter of 230 nm arranged in a FCC crystal lattice. The shape of the whole grain was taken in the form of an ellipsoidal particle with a total size of $5\times6\times7$ μm^3 (see inset in Figure 3.15(a)), which is comparable in size to the grains used in the experiment. In addition, a single defect in the form of a stacking fault was introduced inside the model grain particle.

We simulated 2D diffraction patterns from this structure for different angles of azimuthal rotation φ from 0° to 180° with an angular increment of 0.25°. Diffraction patterns were calculated, assuming kinematical scattering and plane wave illumination of the sample. A modified version of `MOLTRANS` was used, which allows particles of a few hundred nanometers in size as scatterers in the calculations. This yields the correct form-factor of the colloidal scatterers in the simulated diffraction patterns. All diffraction patterns were combined into a 3D data set, using the same approach as for the experimental data. Figure 3.14(b) shows the simulated scattered intensity in 3D reciprocal space in the same manner as Figure 3.14(a) does for the experimental data. Several common features can be identified while comparing these two images. The most prominent is again the hexagonal set of the 220 Bragg peaks. Around each Bragg peak

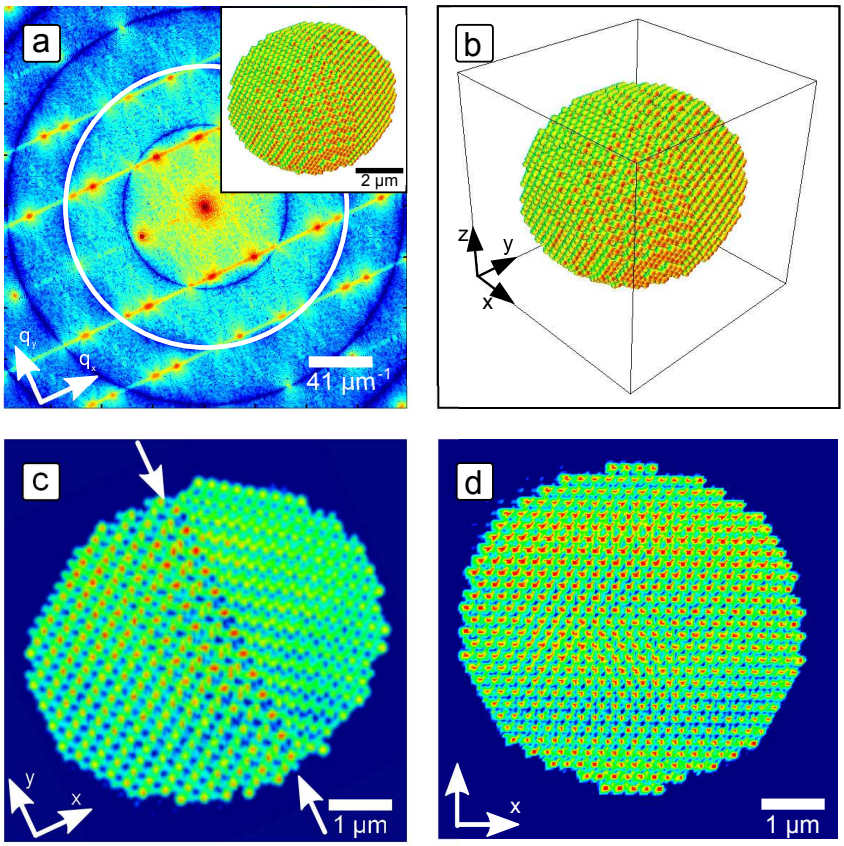

Figure 3.15: (a) The (q_x - q_y) cut in reciprocal space, showing the distribution of the scattered intensity on a logarithmic scale from the model colloidal sample presented in the inset. The white ring corresponds to the data used for the reconstruction. (b) An isosurface of the reconstructed object, the length of the arrows corresponds to 2 μm. (c, d) Two orthogonal cuts through the reconstructed object. The stacking fault, indicated by the arrows, is clearly seen in (c).

strong fringes, due to coherent scattering from the finite size crystalline particle, can be seen (see magnified view of a selected Bragg peak in Figure 3.14(d)). Moreover, six parallel streaks going through the set of 111 Bragg peaks can be observed, which occur due to scattering from the stacking fault, introduced in the model. The structure and position of these streaks in reciprocal space is the same as in the experimental data (see Figure 3.14(a)). The same features are well-distinguished in a horizontal (q_x-q_y) cut through 3D reciprocal space, obtained in the model simulations (see Figure 3.15(a)). For example, in the experiment as well as in the simulations, the streaks in reciprocal space form groups of two lines and no streak is present between these groups (see the absence of the streak through the origin of reciprocal space in Figures 3.13(b), 3.14(a,b), and 3.15(a)). This is typical for stacking fault defects without the shift of the neighboring atomic planes. In the case of a shift of atomic planes additional streaks will appear (compare to results in the previous section). Such behavior was not observed in this experiment. This assures that indeed a defect in the form of a stacking fault was observed in a single grain of a colloidal particle in the experiment.

3.3.4 Reconstruction Results from the Model Simulations

Attempts to reconstruct the full experimental 3D data set shown in Figure 3.14(a) were, unfortunately, unsuccessful. This can be attributed to the large amount of missing data covered by the beamstop, which is known to limit the reconstruction process [TEJ$^+$06], as well as to the parasitic scattering from the slits and the carbon fiber. An additional hindrance is the difference in resolution (statistics) due to the measurements with different exposure times. To gather the same amount of statistics the total exposure time for each diffraction pattern should be the same, even if this means that a great deal of diffraction patterns have to be measured with a short exposure time. With these long exposure times less diffraction data can be measured but it is of utmost importance to sum up to the same amount of total exposure time, which was not the case in this measurement.

The conditions, which are necessary for a successful reconstruction of a single colloidal grain, are discussed below, based on model simulations. To begin with, the simulated 3D scattered intensities shown in Figure 3.14(b) were phased, using an iterative phase retrieval algorithm. Starting from a rectangular support, the shrink-wrap algorithm was applied to find a better estimate of the shape of the object. For each reconstruction 100 iterations of the HIO algorithm were followed by 50 iterations of the ER algorithm. After each 900th iteration the Shrink Wrap algorithm was applied again to optimize the support. Figures 3.15(b,c, and d) show the result of the reconstruction after a total of 2700 iterations. In the reconstruction no significant difference to the initial model can be found. An outer isosurface of the grain, obtained from the reconstruction, (Figure 3.15(b)) is almost identical to the initial model (see inset in Figure 3.15(a)). Clearly, the crystallinity of the sample was reconstructed, showing the positions of each individual scatterer, which can be seen in a cut through the reconstructed sample in Figures 3.15(c and d). The defect, in the form of a stacking fault as a break in the FCC ordering, is also resolved in these ideal conditions. In the experiment the angular

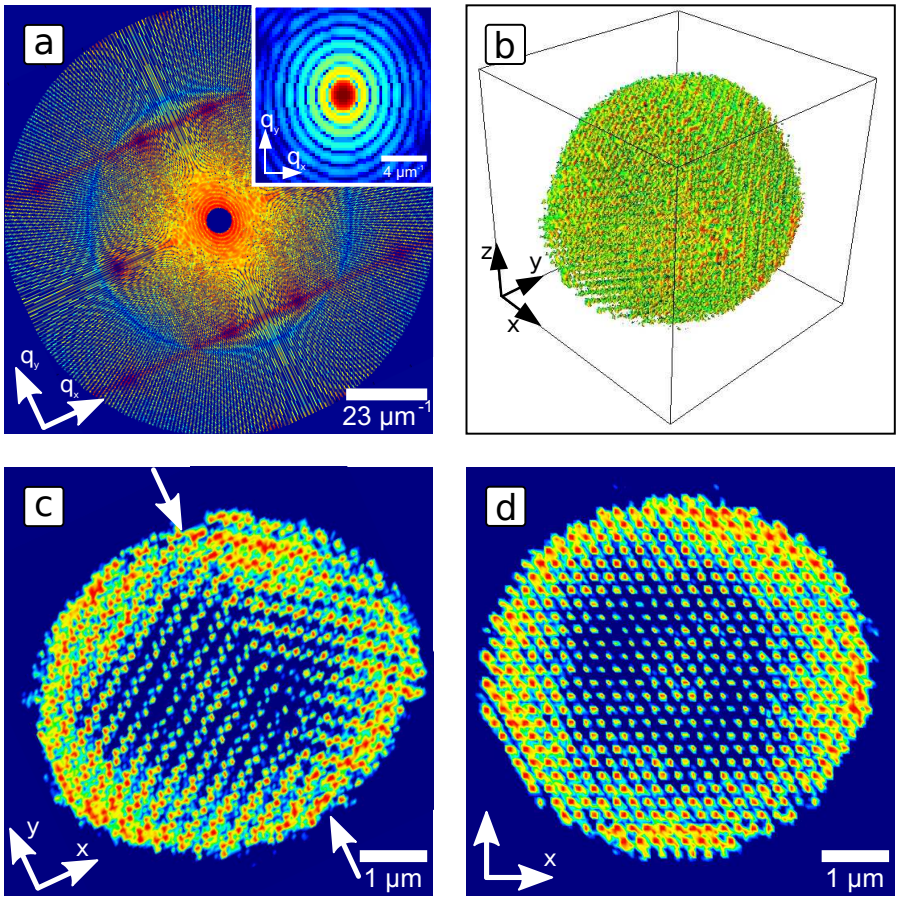

Figure 3.16: (a) The (q_x - q_y) cut in reciprocal space obtained from simulated 2D diffraction patterns with one degree increment. The missing region covers the central speckle and the first two fringes. (inset) A slice through 3D scattered intensity around a 220 Bragg peak, which was used to reconstruct the support. (b) An isosurface of the reconstructed object, the length of the arrows corresponds to 2 μm. (c, d) Two orthogonal cuts through the reconstructed object. The arrows in (c) point to the defect in the colloidal grain.

step size was one degree, which is four times bigger than in the simulations. This sparse angular sampling, as well as the necessary beamstop, may prevent successful convergence of the algorithm [HMS+09]. To investigate these complications in greater detail another set of simulations was calculated, where these questions of missing data and sparse angular sampling on the outcome of the phase retrieval were addressed. A subset of the simulated data was taken, with 180 diffraction planes in total and a one degree rotational increment similar to the conditions of the experiment.

The central part of the diffraction pattern was not used in the reconstruction to simulate a beamstop that covers the central speckle and two additional fringes. This corresponds to a beamstop size of 2 mm which is still slightly smaller than in the experiment. Figure 3.16(a) shows a (q_x-q_y) cut through the 3D diffraction pattern where artefacts appear due to the sparse angular sampling. In comparison to the previous simulation, when a finer step size of 0.25° was used (see Figure 3.15(a)), this data set clearly shows larger regions of missing data at high q-values. To address the problem of missing data in the low q-region as well as to obtain an estimate of the shape of the crystalline grain for the initial step of the 3D reconstruction the scattered intensity around a single Bragg peak was used (see inset in Figure 3.16(a)). As has been demonstrated in the experiment, this region of reciprocal space in the vicinity of a Bragg peak can be measured with fine angular steps and without a beamstop. The same reconstruction procedure as described before was applied to these data subsets and a good estimate of the support for the model grain was obtained.

It should be noted here that this procedure is clearly limited to crystalline particles. For example, if the crystalline particle is surrounded by a non-crystalline part, only the shape of the crystalline part will be reconstructed by applying this approach. The support found from the Bragg peak reconstruction was used to evaluate the intensity in the central part of the entire diffraction data. This missing central part of the diffraction pattern was substituted by the properly scaled central speckle, obtained from the Fourier transform of the support [NMI03]. The intensities in all other non-defined pixels were allowed to freely evolve in the iterative reconstruction process. The reconstruction was based on the repetition of 100 and 50 iterations of the HIO and ER algorithms, respectively.

In Figures 3.16(b), (c), and (d) the results of the reconstruction after 2700 iterations are presented. The crystallinity of the sample and, importantly, the stacking fault are still clearly resolved. In comparison to the result presented in Figure 3.15 the overall image quality decreased. In particular non-uniform density variations across the sample are noticeable. These artefacts appear due to unconstrained modes in the central part of the diffraction pattern [TEJ+06]. The simulations have also shown that attempts to reconstruct the structure of the colloidal grain with a larger region of missing data in the central part of the diffraction pattern were not conclusive. This indicates that in order to obtain a reliable reconstruction applying the conditions of the experiment the beamstop should not be substantially bigger than the central speckle. The performed simulations were made with noise-free data. Experience shows [HMS+09] that a small degree of noise (variations of a few percent in intensity) does not change the results significantly.

In summary, a grain from a colloidal crystal was investigated, using coherent X-rays. The diffraction patterns were recorded in a rotational series and then combined into a 3D data set. The simulations show that such a data set has the potential to be reconstructed, using phase retrieval algorithms.

3.4 Coherent X-ray Nano Diffraction on single GaAs Nanowires [GMM+11]

In this section an experiment is presented to show the potential of CDI for another class of samples, namely nanowires. In recent years it has been demonstrated that new solid-state materials, one-dimensional (1D) crystals in the form of nanowires, nanotrees, and nanoflakes can be synthesized by a range of well-established techniques for growing semiconductor materials [JKP+06]. A special focus has been laid on bottom up techniques, where the growth of nanostructures is promoted by the presence of ultra fine catalyst particles, which act as nanoscale melting pots [WE64]. An alloy is formed at elevated temperatures, consisting of the molten metal particle and semiconductor atoms supplied from a dilute gas. When this alloy is saturated a fine crystalline wire grows epitaxially between particle and substrate. Pursuing this growth at low pressure leads to a forest of micrometer long, uniform, and essentially 1D nanowires. The details of the growth process are, however, still being debated for example, whether or not the catalyst melts during the growth and how the constituents arrive at the growth interface, by diffusion through the catalyst or along the interface [KYS+09]. Understanding the growth process is pivotal in the effort to better control of the nanostructure properties, namely, morphology, structure, and purity, which are essential to fabricate nanowires for practical applications, such as biosensing [BSNM09], solar cells [AJS+07], batteries [CPL+08], and future computing devices. In order to understand the growth strong characterization tools for both ensembles and single wires are required. To this end, this section addresses the possibility of single nanowire X-ray diffraction experiments. The structure of objects on the nanoscale determines the physical properties of macroscopic materials, which is why it is increasingly important to investigate the structure of nanoscale objects. X-ray scattering gives access to local chemical, elemental, and structural information and provides an ideal tool to investigate matter on the nanoscale.

For many years the most common nanowire catalyst material has been Au due to its unique ability to promote nanowire growth. The incorporation of Au, which may create deep levels, acting as recombination centers, hence degrading the electronic properties of the material, is still ambiguous [PAM+06, AHP+08]. Formation of Au-free GaAs nanowires, grown by MBE, has recently been demonstrated with a thin deposited layer of SiO_2 on Si or GaAs substrates [iMCA+08, CSF+08], where the obvious advantage is the absence of Au and the particularly low C environment. The detailed atomic structure depends critically on the choice of composition and growth parameters, which makes it possible to tailor the structural phase along the typical (111) crystal growth direction, switching between the two possible structures, the cubic zincblende (ZB) and the hexagonal wurtzite (WZ) phase. In this way phase perfect wires were recently

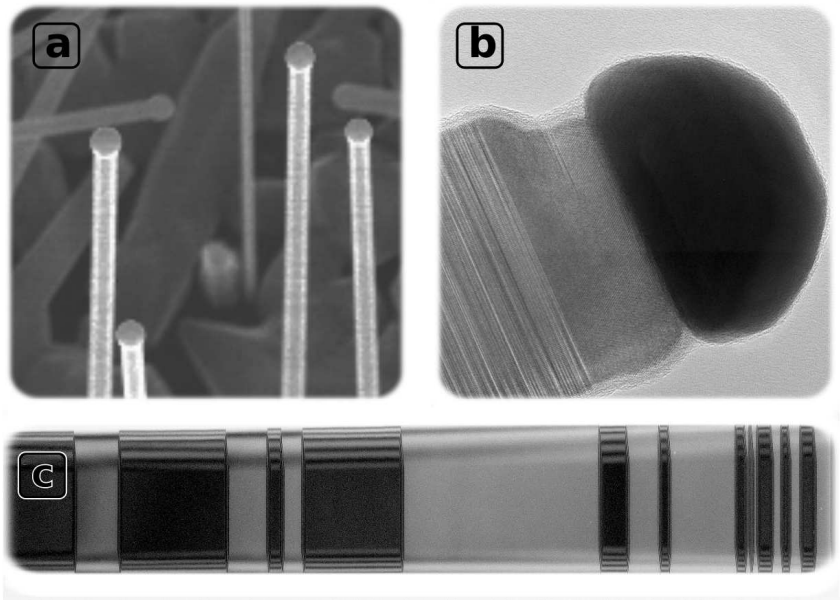

Figure 3.17: SEM images of nanowires. (a) showing an assembly of nanowires similar to the nanowires used in the measurement. (b) a detailed view of the tip of a nanowire, showing the complicated structure as a result of the growth process. (c) a detailed view of the nanowire, showing the wurzite and the zincblende structure along the wire.

obtained by using specific growth parameters [JWLG$^+$10].

The structure of III-V nanowires is, however, usually complicated and contains extended domains with mixed WZ or ZB structure, both regular and twinned, as well as numerous stacking faults. Even a regular super lattice stacking of nanoregions of regular and twin structure has been found [MrA$^+$07, JWDS06]. For pure liquid Ga-assisted GaAs nanowires it is known that the wires naturally change their structure from ZB to WZ during growth [SAG$^+$09], which makes the situation more complicated. Figure 3.17 shows SEM images of nanowires where the complicated structure can be seen.

The combination of the often complicated nanowire structure and the influence of the structure on the nanowires' physical properties suggest the use of both new and well-proven characterization methods. To this end, the structure of III-V nanowires has been extensively investigated by TEM on single wires and X-ray scattering on the full forest of epitaxial wires or flakes [JBHC99, AJS$^+$07, MrA$^+$07, MLD$^+$09, MLD$^+$09]. X-rays have proven to be a powerful tool for measuring ensemble average properties of entire forests of nanowires. With this technique it is possible to characterize structures by crystal truncation scans. By analyzing the shape of the individual Bragg reflections the external shape of the nanowires can be determined [MrA$^+$07]. To extend this to single nanowires, or more generally to nanoobjects, an X-ray setup with a nanofocus is required [SKP$^+$05], an option which only exists due to recent achievements in X-ray source and

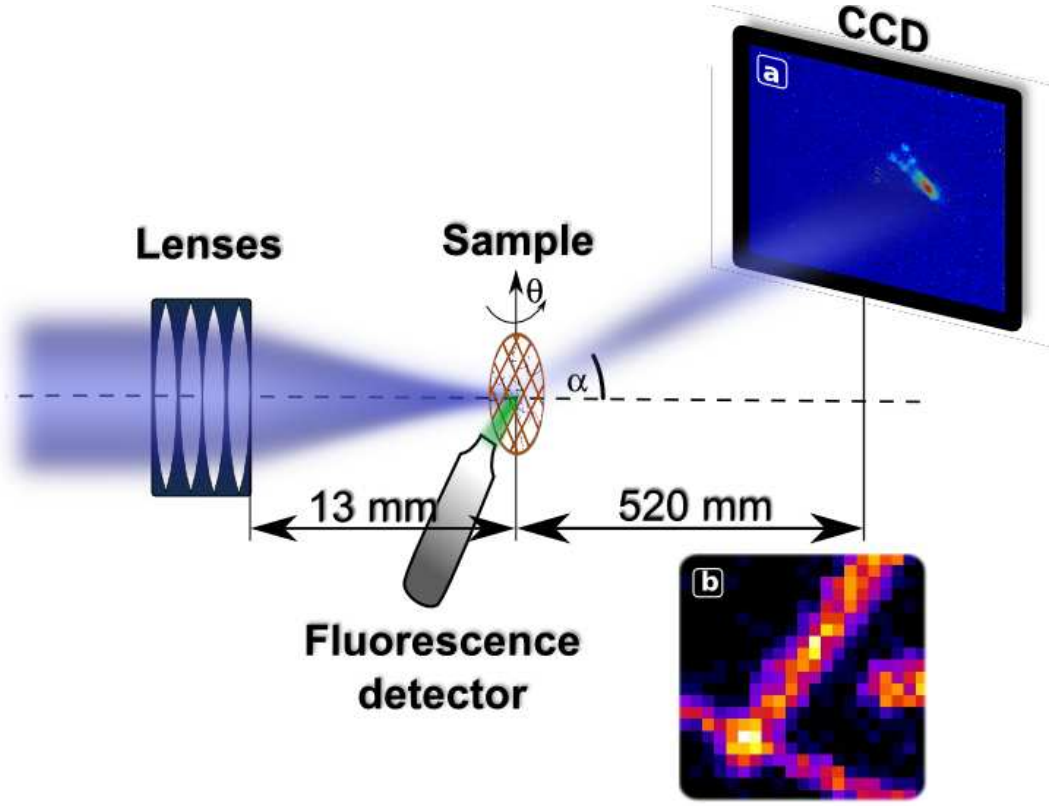

Figure 3.18: Schematic view of the experimental setup. (a) A diffraction pattern recorded at an angle of $\alpha = 11.3°$. (b) Fluorescence map of the scanned region.

optics development. The very small focal size opens the possibility to illuminate a single nanowire within an assembly. In addition, the high degree of coherence in the focus of such a beam has the chance to potentially apply CXDI to investigate the structure of a single nanowire.

In this section, the result of a coherent diffraction experiment on a single GaAs nanowire, which besides the relevance to nanowire science, can serve as an ideal test object for coherent nanodiffraction imaging with high-spatial resolution, is presented.

3.4.1 Experiment at ID13 at ESRF

The experiment was performed at the nanofocusing beamline ID13 of the European Synchrotron Radiation Facility (ESRF) with an X-ray energy of 15.25 keV. The diffraction geometry of the experiment is shown schematically in Figure 3.18.

The GaAs nanowires were grown on a Si (111) substrate by molecular beam epitaxy. The conventional Au catalyst particles were substituted by Ga droplets. The typical dimensions of the nanowires in this sample were 120×140 nm in diameter and 7-8 μm in length.

The GaAs nanowires were brushed off the substrate onto a TEM grid and positioned in the focal plane of two cylindrical Si compound refractive lenses [SKP+05]. These were aligned perpendicularly to each other, each focusing the beam in one dimension. This setup produced a 150×150 nm^2 focus, that is just bigger than the nanowire diameter. The focus position was 13 mm behind the last lens [SBF+10]. The sample position was adjusted by a set of piezo stages. In addition, the sample could be rotated around both axes perpendicular to the incoming beam direction. Especially important was the rotation around the vertical axis which was scanned to sample the diffracted intensity in a 3D volume around a Bragg peak. An on-axis microscope was used for coarse sample positioning.

A fluorescence detector was positioned close to the sample perpendicular to the beam. It was used to locate a single wire on the TEM grid by mapping the combined fluorescence signal of Ga and As. In Figure 3.18(b) a fluorescence map with a step size of 100 nm is shown. Three isolated GaAs nanowires can be resolved in this image. The coherent diffraction signal was recorded by a single photon counting, noise-free MAXIPIX detector with 256×256 pixels. Each pixel has an area of 55×55 μm^2. The detector was positioned 520 mm downstream from the sample to record the forward scattering signal. A 1.5 mm wide beamstop was used to prevent damage to the detector from the direct beam. For the measurements of the Bragg peaks the detector was moved away from the optical axis. At an angle of a α =11.3° the 101 WZ Bragg peak was accessible. An example of a diffraction pattern measured in this geometry (see also Figure 1.13) is shown in Figure 3.18(a).

3.4.2 Results and Discussion

Coarse fluorescence map scans were used to locate the wires. With finer scans a specific location on a nano wire was chosen. Then several of the isolated nanowires were investigated in the forward scattering geometry. In addition to single wires, more dense regions were illuminated, in which several wires were simultaneously placed in the focus of the X-ray beam. No significant scattering signal could be measured due to the relatively large beamstop. Longer exposure times, which should increase the scattering signal, were limited by radiation damage of the sample. The damage occurred to the supporting film before the nanowires were damaged, which reduced the stability of the setup. The damage could be observed by the on-axis microscope as black dots on the membrane.

In the next step, single nanowires were measured in the diffraction geometry where the detector is offset from the optical axis, which has the additional advantage that the direct beam does not hit the detector and therefore no beamstop is needed. The diffraction signal around a WZ 101 Bragg peak for different angles θ of sample rotation (see Figure 3.18) was measured, covering a range of 3° with a step size of 0.05°. In Figure 3.19 each tenth diffraction pattern is shown. During the scan the diffraction signal drastically changed, depending on the angle of rotation. The Bragg peak was observed over a range of 3°, in which the position of the Bragg peak on the detector changed. Beyond the 3° range the scattering signal of the Bragg peak was no longer

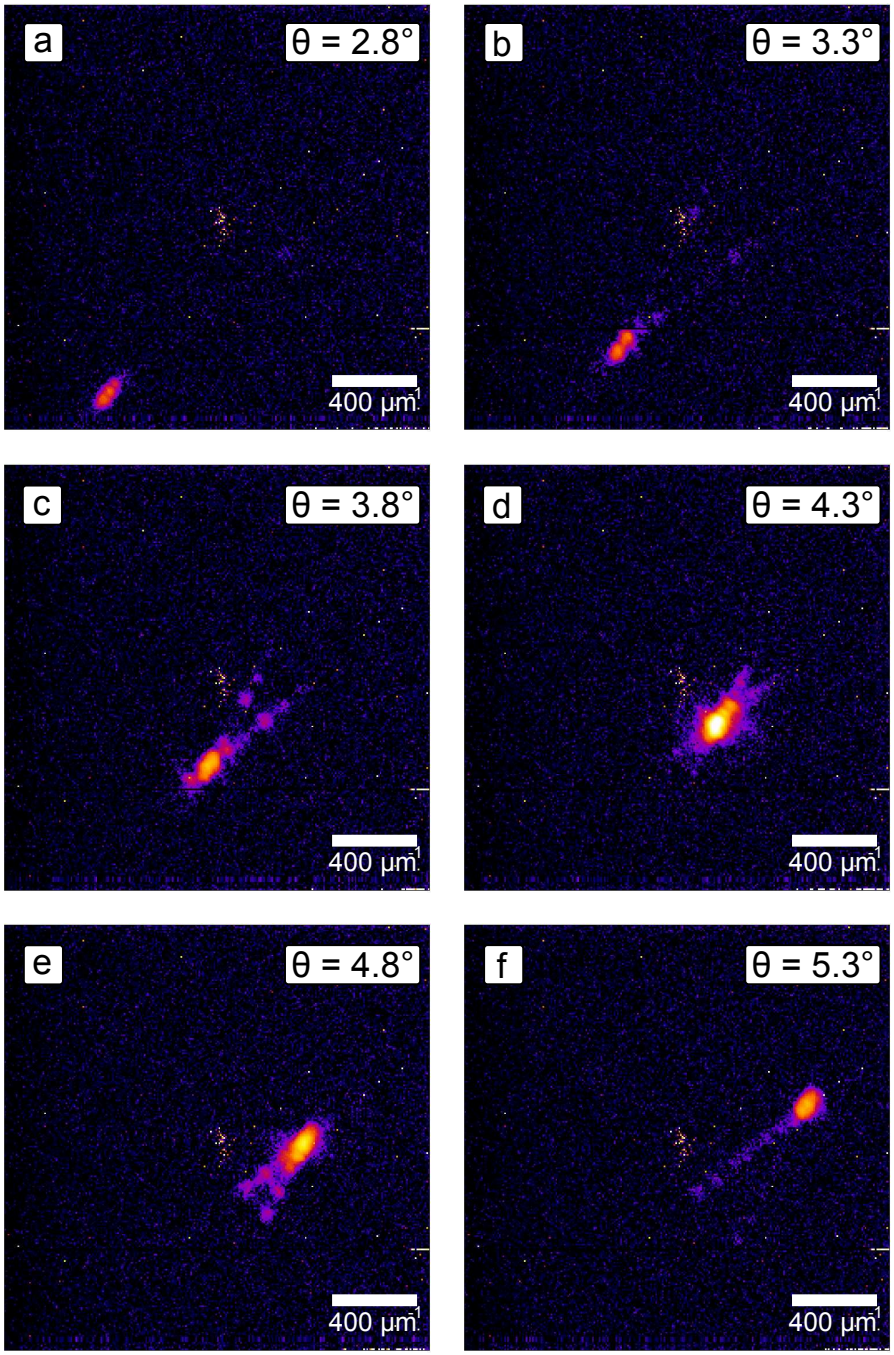

Figure 3.19: Diffraction patterns measured at different angles of sample rotation, shown on a logarithmic scale. The position of the Bragg peak on the detector changes and a complicated diffraction signal around the Bragg peak is observed.

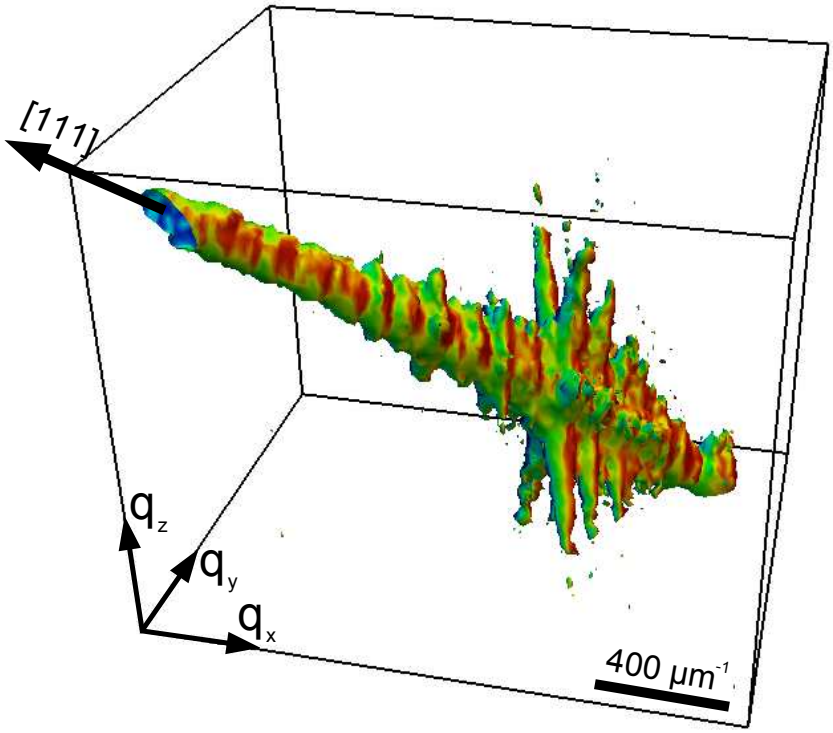

Figure 3.20: A 3D isosurface of the scattered intensity in the vicinity of the Bragg peak in reciprocal space, combined from 60 diffraction patterns.

strong enough to be measured.

The different positions of the Bragg peak in the detector correspond to different scattering vectors and are the sign of a crystal truncation rod (CTR), originating from the center of the Bragg peak. This gives rise to an elongated shape of the Bragg peak (see Figure 3.19). The intensity distribution in reciprocal space is given by a Fourier transform of the crystal shape function. Any sharp truncation of the crystal causes a streak of scattering that is the CTR along the surface normal in reciprocal space. At the angles closest to the center of the peak additional CTRs, originating from the center of the peak but emanating in various directions in reciprocal space, can be seen (Figures 3.19(c - e)).

Each diffraction pattern represents a cut through 3D reciprocal space. By combining these slices the full 3D information around a Bragg peak can be obtained. The result of the measurement reveals a complicated structure, which can be seen in an isosurface of the scattered 3D intensity presented in Figure 3.20. The elongation of the peak is the CTR of the nanowire and exhibits a clear sign of stacking faults or twin planes along the growth direction of the wire. The fringes along the rod in reciprocal space occur due to the coherent interference from the size of investigated features. The smaller CTRs, which form a weak, six-armed star, arise from the nanowire's side facets and show the

hexagonal shape of the nanowire. The existence of several such stars confirms that the diffraction from several independent domains in the nanowire was measured, which have the same facet structure (Figure 3.20). Due to the slight phase difference of two WZ domains separated by a single twin plane the scattering from such two domains is slightly separated in reciprocal space. The three hexagonal stars correspond to the three possible WZ stacking sequences and the fact that they are all roughly equal in magnitude shows that the WZ domains are not only significantly smaller than the X-ray focus size but also randomly distributed.

The measurements were repeated on different locations along the nanowire that, in one dimension, extends much longer than the size of the beam. The overall structure of the Bragg peak remained independent from the position on the wire. The hexagonal CTRs, however, were observed only on the measurement position closest to the tip of the wire, which indicates that the long nanowire only has extended WZ domains with well-defined facet structures at the tip.

Due to instabilities during the measurements the observed contrast in the images was not sufficient and prevented a direct reconstruction of the recorded diffraction patterns with conventional iterative phase retrieval methods. Similar experiments were previously performed on shorter, thicker, and/or more uniform nanowires [FNEKG09, DMS$^+$09, BDP$^+$09]. The results of these experiments were limited to obtaining the shape of the wire with low resolution. A complicated structure like the one studied here, with the existence of several independent domains, has not yet been reconstructed successfully. But future experiments, which follow up the idea presented here, will potentially reveal the inner structure of nanowires through CXDI.

3.5 Conclusions and Outlook

In summary, this chapter demonstrated that the simple and nondestructive mechanism of coherent X-ray diffractive imaging opens a unique route to determine defects in mesoscopic materials. CXDI together with new hard X-ray microscopy methods has the potential to provide detailed information about the local defect structure in colloidal crystals. This is especially important for imaging of photonic materials when refraction index matching is not possible or the sizes of colloidal particles are too small for conventional optical microscopy. A model system was presented, including most of the effects seen in the measured data, also supporting the results from the reconstructions. To extend this method to larger fields of view scanning methods such as ptychography have to be used.

The subsequent section discussed an experiment, where coherent X-ray diffraction patterns from isolated colloidal crystal grains were recorded at the coherence Beamline P10 at PETRA III, covering several Bragg peaks as well as the coherent interference signal between the peaks. Different grains were measured in rotation series. These diffraction patterns were combined into a 3D data set, containing the structural information about the object in reciprocal space. Streaks in reciprocal space were observed, which are a clear indication of a plane defect in the grain.

The observations were confirmed by simulations performed on a model of a single grain of a colloidal particle with a defect in the form of a stacking fault. The 3D distribution of intensity from that model has similar features to those observed in the experiment, which supports the conclusions drawn from the analysis of the diffracted intensities. The simulated intensity distributions were inverted using iterative phase retrieval methods. The results of the 3D reconstruction revealed the shape and the inner structure of the grain. The position and the structure of a stacking fault defect were obtained with high resolution as well.

It was proposed to use the results of the reconstruction of the data collected around the Bragg peak in order to determine the tight support which is required to treat the missing data problem. The simulations show that diffraction patterns collected in the conditions close to the experiment, with the rotation step of one degree and the beamstop covering the central speckle as well as two additional fringes, are sufficient for a successful reconstruction. With this knowledge, in future experiments, it is planned to collect a set of data that will be sufficient to retrieve the structure of individual grains, showing the positions of the individual colloidal particles including possible structural defects. It was shown in section 3.1.2 that this is especially important to understand the nucleation of crystal growth.

The last section of this chapter presented an experiment which was carried out at the hard X-ray nanobeam scanning X-ray microscope at ID13 of the ESRF. The experiment was used to perform a coherent diffraction experiment on single GaAs nanowires. Diffraction patterns in the vicinity of a Bragg peak were measured locally in a small region of a selected nanowire and the origin of the different features were explained. It appears to be evident that the extension to anything but forward scattering are nanowires fixed on a substrate, which allows much easier handling and orientation as well as greater stability. With further development of the measurement CXDI can possibly provide high resolution images of the complicated nanowire structure.

This chapter showed the potential of CDI to reveal the inner structure of nanostructured materials. Future experiments will exploit the conclusions drawn here and will help the understanding of the crystal growth process as well as the development of new materials. The main limitation of most experiments carried out at synchrotron sources, however, is the restriction to static measurements. Dynamical processes, especially when they happen on the ultra fast timescale, have to be studied by a different method. The next chapter will, with the help of two example experiments, demonstrate the potential of FEL radiation for the visualization of ultrafast processes.

4 Experiments at FLASH

To overcome the radiation damage problem in X-ray imaging it was proposed to use ultrafast FEL radiation for probing the sample [NWvdS+00]. Important milestones towards the ultimate goal of single molecule imaging have been set. Two experiments using the ultrafast time structure of the FEL radiation are presented in this chapter. The first one demonstrates the fundamental principle of SAB CDI in a simple experiment performed at FLASH. The experiment was carried out on an artificial 2D crystal and a reconstruction with 200 nm resolution was performed. The second experiment discussed here illustrates the potential of using single FEL pulses to probe an excited material. The excitation happened through an intense IR laser pulse pumped into a colloidal crystal sample. Furthermore, ultra fast structural dynamics in colloidal crystals on the picosecond timescale will be presented. The temporal changes of the Bragg peaks were analyzed and their frequency components were calculated using a Fourier analysis.

4.1 Coherent-Pulse 2D Crystallography Using a Free-Electron Laser X-ray Source [MSR+09]

Revealing the structure of protein molecules is mandatory for understanding the structure of larger biological complexes. The knowledge of the functionality of biological systems on different length and time scales is at the forefront of modern structural investigations. The major progress in uncovering the structure of proteins in past decades was due to the development of phasing methods [WHF05], allowing the determination of the structure of complex molecules that crystallize. In spite of considerable progress in macromolecular crystallography, crystallization and radiation damage are still a bottleneck in protein structure determination.

One new approach to overcome these difficulties is based on the use of ultrashort pulses of X-ray free-electron lasers. An elegant idea is based on measuring a sufficiently sampled diffraction pattern from a single molecule illuminated by an FEL pulse [NWvdS+00]. Femtosecond single pulse imaging was recently demonstrated [CBB+06, CHRB+07, BBB+08] at the FLASH Facility in Hamburg [AAA+07]. However, in spite of the extreme intensity of the FEL pulses, a diffraction pattern from only one molecule will not be sufficient to obtain a high resolution diffraction pattern. Many reproducible copies will need to be measured to get a sufficient signal-to-noise ratio for each projection, which is necessary for three-dimensional (3D) imaging at subnanometer spatial resolution. These noisy diffraction patterns will necessarily be of random orientation and their classification is not straightforward [HSH03, BF07, FSSO09, LE09, LBE+10, BT11], requiring further development.

Alternatively, two-dimensional (2D) finite crystals can be used to reveal the structure of single molecules. It is well known that a 2D infinite crystal cannot exist due to logarithmically growing fluctuations [LL96]; however, there are no limitations for the existence of 2D finite crystals. As a result, all molecules, or any other biological complexes arranged in a 2D crystal with identical unit cell structure, will provide an enhanced signal in a single shot diffraction pattern from FEL sources. This can be especially important for membrane proteins which are difficult to grow in 3D crystals, but easily form 2D crystalline structures [UK83, KVM$^+$97]. This approach is particularly attractive, since the enhancement of the signal-to-noise ratio, due to the periodicity, improves as the square root of the number of repeated unit cells. In general, the enhancement of the diffracted signal is proportional to the number of unit cells N, but the noise in each pixel due to its statistical nature is proportional to the square root of the intensity. Therefore, it can be seen that the improvement in the signal-to-noise ratio only increases with the square root of N. In addition, the unique opportunity to exploit an extension of this approach by collecting diffraction patterns from reproducible 2D crystals at different known orientations is possible. This enables complete 3D imaging of biological samples.

CXDI with application to 2D crystallography was tested earlier with a computer generated 2D crystal structure [MS00] and a finite periodic array of nanoislands [VR03]. Here, a proof-of-principle CXDI experiment on a 2D finite crystal structure is performed on FLASH.

4.1.1 Experiment

Free-electron lasers are especially suited for such coherent 2D crystallography. They provide femtosecond coherent pulses with extremely high power. Only the combination of these unique properties will allow the realization of 2D crystallographic X-ray imaging on biological systems. Brilliant, ultrashort pulses could overcome the radiation damage problem [NWvdS$^+$00] which is a severe limitation of conventional crystallography at third-generation synchrotron sources [NG05]. Higher brilliance and hence improved statistics for such experiments can be obtained by the use of pulse trains that can be provided by FLASH and the European XFEL. It should be noted here that the detector development is not yet at a state to discriminate between the individual pulses within pulse trains.

During the experiment FLASH was operated in a regime producing 21 bunches of electrons per pulse train with a pulse train repetition rate of 5 Hz. The bunches within each pulse train were spaced at 1 MHz. The average pulse energy was 15 μJ, which is equivalent to $6 \cdot 10^{11}$ photons per pulse or $1.3 \cdot 10^{13}$ photons per train at the source. The diffraction data were measured at FLASH on the PG2 monochromator beam line [WMW$^+$07] with a fundamental wavelength of 7.97 nm. The monochromator was used in specular reflection (zeroth order) mode. The last mirror of the beam line is a focusing mirror with long focal length ($\geq$ 2 m), which provides an image of the source. A beam size in the focal plane of the order of 150 μm FWHM in horizontal and vertical directions with a flux of $4.5 \cdot 10^{10}$ ph/pulse was determined by ray tracing.

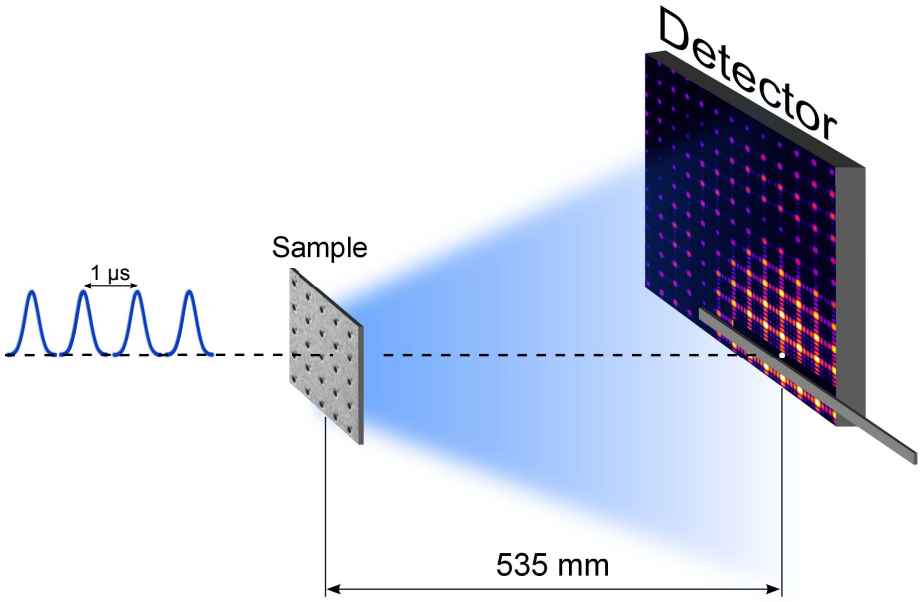

Figure 4.1: A sketch of the experiment. The FEL beam first interacts with the sample, and then the diffracted radiation propagates to a CCD detector. To enhance the measured resolution of the data the direct beam was incident near the corner of the detector.

Crystallography was demonstrated on crystals of finite size by using a crystal array that was prepared on a 100 nm thick Si_3N_4 membrane coated with 600 nm of Au and 200 nm of Pd. The finite crystal sample was manufactured by milling holes in the film in a regular array pattern, using a FIB. The unit cell of the crystal consists of a large hole of 500 nm diameter, representing a heavy atom and a smaller hole of 200 nm diameter, representing a light atom. The centres of these holes were separated by 495 nm. The whole structure is composed of five unit cells in each direction, making the total structure size about $10 \times 10 \mu m^2$ see Figure 4.3(a).

The experiment was conducted in a dedicated CXDI vacuum chamber, which was connected to the PG2 beam line. The chamber consists of an upstream shutter, a sample stage, and a flight tube to the charged-coupled device (CCD). The FEL beam was incident on the sample at a distance of 71.5 m from the source. The diffracted radiation then propagated 535 mm to the detector position (see Figure 4.1). The detector used was an in-vacuum CCD (PI-MTE 2048B) with 2048 $\times$ 2048 pixels, each 13.5 μm square with 16-bit digitization. For a 10 μm sample size with these experimental conditions the far-field condition is well satisfied and the diffraction pattern is adequately sampled with a sampling rate of 30 pixels in each direction. A series of single pulse train data was collected from the sample with a coherent flux on the sample area of $1.5 \cdot 10^{10}$ photons per pulse train. This is an order of magnitude higher than the expected coherent flux of about $3 \cdot 10^9$ photons on the same sample area for the same exposure time at a third generation synchrotron source. This estimate is based on a coherent flux of 10^{12} photons per second with the same incident photon energy and beam size as in the experiment at a third-generation synchrotron. The estimate implies that measurements using FELs can be performed in less than one tenth of the collection time required by a synchrotron and orders of magnitude less in exposure time due to the femtosecond FEL pulses. This is especially important in the case of radiation sensitive biological materials. A beamstop was positioned in front of the CCD to protect the camera from the direct beam. A typical data set is shown in Figure 4.2(a). It demonstrates an excellent visibility for the 2D finite crystal structure of 10 μm size. By comparing the visibility (98%) of the measured data with a simulated diffraction pattern it can be concluded that the incident beam is fully coherent across the spatial extent of the sample.

The diffraction pattern in Figure 4.2(a) contains signal up to the edge of the detector, which corresponds to a minimum feature size of 220 nm. All expected features of a finite, crystalline structure are observed. The Bragg peaks, due to the regular array, are clearly visible, as are the oscillations between the Bragg peaks that are the result of the finite extent and coherent illumination of the sample, as explained in section 1.3.2. Moreover, the form factor from the individual elements (the large holes) can be observed as a radial intensity modulation across the pattern. This is also very similar to the observations on colloidal crystals (see chapter 3).

4.1.2 Reconstructions

Several steps were implemented to perform a phase retrieval reconstruction from the measured diffraction pattern shown in Figure 4.2(a). The raw data were first corrected

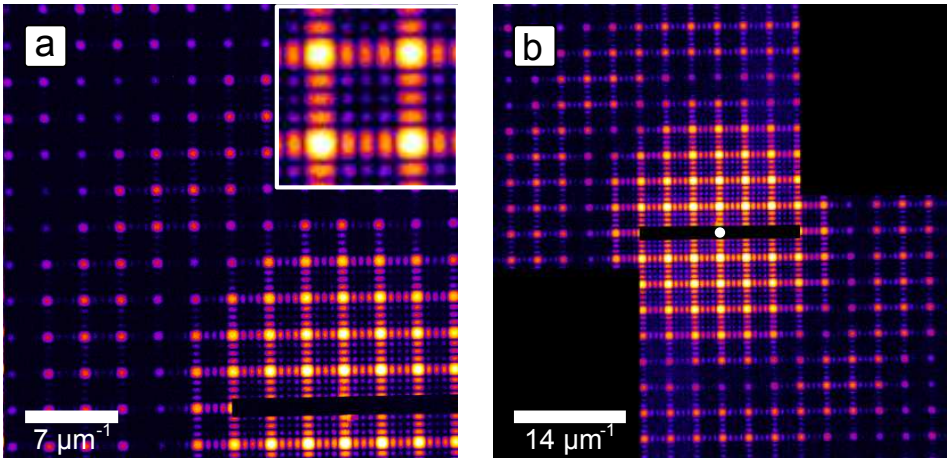

Figure 4.2: (a) Far-field diffraction data measured from a single train of 21 femtosecond pulses from the FEL. (Inset) Enlarged region of diffraction pattern. (b) A symmetrized version of (a) used for reconstruction. The region in black corresponds to missing data covered by the beamstop and unknown data regions after the symmetrization. The white dot corresponds to the center of the incoming beam.

for background effects by subtracting dark field images. The data were then symmetrized about the center and the pattern was binned (3×3), which improves the signal-to-noise ratio of the measured data (see Figure 4.2(b)). Symmetrizing the data is justified by the assumption that the sample is an amplitude object since the incident radiation is totally blocked except at the holes and, consequently, the measured diffraction pattern must be centrosymmetric. It is important to note here that the biological systems to be studied with pulsed FEL beams in the future will rather be phase objects. With the exception of symmetrizing the data set the results obtained in the present research can nonetheless be extended to phase objects. After symmetrizing and binning the image was 967×967 pixels in size. This data set is shown in Figure 4.2 (b). This array was embedded in a larger 2048×2048 pixel array to avoid artifacts in the reconstruction due to aliasing effects. The effective pixel size of this new array was 51.5 nm (which is clearly not the achieved resolution value as the data was measured to a resolution of 220 nm). The regions without measured data were allowed to freely evolve during the reconstruction without additional constraint. This preprocessed data set was used for reconstruction by applying the HIO iterative phase retrieval algorithm. A scanning ion micrograph (SIM) image of the sample is shown in Figure 4.3(a). The initial square support used for reconstruction is indicated by a dashed line in Figure 4.3(b). For the reconstructed image shown in Figure 4.3(c) 1000 iterations of the HIO algorithm with square support and positivity constraint were used[1]. It can be seen that the periodic array of large holes is successfully reconstructed, however, the small holes of 200 nm in diameter are

[1]The final reconstructions were performed by Adrian Mancuso.

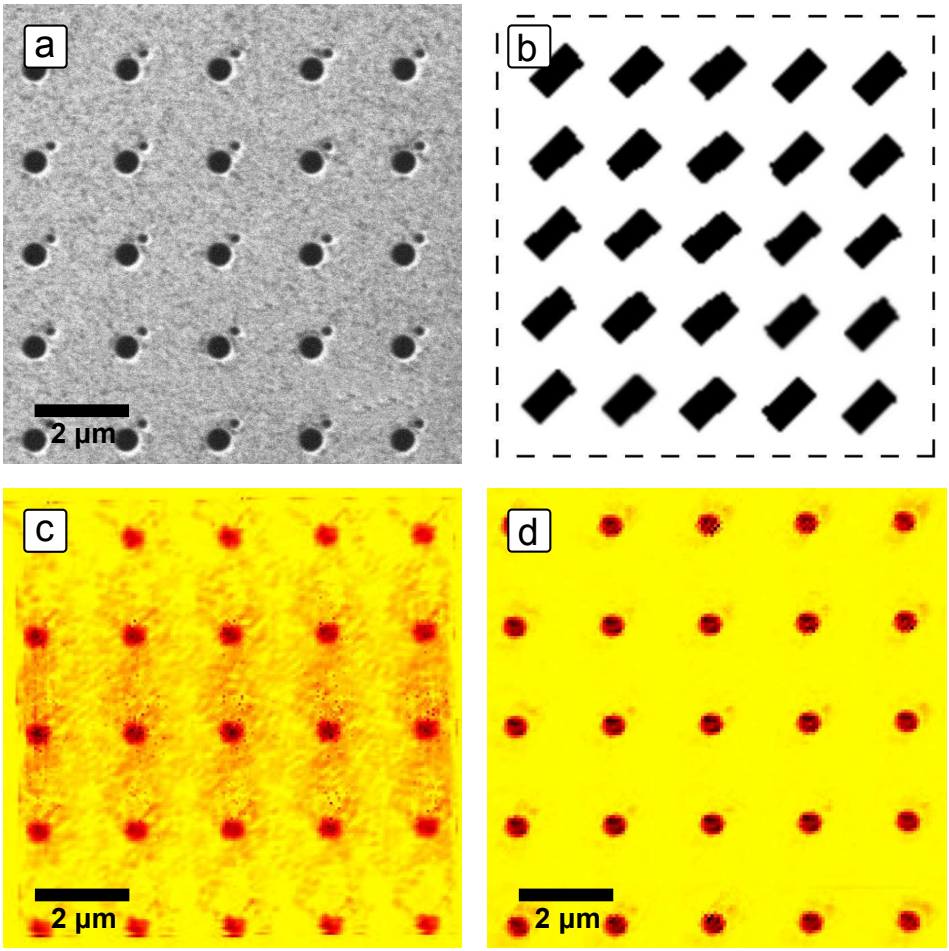

Figure 4.3: (a) SIM image of the finite, periodic structure. (b) Support region used for the reconstruction of the diffraction pattern. The large rectangular support (dashed line) was used in the reconstruction shown in (c). The support in the form of 25 rectangular boxes was used in the reconstruction shown in (d). (c) The initial reconstructed image with the original data binned 3×3. (d) The final reconstructed image using the original data binned 5×5. The scale bar is 2 μm in length.

missing. Also the diffuse, elongated background present in the reconstruction has to be noted.

Considerable efforts were taken to reconstruct the diffraction data with a better resolution. Since the maximum scattering angle suggests a theoretical resolution of 220 nm the small holes, representing the light atoms, should be resolved. One known hindrance for the reconstructions is a too loose support. The wide square support used in the prior reconstructions leaves too much space for the reconstructed object to float around. In the case of a complicated and unknown shape of an object it is common to use the Shrink - Wrap algorithm to confine the support dynamically during the reconstruction process. However, this proved to be challenging, since the correct value for the cut off in the shrinking procedure has to be found manually. For too high values individual holes from the known structure were cut and suppressed in latter iterations. For the case that the value is set too low the elongated background present after the first reconstructions becomes part of the support and also hinders a clean reconstruction. Even with manual adjustment the attempt to reconstruct the object with a quality to observe all 25 small holes was unsuccessful. In some cases however, the small hole was seen after the reconstruction in the correct position near the bigger void. This indicates that the resolution of the measured diffraction pattern potentially allows for a reconstruction showing the small holes.

One possible explanation of these difficulties with the reconstruction is that the measured diffraction pattern has two equivalent, symmetric solutions. One solution with the small dots appearing to the top right of the larger dots, and the other one with them appearing to the bottom left. This so-called twin image was introduced in section 1.4.6. Because of this symmetry the reconstruction algorithm does not fully converge, but rather stagnates with two equivalent solutions superimposed with each other. As the measured data is highly oversampled it can be binned further and in this way the signal-to-noise ratio can be improved. The data was binned 5×5,yielding a sampling rate of 6 in each dimension. Besides, instead of a large square support, a more constrained support of 25 rectangular boxes was implemented, each centered on the positions of the unit cell obtained in the previous reconstruction (see Figure 4.3(b)). The individual support boxes are of a significantly larger size than the reconstructed structures. By improving the noise statistics and reducing the symmetry in real space the reconstruction improved to a level at which the smallest features present in the sample were resolved (see Figure 4.3(d))). The reconstruction was performed by applying 2000 iterations of HIO with the mentioned fixed support.

Figure 4.3(d) shows the 2D finite crystal structure reconstructed from a single pulse train of the FEL beam. From line scans taken at the edge of a large hole in Figure 4.3(d) the variation in intensity, from 10% to 90% of its maximum value, occurs over less than four real space pixels (59.6 nm size), which yields a resolution of better than 238 nm. This compares favorably with the measured maximum momentum transfer, that corresponds to 220 nm resolution (see Figure 4.2), where clearly defined features at the edge of the measured diffraction data can be seen. This shows the potential of SAB CDI to reveal the inner structure using FELs.

4.2 Pump- Probe Experiment on Colloidal Crystals at FLASH [DGY+12]

In order to demonstrate the outstanding possibilities of the ultra short intense FEL pulses, in this section, an experiment performed at FLASH using a thin colloidal crystals is discussed. The crystal was excited by a strong infrared (IR) laser pulse and the dynamics in the crystal were analyzed on a picosecond time scale. Colloidal crystals are a new, functional material and posses novel optical and acoustic properties. Artificial hypersonic phononic crystals are a new generation of acousto-optical devices that can be used for the ultrafast manipulation and control of electromagnetic waves by hypersonic (GHz) acoustic waves [GUM+05]. Colloidal crystals, formed by self-assembly of polystyrene and silica nanospheres, have also shown phononic band gaps in the GHz frequency range, which corresponds to the picosecond time scale [CWJ+06, SCR+08, TGM06, ATP+08, SSY+10]. Probing these ultrafast dynamics of colloidal crystals has attracted a large interest in the recent past. There are several techniques that measure vibrations excited by light waves in nanosized colloidal crystals, such as Brillouin light scattering [CWJ+06, ATP+08], Raman scattering [DBC86], and optical pump-probe spectroscopy [TGM06, SSY+10, MSS+07]. Two- and three-dimensional, static structural information of colloidal crystals can be obtained with high spatial resolution at third generation synchrotron sources, using advanced X-ray imaging techniques [GYM+10, BSNS10, GYM+12]. At the same time, the newly developed FELs are especially well-suited for time-resolved experiments on ultrafast structural dynamics of different materials [Bar10], including colloids. FELs provide coherent femtosecond X-ray pulses with extremely high power, which are needed to perform time-resolved experiments with a time resolution that outperforms that of third generation synchrotron sources by several orders of magnitude.

Here, a time-resolved pump-probe diffraction experiment is proposed to investigate ultrafast structural dynamics of colloidal crystals with picosecond time resolution. In this experiment the temporal changes in the sample were induced by short and intense IR laser pulses. The dynamics are encoded in the changes of the diffraction patterns at different time delays. Contrary to the pump-probe experiments with visible light the high penetration depth of XUV pulses for this material allows the probing of relatively thick samples. This experiment is unique in a way since the recorded diffraction patterns were composed of several orders of Bragg peaks and, additionally, the diffuse scattering between them. This opens the possibility of simultaneously extracting the time-dependent variations of the sample in different spatial directions and provides unique information about the dynamics in colloidal samples. In the analysis the temporal changes of the positions of the Bragg peaks and their size were determined. The frequency components of those parameters were calculated using a Fourier analysis.

4.2.1 Experiment

The experiment was conducted at the BL3 beamline at FLASH at a fundamental wavelength of 8 nm. FLASH was operated producing single FEL pulses with an average

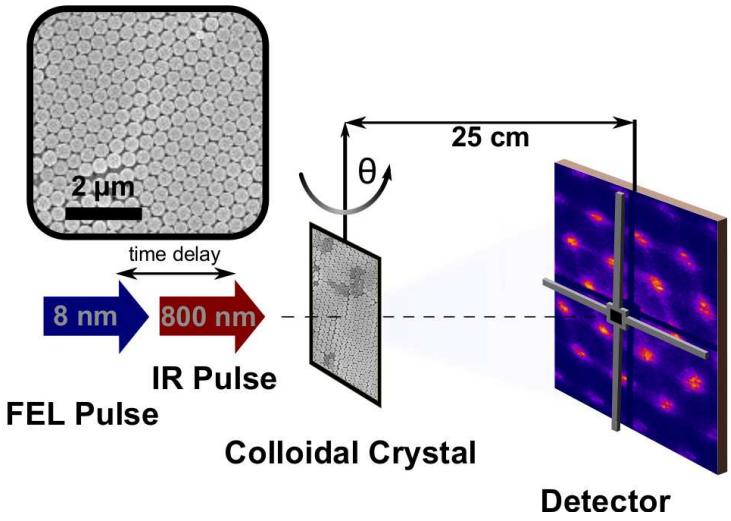

Figure 4.4: Schematic view of the pump-probe experiment showing the IR pump pulse and the XUV probe pulse separated by a time delay Δt, the sample, and the detector, which is protected by a beamstop. The inset shows an SEM image of the colloidal crystal film used in the experiment.

energy of 170 μJ per pulse at a repetition rate of 10 Hz. The last mirror of the beamline was an ellipsoidal mirror which provides an image of the source. Using a laser-induced ablation of poly-methyl methacrylate (PMMA) films [Liu82, CJK$^+$07] the beam size was estimated to be in the sample plane about 12 μm by 40 μm (FWHM) in the horizontal and vertical directions, respectively.

The diffraction data were measured in the dedicated HORST vacuum chamber [Sta09] which was connected to the BL3 beamline. The chamber contains a sample stage which allows rotation of the sample around the vertical axis, an in-vacuum detector, and an optical microscope for sample alignment. The sample position was 70 m downstream from the source. Different absorbers were used to attenuate the intense beam, since the experiment has to be performed in the non-destructive regime, where the sample can withstand several shots without detectable damage. By inserting a 300 nm thick aluminum foil in the beam the intensity of the beam was reduced to $(2.3 \pm 0.7) \times 10^9$ photons per pulse. The diffracted radiation propagates 174 mm from the sample to the detector plane (see Figure 4.4), where an in-vacuum charge-coupled device (CCD) recorded the data. As detector an Andor DODX436-BN with 2048×2048 pixels, each with a 16-bit digitization and a pixel size of $13.5 \times 13.5 \mu m^2$, was used. A cross-shaped beamstop was positioned in front of the CCD to protect the camera from the direct beam (see Figure 4.4).

In addition to the XUV radiation from FLASH IR laser pulses were used to excite the sample. The pump pulses were generated by a Ti:sapphire laser system [RASA$^+$11], operating at 800 nm with a pulse duration of about $\leq$100 fs and a pulse energy of 400

μJ, focused to a spot size of about $200 \times 200\mu m^2$ in the sample plane. The IR laser pulses were co-propagating along the XUV pulses (see Figure 4.4) and synchronized to the pulses from FLASH within a $\leq$500 fs FWHM jitter. The arrival time of the pulses, with respect to each other (the time delay Δt), can be varied with an accuracy better than 500 fs. A time series of diffraction patterns was measured with time delays from -100 to 1000 ps, with 100 ps and 50 ps time intervals. For each time delay ten diffraction patterns were measured to increase the statistics and to neglect other fluctuations in the measurement. The zero time offset was known with an accuracy of about 50 ps due to synchronisation of the laser system with the FEL.

The pump-probe experiments were performed on a colloidal crystal film. The sample consisted of a Si wafer with an array of $250 \times 250\mu m^2$ sized windows, which are sufficiently larger than the FLASH beam. The wafer was covered by a 100 nm thick Si_3N_4 membrane and coated with the thin colloidal crystal. The crystal was grown from 398 nm 2.8% polystryrene microspheres. The polystyrene spheres were synthesized by emulsifier-free emulsion polymerization of styrene, using potassium persulfate as an initiator [GHHO74]. The colloidal crystals were grown by the vertical deposition technique [JBHC99, HAS$^+$09], therefore the wafer was immersed in a suspension of spheres in ethanol (p.a.), with a volume fraction of 0.1 v% in a temperature-controlled room at 20°C. The crystal consisted of about 11 layers, which was determined with an SEM on a crack of the sample.

The initial orientation of the sample ($\theta = 0°$) corresponds to a direction of the incident IR and XUV pulses along the [111] direction of the FCC colloidal crystal, which is perpendicular to the sample surface. Figure 4.5(a) shows a typical single-shot diffraction pattern measured in this geometry after background subtraction. The background signal of the pump laser was removed by averaging over ten images, recorded without the probe laser, and subtracting the result from all diffraction patterns. Several orders of the Bragg peaks are seen on a single-shot diffraction pattern, as shown in Figure 4.5(a,b). The three strongest sets of reflections, which were used in further analysis, are marked. They reflect the periodicity within the close-packed layering of the colloidal spheres. The shape of each Bragg peak is broadened in both vertical and horizontal directions due to defects in the crystal structure as discussed in section 1.3.3. The speckles around and between the peaks are well resolved due to coherent illumination of the sample. In addition, a diffuse scattering around and between the Bragg peaks can be seen.

The measurements were also performed at $\theta = 35°$ incident angle, where another set of Bragg peaks could be accessed (see Figure 4.5(b)). In this orientation the FEL radiation is parallel to the [110] crystallographic FCC direction. The experiment in this geometry was sensitive to the changes in the sample, which are perpendicular to the surface of the colloidal crystal film.

4.2.2 Results and Discussion

When the energy of the pump pulse is transferred to the crystal changes in the crystal lattice affect the position, the intensity, and the shape of the Bragg peaks [BZWE06]. To reveal the characteristic time scales on which structural changes occur in the colloidal

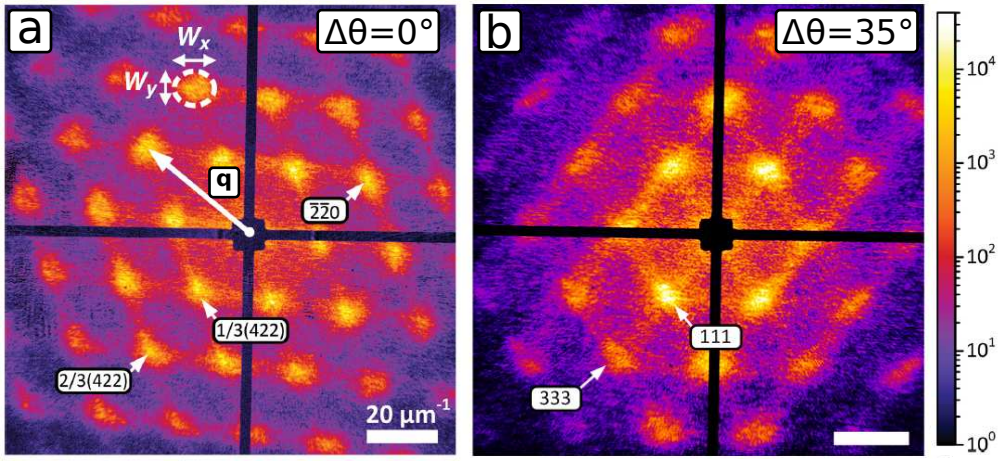

Figure 4.5: (a) Selected single-shot diffraction pattern on a logarithmic scale measured in transmission geometry at azimuthal angle orientation $\Delta\theta = 0°$. The family of FCC peaks $(\bar{2}\bar{2}0)$ and forbidden FCC peaks (1/3(422) and 2/3(422)) are indicated. The momentum transfer vector $\mathbf{q}$ and the horizontal W_x and vertical W_y size of the peaks are shown. (b) Shows a diffraction pattern measured at the azimuthal angle of $\Delta\theta = 35°$.

crystal during the measurement each single-shot diffraction pattern was analyzed in the following way. First, due to a readout error in the CCD detector most images had to be corrected by an offset of an arbitrary number of pixels. To adjust for this shift a distinct region, namely some dead pixels, were directly correlated between two data sets. An automated routine found more than 80 % of the correlations and checked the result by correlating another distinct region on the detector. The remaining data sets had to be corrected manually. It should be noted that this correction had an accuracy of merely 3±2 pixels. After the offset correction the data sets were cropped from the original 2048×2048 pixels to 1900×1900 pixels to avoid other artifacts on the edges of the detector.

Before the detailed analysis of the peaks the correct whitefield image had to be subtracted from the diffraction patterns. The sample was completely removed to measure the background scattering of all other sources. The subtraction then yielded the scattering from the sample only. It should be noted that even the individual dark images had a problem with the offset, which was corrected before averaging 20 background images into one, which was subtracted from the diffraction patterns. In addition, a correction for the readout noise and a possible dark current has to be taken into account. In total 100 dark images were averaged, this average has to be subtracted from all data sets as well, and was therefore included in the whitefield image.

To analyse the peaks in detail, first, the approximate position of all Bragg peaks has to be determined. The routine displays one diffraction pattern, on which a certain number of peaks can be manually identified. It can be assumed that all peaks appear

approximately at the same position. The manually found peak positions are used to locally find the maximum of the peak. This is done by a convolution with a 31 pixel wide circle to blur the fine features, which leaves a smooth peak. Now the maximum can easily be found. The center of the diffraction pattern is defined as the middle position of two opposite peaks. By analysing several pairs of peaks up to nine middle positions are determined, from which the average central position is obtained. The distance between the determined center of the diffraction pattern and the peak position is the momentum transfer and corresponds to a certain spacing in the lattice. Therefore, a time-depended change in the lattice spacing in a certain direction will be reflected by a change in the position of the corresponding Bragg peak.

At the next step, for each Bragg peak position the algorithm fits a 2D Gaussian function, which provides additional information like the FWHM of the peak. The time-dependent broadening of the Bragg peaks corresponds to an inhomogeneous disorder (see section 1.3.3) in the crystal lattice, induced by the pump laser. The integrated intensity within a 81×81 pixel region around the peak is calculated as well as the ratio between the center of the peak and a region around the peak. In order to calculate this ratio the integrated intensity within a 25 pixel wide ring is compared to the intensity in the center region of the Bragg peak. In addition, the integrated intensity in the center of Bragg peak is compared to the intensity in a region around the middle between two Bragg peaks. Changes in the relative peak intensity correspond to modulations of the crystal lattice spacing.

For each time delay all parameters described above were averaged over ten diffraction patterns and their standard deviations were calculated. As an example, in Figure 4.6 the time-dependence of the peak to center distance, the horizontal, and the vertical size of the marked peak (see Figure 4.5(a)) are presented. To estimate the characteristic frequencies probed in the experiment the Fourier transforms of all time-dependent parameters were calculated. The corresponding power spectrum with error bars is shown in the insets of Figure 4.6 in red. Finally, the calculated power spectra of experimental data were averaged over all Bragg peaks from the same family, which all appear at the same $\mathbf{q}$ value. As a result, the insets of Figure 4.6 show the averaged frequency components of the momentum transfer values as well as the horizontal and vertical peak sizes, which are presented with their standard deviations. These results demonstrate an increased contribution of the Fourier components in the frequency region of 4-5 GHz, this can be backed up theoretically [DGY+12] and contributed to beating modes of the colloidal spheres. These enhanced frequencies were not seen as prominent for other peaks, which also demonstrates the directional sensitivity of the experiment for probing dynamics in the crystal in different directions. The diffraction patterns from the measurement at $\theta = 35^\circ$ showed similar behaviour. Due to the rotation the footprint of the IR laser beam is larger on the sample, and the induced dynamics are much weaker. The weak changes in the Bragg peaks observed before were less pronounced and the corresponding power spectra have no characteristic frequencies.

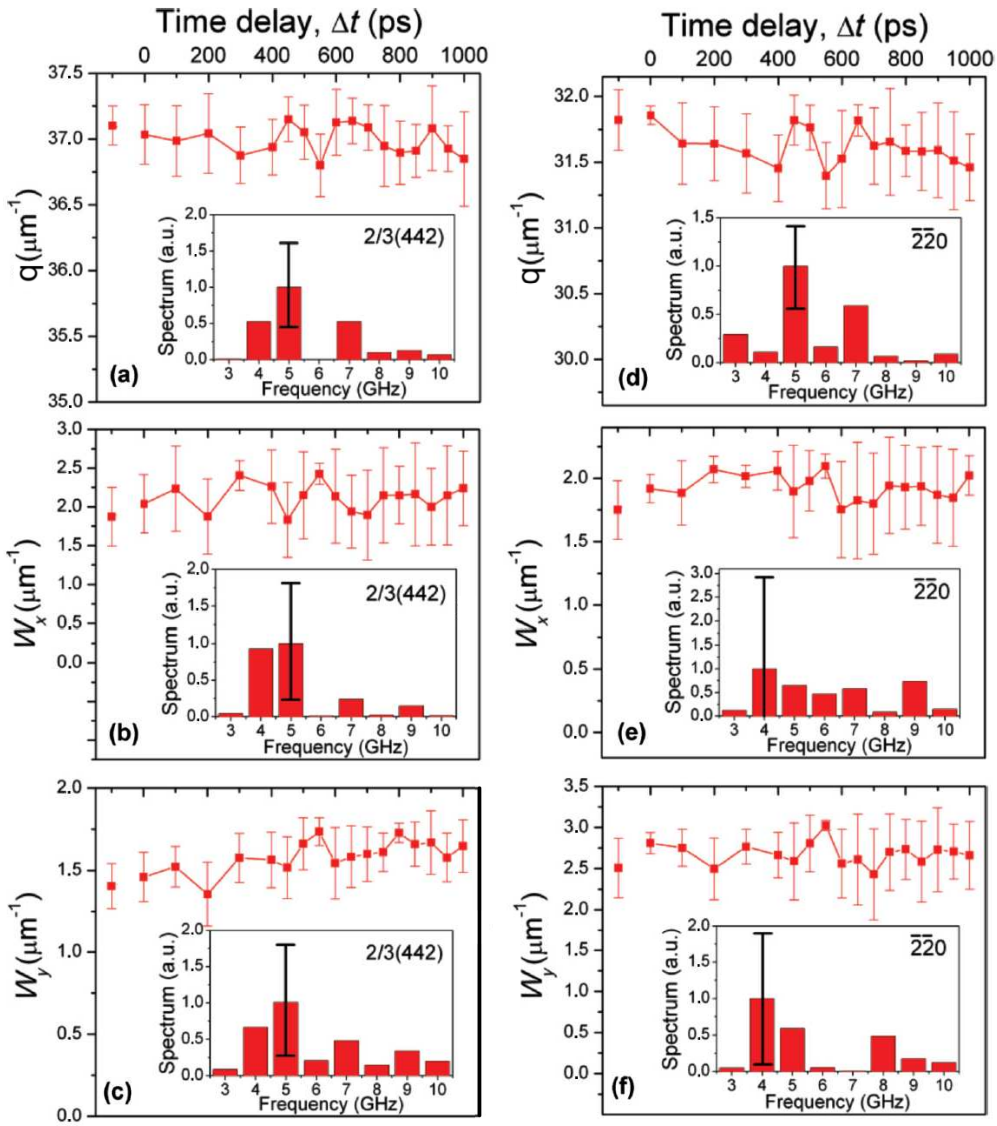

Figure 4.6: Time dependence of the momentum transfer **q** (a) and (d), horizontal W_x (b) and (e), and vertical W_y (c) and (f) size (FWHM) for the selected Bragg peaks 2/3(422) (a)-(c), and $\overline{2}\overline{2}0$ (d)-(e), indicated in Figure 4.5(a). The error bars are determined as a standard deviation for ten measurements. The insets show the power spectrum of the corresponding data.

4.3 Summary and Outlook

In summary, it was demonstrated in this chapter that single pulse train coherent diffractive imaging for a synthetic finite crystalline sample with the reconstructed image exhibiting resolution commensurate with the maximum momentum transfer measured in the diffraction data. Furthermore, it was demonstrated that the traditional noncrystalline framework of CXDI is applicable to two-dimensional finite crystals. In this experiment the 2D crystalline structure has been essential in providing the necessary signal to determine the structure of the unit cells. If only a single unit cell was used simulations suggest that a successful reconstruction to the resolution shown here would be impossible. These findings improve the scope of the fast growing CXDI technique by including finite 2D crystalline specimens in the sphere of applicability of CXDI and by utilizing these crystals to improve the signal to noise ratio, and hence, the resolution of reconstructed images. It can be concluded that this alternative approach to single molecule imaging is a significant step towards revealing the structure of proteins with subnanometer resolution at newly built XFEL sources.

These sources are also perfectly suited for time-dependet measurements of ultrafast dynamics. A pilot experiment on a colloidal crystal was demonstrated. Dynamics were induced in the crystal by short IR laser pulses and the sample was probed by FEL radiation while changing the time delay between the lasers in the picosecond range. The studies were carried out in a non-destructive regime at different rotation angles of the sample. The changes in the colloidal crystal induced by the IR laser were investigated by the analysis of Bragg peaks extracted from the diffraction patterns. The dynamics at different time scales were studied through a Fourier analysis of selected parameters which are associated with different changes in the crystal lattice. Indications for oscillations in the colloidal crystals were found to be in a frequency range of about 4-5 GHz. The demonstrated pump-probe experiment, combined with CDI, has the potential to visualize ultrafast dynamics in colloidal crystals with nanometer spatial resolution at femtosecond time scales.

5 Summary

After a theoretical introduction, in which the fundamental concepts of coherence and scattering were introduced, it was shown that the scattered intensities for a small sample at high energies from coherent X-rays are directly connected with the Fourier transform of the shape function of the sample. The shape function is related to the electron density of the sample, which is the desired information about the sample. For crystalline samples the shape information is encoded in the scattering signal around each Bragg peak, assuming that the sample is coherently illuminated. Different methods of coherent X-ray imaging were introduced, among them Small Angle CDI and Bragg CDI, as well as the basic idea of iterative phase retrieval algorithms. As a combination of Small Angle CDI and Bragg CDI the method of SAB CDI was developed in this thesis. This new method uses the coherent scattering signal around each Bragg peak and the coherent interference signal between the peaks, while measuring several Bragg peaks simultaneously. It was shown in chapter two in simulations that it is possible to reconstruct the individual atom positions within a Pd nano crystal. The necessary conditions to reach this goal are small samples, high energies, and the possibility to measure several Bragg peaks simultaneously with the coherent interference pattern between the peaks.

In the following chapter experiments performed at synchrotron sources were presented. Here, the concept of SAB CDI was proven on colloidal crystalline samples. The first experiment was carried out at ID06 at the ESRF, where a thin colloidal crystal film was illuminated, using a round aperture. The recorded diffraction patterns were inverted and the crystalline structure of the sample was recovered. At a different orientation of the sample the diffraction pattern changed significantly and streaks associated with defects in crystals were measured. The inversion of these diffraction patterns revealed a defect in the form of a stacking fault. For the first time the positions of the individual scatterers around a defect in a crystal were visualized with the help of a direct method.

The following section presented an experiment, which expands this idea to the third dimension. For a small grain of a colloidal crystal diffraction patterns containing several Bragg peaks and a rich speckle pattern were measured for different angles of sample rotation. The diffraction patterns were combined in three- dimensional reciprocal space, containing all information about the inner structure of the grain. Evaluating the analysis of the scattered intensities in 3D several statements about the structure can be made. Clearly, a crystalline structure is present, represented by the strong Bragg peaks, revealing the FCC structure of the self assembled colloids. In addition, streaks were observed, which are attributed to a plane defect in the colloidal crystal grain. Model simulations show that this behaviour can, indeed, be recreated by a stacking fault in the grain. The simulated reciprocal space data was used for a reconstruction and the internal structure of the model was revealed, assuming the same experimental conditions. The knowledge

and experience gained in the performed experiments will lead to future experiments, likely resulting in a measured 3D diffraction pattern, which can be inverted to reveal the inner structure of a colloidal crystal grain.

To show the potential of coherent X-ray scattering applied to a variety of samples an experiment at ID13 at the ESRF was performed on GaAs nanowires. Here, the nano focusing setup was used to illuminate an isolated nanowire. The diffraction patterns were recorded around a Bragg peak and by rotating the sample the 3D structure around a Bragg peak was measured. The volume around the Bragg peak showed a complex pattern, consisting of several crystal truncation rods. The analysis showed that from the orientation of the rods predictions about the shape of the nano wire can be made. With the newly introduced method of SAB CDI the complex internal structure of such nano wires can potentially be reconstructed. This knowledge is important for a better understanding of the complicated growth process of these structures. Here, the technical difficulties for future experiments are rather considerable and further experimental developments are necessary.

The fourth chapter focused on experiments carried out at the FLASH facility at DESY in Hamburg. The special properties of this source make the experiments even more challenging, but also enable measurements in a totally new regime. Due to the ultra short and ultra bright pulses time resolved measurements can be done with a much better time resolution than at any other source relevant for X-ray structure determination. It is, however, not directly inferable that the same methods can be applied and new measurement schemes have to be tested. To this end, a proof of principle experiment was performed, using an artificial 2D crystal. It was shown that the diffraction pattern recorded from a single pulse train contains enough information to invert the diffraction pattern, revealing the structure of the sample. The finally achieved resolution was even high enough to resolve a smaller hole, which had a diameter of only 200 nm, showing the potential for 2D crystals and the possibility to measure single shot diffraction patterns with the ultra short pulses from an FEL, which is important in many fields of life science to overcome the limitations imposed by radiation damage.

The other important feature of FEL radiation is the unique short pulse time structure. Only with such short pulses time resolved measurements in the sub-picosecond regime are possible. In a first proof of principle experiment on colloidal crystals the feasibility of pump-probe experiments on such sample systems was demonstrated. IR laser pulses were used to excite a thin film of a colloidal crystal. The VUV pulses from FLASH were used to probe the material after different time delays, thus creating a series, revealing the time-dependet behaviour of the system. From the rich information in the diffraction patterns several features were analyzed and correlated to their origin in the crystal structure. The time resolution was better than 100 ps and through Fourier analysis the strongest periodic movements were determined. This experimental approach has several advantages, e.g. the possibility to measure the interior of the crystal as well as the behaviour in different directions. Due to the non-destructive nature of the experiment the measurement can be repeated with different parameters. This first experiment showed the potential and set the conditions for future pump-probe experiments with colloidal crystals at FLASH.

The results presented in this thesis show the future path of SAB CDI, which clearly has two available options to develop One of them are static samples with the possibility to measure several projections from an isolated sample. This can reveal the inner structure in three dimensions and the positions of all the individual scatterers can be obtained. From this the functionality of a nano structured material can be designed, since the knowledge about the inner structure is essential for the performance of new materials.

The other path available for SAB CDI are time resolved measurements. If single shot diffraction patterns from nano structured samples are measured, containing several Bragg peaks and the coherent interference signal in between, with pump-probe experiments the internal structure can be determined at different time steps after an excitation. With the high degree of coherence and ultra short pulses of the FEL sources this will be possible even in the sub-picosecond regime. In combination with the possibility of SAB CDI to achieve atomic resolution it will be possible to see crystal nucleation and growth with unprecedented precision. In addition, new information might be deduced about the formation and evolution of defects in crystals.

It is, however, still a long way to go and the first experiments in this direction have just been performed. It has been shown that the method works reliably and is suited for future applications. Now it has to be applied to a variety of samples to attract the interest of the condensed matter community.

List of Publications

This thesis is based on the following publications

Chapter 2:

- J. Gulden, O.M. Yefanov, E. Weckert, and I.A. Vartanyants, *Imaging of Nano-Crystals with Atomic Resolution using High Energy Coherent X-rays*, AIP Conference Proceedings **1365**, 42 (2011).

Chapter 3:

- J. Gulden, O. M. Yefanov, A. P. Mancuso, V. V. Abramova, J. Hilhorst, D. Byelov, I. Snigireva, A. Snigirev, A. V. Petukhov, and I. A. Vartanyants, *Coherent X-ray imaging of defects in colloidal crystals*, Physical Review B **81**, 224105 (2010).
- J. Gulden, O.M. Yefanov, A.P. Mancuso, R. Dronyak, A. Singer, V. Bernátová, A. Burkhardt, O. Polozhentsev, A. Soldatov, M. Sprung, and I.A. Vartanyants, *Three-dimensional structure of a single colloidal crystal grain studied by coherent X-ray diffraction*, Optics Express, (2012).
- J. Gulden, S.O. Mariager, A.P. Mancuso, O.M. Yefanov, J. Baltser, P. Krogstrup, J. Patommel, M. Burghammer, R. Feidenhans'l, and I.A. Vartanyants, *Coherent X-ray nano diffraction on single GaAs nanowires*, physica status solidi (a), **208**, 11, 2495-2498 (2011). (Cover)

Chapter 4:

- A. P. Mancuso, A. Schropp, B. Reime, L.-M. Stadler, A. Singer, J. Gulden, S. Streit-Nierobisch, C. Gutt, G. Grübel, J. Feldhaus, F. Staier, R. Barth, A. Rosenhahn, M. Grunze, T. Nisius, T. Wilhein, D. Stickler, H. Stillrich, R. Frömter, H.-P. Oepen, M. Martins, B. Pfau, C. M. Günther, R. Könnecke, S. Eisebitt, B. Faatz, N. Guerassimova, K. Honkavaara, V. Kocharyan, R. Treusch, E. Saldin, S. Schreiber, E. A. Schneidmiller, M.V. Yurkov, E. Weckert, and I. A. Vartanyants, *Coherent-Pulse 2D Crystallography Using a Free-Electron Laser X-ray Source*, Physical Review Letters **102**, 035502 (2009).
- R. Dronyak, J. Gulden, O. M. Yefanov, A. Singer, T. Gorniak, T. Senkbeil, J.-M. Meijer, A. Al-Shemmary, J. Hallmann, D. D. Mai, T. Reusch, D. Dzhigaev, R. P. Kurta, U. Lorenz, A. V. Petukhov, S. Duesterer, R. Treusch, M. N. Strikhanov, E. Weckert, A. P. Mancuso, T. Salditt, A. Rosenhahn, I. A. Vartanyants, *Dynamics of colloidal crystals studied by pump-probe experiments at FLASH*, Physical Review B **86**, 064303 (2012).

Other Publications by the author

- J. Gulden, O. M. Yefanov, A. P. Mancuso, V. V. Abramova, J. Hilhorst, D. Byelov, I. Snigireva, A. Snigirev, A. V. Petukhov, I. A. Vartanyants, *Imaging defects with coherent X-rays*, Highlights in the DESY Photon Science Report 2010.

- C. Gutt, L.-M. Stadler, S. Streit-Nierobisch, A.P. Mancuso, A. Schropp, B. Pfau, C.M. Günther, R. Könnecke, J. Gulden, B. Reime, J. Feldhaus, E. Weckert, I.A. Vartaniants, O. Hellwig, F. Staier, R. Barth, M. Grunze, A. Rosenhahn, D. Stickler, H. Stillrich, R. Frömter, H.P. Oepen, M. Martins, T. Nisius, T. Wilhein, B. Faatz, N. Guerassimova, K. Honkavaara, V. Kocharyan, R. Treusch, E. Saldin, S. Schreiber, E.A. Schneidmiller, M.V.Yurkov, S. Eisebitt, G. Grübel, *Resonant magnetic scattering with soft X-ray pulses from a free electron laser at 1.59 nm* Physical Review B **79**, 212406 (2009).

- A. Rosenhahn, F. Staier, T. Nisius, D. Schäfer, R. Barth, C. Christophis, L.-M. Stadler, S. Streit-Nierobisch, C. Gutt, A.P. Mancuso, A. Schropp, J. Gulden, B. Reime, J. Feldhaus, E. Weckert, B. Pfau, C. M. Günther, R. Könnecke, S. Eisebitt, M. Martins, B. Faatz, N. Guerassimova, K. Honkavaara, R. Treusch, E. Saldin, S. Schreiber, E. A. Schneidmiller, M. V. Yurkov, I.A. Vartanyants, G. Grübel, M. Grunze, and T. Wilhein, *Digital In-line Holography with femtosecond VUV radiation provided by the free-electron laser FLASH* Optics Express, **17**, 10, 8220-8228 (2009).

- A. P. Mancuso, Th. Gorniak, F. Staier, O. M. Yefanov, R. Barth, C. Christophis, B. Reime, J. Gulden, A. Singer, M. E. Pettit, Th. Nisius, Th. Wilhein, C. Gutt, G. Grübel, N. Guerassimova, R. Treusch, J. Feldhaus, S. Eisebitt, E. Weckert, M. Grunze, A. Rosenhahn, and I. A. Vartanyants, *Coherent imaging of biological samples with femtosecond pulses at the free-electron laser FLASH*, New Journal of Physics, **12**, 035003 (2010).

- A. Schropp, P. Boye, J. M. Feldkamp, R. Hoppe, J. Patommel, D. Samberg, S. Stephan, K. Giewekemeyer, R. N. Wilke, T. Salditt, J. Gulden, A. P. Mancuso, I. A. Vartanyants, E. Weckert, S. Schöder, M. Burghammer, and C. G. Schroer, *Hard X-ray nanobeam characterization by coherent diffraction microscopy* Applied Physics Letters **96**, 091102 (2010).

- I. A. Vartanyants, A. P. Mancuso, A. Singer, O. M. Yefanov, and J. Gulden, *Coherence measurements and coherent diffractive imaging at FLASH*, Journal of Physics B: Atomic, Molecular and Optical Physics, **43**, 194016, (2010).

- A. Singer, F. Sorgenfrei, A. P. Mancuso, N. Gerasimova, O. M. Yefanov, J. Gulden, T. Gorniak, T. Senkbeil, A. Sakdinawat, Y. Liu, D. Attwood, S. Dziarzhytski, D. D. Mai, R. Treusch, E. Weckert, T. Salditt, A. Rosenhahn, W. Wurth, and I. A. Vartanyants, *Spatial and temporal coherence properties of single free-electron laser pulses*, Optics Express, **20**, 17480-17495 (2012).

Bibliography

[AAA+07] W. Ackermann, G. Asova, V. Ayvazyan, A. Azima, N. Baboi, J. Bähr, V. Balandin, B. Beutner, A. Brandt, A. Bolzmann, R. Brinkmann, O. I. Brovko, M. Castellano, P. Castro, L. Catani, E. Chiadroni, S. Choroba, A. Cianchi, J. T. Costello, D. Cubaynes, J. Dardis, W. Decking, H. Delsim-Hashemi, A. Delserieys, G. Di Pirro, M. Dohlus, S. Düsterer, A. Eckhardt, H. T. Edwards, B. Faatz, J. Feldhaus, K. Flöttmann, J. Frisch, L. Fröhlich, T. Garvey, U. Gensch, Ch, M. Görler, N. Golubeva, H. J. Grabosch, M. Grecki, O. Grimm, K. Hacker, U. Hahn, J. H. Han, K. Honkavaara, T. Hott, M. Hüning, Y. Ivanisenko, E. Jaeschke, W. Jalmuzna, T. Jezynski, R. Kammering, V. Katalev, K. Kavanagh, E. T. Kennedy, S. Khodyachykh, K. Klose, V. Kocharyan, M. Körfer, M. Kollewe, W. Koprek, S. Korepanov, D. Kostin, M. Krassilnikov, G. Kube, M. Kuhlmann, C. L. S. Lewis, L. Lilje, T. Limberg, D. Lipka, F. Löhl, H. Luna, M. Luong, M. Martins, M. Meyer, P. Michelato, V. Miltchev, W. D. Möller, L. Monaco, W. F. O. Müller, O. Napieralski, O. Napoly, P. Nicolosi, D. Nölle, T. Nuñez, A. Oppelt, C. Pagani, R. Paparella, N. Pchalek, J. Pedregosa-Gutierrez, B. Petersen, B. Petrosyan, G. Petrosyan, L. Petrosyan, J. Pflüger, E. Plönjes, L. Poletto, K. Pozniak, E. Prat, D. Proch, P. Pucyk, P. Radcliffe, H. Redlin, K. Rehlich, M. Richter, M. Roehrs, J. Roensch, R. Romaniuk, M. Ross, J. Rossbach, V. Rybnikov, M. Sachwitz, E. L. Saldin, W. Sandner, H. Schlarb, B. Schmidt, M. Schmitz, P. Schmüser, J. R. Schneider, E. A. Schneidmiller, S. Schnepp, S. Schreiber, M. Seidel, D. Sertore, A. V. Shabunov, C. Simon, S. Simrock, E. Sombrowski, A. A. Sorokin, P. Spanknebel, R. Spesyvtsev, L. Staykov, B. Steffen, F. Stephan, F. Stulle, H. Thom, K. Tiedtke, M. Tischer, S. Toleikis, R. Treusch, D. Trines, I. Tsakov, E. Vogel, T. Weiland, H. Weise, M. Wellhöfer, M. Wendt, I. Will, A. Winter, K. Wittenburg, W. Wurth, P. Yeates, M. V. Yurkov, I. Zagorodnov, and K. Zapfe. Operation of a free-electron laser from the extreme ultraviolet to the water window. *Nat Photon*, 1(6):336–342, June 2007.

[AAF+86] A. M. Afanas'ev, P. A. Aleksandrov, S. S. Fanchenko, V. A. Chaplanov, and S. S. Yakimov. Asymptotic Bragg diffraction. Single-crystal surface-adjoining-layer structure analysis. *Acta Crystallographica Section A*, 42(2):116–122, March 1986.

[Ae06] M. Altarelli and et.al. Technical design report desy, xfel the european x-ray free-electron laser. Technical report, XFEL, DESY, 2006.

[AF01] S. Auer and D. Frenkel. Prediction of absolute crystal-nucleation rate in hard-sphere colloids. *Nature*, 409(6823):1020–1023, February 2001.

[AHP+08] J.E. Allen, E.R. Hemesath, D.E. Perea, J.L. Lensch-Falk, Z.Y. Li, F. Yin, M.H. Gass, P. Wang, A.L. Bleloch, R.E. Palmer, and L.J. Lauhon. High-resolution detection of au catalyst atoms in si nanowires. *Nat Nano*, 3(3):168–173, March 2008.

[AJS+07] M. Aagesen, E. Johnson, C.B. Sorensen, S.O. Mariager, R. Feidenhans'l, E. Spiecker, J. Nygard, and P.E. Lindelof. Molecular beam epitaxy growth of free-standing plane-parallel inas nanoplates. *Nat Nano*, 2(12):761–764, December 2007.

[AM76] N. W. Ashcroft and N.D. Mermin. *Solid State Physics*. Cengage Learning Services, 1976.

[ANM01] J. Als-Nielsen and D. Mc Morrow. *Elements of Modern X-Ray Physics*. Wiley & Sons, 2001.

[ART+00] R. M. Amos, J. G. Rarity, P. R. Tapster, T. J. Shepherd, and S. C. Kitson. Fabrication of large-area face-centered-cubic hard-sphere colloidal crystals by shear alignment. *Phys. Rev. E*, 61(3):2929–2935, March 2000.

[ATP+08] A. V. Akimov, Y. Tanaka, A. B. Pevtsov, S. F. Kaplan, V. G. Golubev, S. Tamura, D. R. Yakovlev, and M. Bayer. Hypersonic modulation of light in three-dimensional photonic and phononic band-gap materials. *Phys. Rev. Lett.*, 101:033902, July 2008.

[Aut01] A. Authier. *Dynamical theory of x-ray diffraction*. Oxford University Press, 2001.

[Ban08] J. Banhart, editor. *Advanced Tomographic Methods in Materials Research and Engineering*. Oxford University Press, 2008.

[Bar10] A. Barty. Time-resolved imaging using x-ray free electron lasers. *Journal of Physics B: Atomic, Molecular and Optical Physics*, 43(19):194014, 2010.

[Bat82] R. H. T. Bates. Fourier phase problems are uniquely sovable in more than one dimension. i: Underlying theory. *Optik*, 61(3):247–262, 1982.

[BBB+08] A. Barty, S. Boutet, M.J. Bogan, S. Hau-Riege, S. Marchesini, K. Sokolowski-Tinten, N. Stojanovic, R. Tobey, H. Ehrke, A. Cavalleri, S. Dusterer, M. Frank, S. Bajt, B.W. Woods, M.M. Seibert, J. Hajdu, R. Treusch, and H.N. Chapman. Ultrafast single-shot diffraction imaging of nanoscale dynamics. *Nat Photon*, 2(7):415–419, July 2008.

[BBD+04] K. Balewski, W. Brefeld, W. Decking, H. Franz, R. Röhlsberger, and E. Weckert. Petra 3: A low emittance synchrotron radiation source. Technical report, DESY, Hamburg, Germany, February 2004.

[BCG+00] A. Blanco, E. Chomski, S. Grabtchak, M. Ibisate, S. John, S.W. Leonard, C. Lopez, F. Meseguer, H. Miguez, J.P. Mondia, G.A. Ozin, O. Toader, and H.M. van Driel. Large-scale synthesis of a silicon photonic crystal with a complete three-dimensional bandgap near 1.5 micrometres. *Nature*, 405(6785):437–440, 2000.

[BDP+09] A. Biermanns, A. Davydok, H. Paetzelt, A. Diaz, V. Gottschalch, T.H. Metzger, and U. Pietsch. Individual GaAs nanorods imaged by coherent X-ray diffraction. *Journal of Synchrotron Radiation*, 16(6):796–802, November 2009.

[BF07] G. Bortel and G. Faigel. Classification of continuous diffraction patterns: A numerical study. *Journal of Structural Biology*, 158(1):10 – 18, 2007.

[BP08] R. Borsali and R. Pecora. *Soft-Matter Characterization*. Springer reference. Springer, 2008.

[BPN84] R. Bonifacio, C. Pellegrini, and L.M. Narducci. Collective instabilities and high-gain regime in a free electron laser. *Optics Communications*, 50(6):373 – 378, 1984.

[Bro28] R. Brown. A brief account of microscopical observations made in the months of June, July and August, 1827, on the particles contained in the pollen of plants; and on the general existence of active molecules in organic and inorganic bodies. *Phil. Mag.*, 4:161–173, 1828.

[BSNM09] T. Berthing, C.B. Sorensen, J. Nygard, and K.L. Martinez. Applications of nanowire arrays in nanomedicine. *Journal of Nanoneuroscience*, 1(1):3–9, 2009.

[BSNS10] Alexey Bosak, Irina Snigireva, Kirill S. Napolskiia, and Anatoly Snigirev. High resolution transmission microscopy: A new tool for mesoscopic materials. *Adv. Mat.*, 2010.

[BT11] G. Bortel and M. Tegze. Common arc method for diffraction pattern orientation. *Acta Crystallographica Section A*, 67(6):533–543, Nov 2011.

[BW00] M. Born and E. Wolf. *Principles of Optics*. Cambridge University Press, 6 edition, 2000.

[BZWE06] M. Bargheer, N. Zhavoronkov, M. Woerner, and T. Elsaesser. Recent progress in ultrafast x-ray diffraction. *ChemPhysChem*, 7(4):783–792, 2006.

[CBB+06] H.N. Chapman, A. Barty, M.J. Bogan, S. Boutet, M. Frank, S.P. Hau-Riege, S. Marchesini, B.W. Woods, S. Bajt, W.H. Benner, R. A. London, E. Plonjes, M. Kuhlmann, R. Treusch, S. Dusterer, T. Tschentscher, J.R. Schneider, E. Spiller, T. Moller, C. Bostedt, M. Hoener, D.A. Shapiro,

K.O. Hodgson, D. van der Spoel, F. Burmeister, M. Bergh, C. Caleman, G. Huldt, M.M. Seibert, F.R.N.C. Maia, R.W. Lee, A. Szoke, N. Timneanu, and J. Hajdu. Femtosecond diffractive imaging with a soft-x-ray free-electron laser. *Nat Phys*, 2(12):839–843, December 2006.

[CBM+06] H.N. Chapman, A. Barty, S. Marchesini, A. Noy, S.P. Hau-Riege, C. Cui, M.R. Howells, R. Rosen, H. He, J.C.H. Spence, U. Weierstall, T. Beetz, C. Jacobsen, and D. Shapiro. High-resolution ab initio three-dimensional x-ray diffraction microscopy. *J. Opt. Soc. Am. A*, 23(5):1179–1200, May 2006.

[CFB+11] H.N. Chapman, P. Fromme, A. Barty, T.A. White, R.A. Kirian, A. Aquila, M.S. Hunter, J. Schulz, D.P. DePonte, U. Weierstall, R.B. Doak, F.R.N.C. Maia, A.V. Martin, I. Schlichting, L. Lomb, N. Coppola, R.L. Shoeman, S.W. Epp, R. Hartmann, D. Rolles, A. Rudenko, L. Foucar, N. Kimmel, G. Weidenspointner, P. Holl, M. Liang, M. Barthelmess, C. Caleman, S. Boutet, M.J. Bogan, J. Krzywinski, C. Bostedt, S. Bajt, L. Gumprecht, B. Rudek, B. Erk, C. Schmidt, A. Homke, C. Reich, D. Pietschner, L. Struder, G. Hauser, H. Gorke, J. Ullrich, S. Herrmann, G. Schaller, F. Schopper, H. Soltau, K. Kuhnel, M. Messerschmidt, J.D. Bozek, S.P. Hau-Riege, M. Frank, C.Y. Hampton, R.G. Sierra, D. Starodub, G.J. Williams, J. Hajdu, N. Timneanu, M.M. Seibert, J. Andreasson, A. Rocker, O. Jonsson, M. Svenda, S. Stern, K. Nass, R. Andritschke, C. Schroter, F. Krasniqi, M. Bott, K.E. Schmidt, X. Wang, I. Grotjohann, J.M. Holton, T.R.M. Barends, R. Neutze, S. Marchesini, R. Fromme, S. Schorb, D. Rupp, M. Adolph, T. Gorkhover, I. Andersson, H. Hirsemann, G. Potdevin, H. Graafsma, B. Nilsson, and J.C.H. Spence. Femtosecond x-ray protein nanocrystallography. *Nature*, 470(7332):73–77, February 2011.

[CHRB+07] H.N. Chapman, S.P. Hau-Riege, M.J. Bogan, S. Bajt, A. Barty, S. Boutet, S. Marchesini, M. Frank, B.W. Woods, W.H. Benner, R.A. London, U. Rohner, A. Szoke, E. Spiller, T. Moller, C. Bostedt, D.A. Shapiro, M. Kuhlmann, R. Treusch, E. Plonjes, F. Burmeister, M. Bergh, C. Caleman, G. Huldt, M.M. Seibert, and J Hajdu. Femtosecond time-delay x-ray holography. *Nature*, 448(7154):676–679, August 2007.

[CJK+07] J. Chalupský, L. Juha, J. Kuba, J. Cihelka, V. Hájková, S. Koptyaev, J. Krása, A. Velyhan, M. Bergh, C. Caleman, J. Hajdu, R. M. Bionta, H. Chapman, S. P. Hau-Riege, R. A. London, M. Jurek, J. Krzywinski, R. Nietubyc, J. B. Pelka, R. Sobierajski, J. Meyer ter Vehn, A. Tronnier, K. Sokolowski-Tinten, N. Stojanovic, K. Tiedtke, S. Toleikis, T. Tschentscher, H. Wabnitz, and U. Zastrau. Characteristics of focused soft x-ray free-electron laser beam determined by ablation of organic molecular solids. *Opt. Express*, 15(10):6036–6043, May 2007.

[CMWL07] C.C. Chen, J. Miao, C.W. Wang, and T.K. Lee. Application of optimization technique to noncrystalline x-ray diffraction microscopy: Guided hybrid input-output method. *Phys. Rev. B*, 76(6):064113, 2007.

[CN10] H.N. Chapman and K.A. Nugent. Coherent lensless X-ray imaging. *Nature Photonics*, 4(12):833–839, December 2010.

[CPL+08] C.K. Chan, H. Peng, G. Liu, K. McIlwrath, X.F. Zhang, R.A. Huggins, and Y. Cui. High-performance lithium battery anodes using silicon nanowires. *Nat Nano*, 3(1):31–35, January 2008.

[CSC+10] V. Chamard, J. Stangl, G. Carbone, A. Diaz, G. Chen, C. Alfonso, C. Mocuta, and T. H. Metzger. Three-dimensional x-ray fourier transform holography: The bragg case. *Phys. Rev. Lett.*, 104:165501, April 2010.

[CSF+08] C. Colombo, D. Spirkoska, M. Frimmer, G. Abstreiter, and A. Fontcuberta i Morral. Ga-assisted catalyst-free growth mechanism of gaas nanowires by molecular beam epitaxy. *Phys. Rev. B*, 77:155326, April 2008.

[CWJ+06] W. Cheng, J. Wang, U. Jonas, G. Fytas, and N. Stefanou. Observation and tuning of hypersonic bandgaps in colloidal crystals. *Nat Mater*, 5(10):830–836, October 2006.

[DBC86] E. Duval, A. Boukenter, and B. Champagnon. Vibration eigenmodes and size of microcrystallites in glass: Observation by very-low-frequency raman scattering. *Phys. Rev. Lett.*, 56:2052–2055, May 1986.

[DBK+08] M. Dierolf, O. Bunk, S. Kynde, P. Thibault, I Johnson, A. Menzel, K. Jefimovs, C. David, O. Marti, and F. Pfeiffer. Ptychography & lensless x-ray imaging. *Europhysics News*, 39(1):22–24, January 2008.

[DG00] A. Ducruix and R. Giege. *Crystallization of Nucleic Acids and Proteins: A Practical Approach*. The Practical Approach Series. Oxford University Press, USA, 2000.

[DGY+12] R. Dronyak, J. Gulden, O. M. Yefanov, A. Singer, T. Gorniak, T. Senkbeil, J.-M. Meijer, A. Al-Shemmary, J. Hallmann, D. D. Mai, T. Reusch, D. Dzhigaev, R. P. Kurta, U. Lorenz, A. V. Petukhov, S. Düsterer, R. Treusch, M. N. Strikhanov, E. Weckert, A. P. Mancuso, T. Salditt, A. Rosenhahn, and I. A. Vartanyants. Dynamics of colloidal crystals studied by pump-probe experiments at flash. *Phys. Rev. B*, 86:064303, Aug 2012.

[Dic05] E.A.H. Dictionaries. *The American Heritage Science Dictionary*. Houghton Mifflin Harcourt, 2005.

[DLS+09] R. Dronyak, K.S. Liang, Y.P. Stetsko, T.K. Lee, C.K. Feng, J.S. Tsai, and F.R. Chen. Electron diffractive imaging of nano-objects using a guided method with a dynamic support. *Appl. Phys. Lett.*, 95:111908, 2009.

[DMS+09] A. Diaz, C. Mocuta, J. Stangl, B. Mandl, C. David, J. Vila-Comamala, V. Chamard, T. H. Metzger, and G. Bauer. Coherent diffraction imaging of a single epitaxial inas nanowire using a focused x-ray beam. *Phys. Rev. B*, 79:125324, March 2009.

[DMT+10] M. Dierolf, A. Menzel, P. Thibault, P. Schneider, C.M. Kewish, R. Wepf, O. Bunk, and F. Pfeiffer. Ptychographic x-ray computed tomography at the nanoscale. *Nature*, 467(7314):436–439, September 2010.

[DPA+05] I. P. Dolbnya, A. V. Petukhov, D. G. A. L. Aarts, G. J. Vroege, and H. N. W. Lekkerkerker. Coexistence of rhcp and fcc phases in hard-sphere colloidal crystals. *Europhysics Letters*, 72(6):962, 2005.

[DSSS05] M. Drakopoulos, A. Snigirev, I. Snigireva, and J. Schilling. X-ray high-resolution diffraction using refractive lenses. *Applied Physics Letters*, 86(1):014102, 2005.

[Ein05] A. Einstein. Über die von der molekularkinetischen Theorie der Wärme geforderte Bewegung von in ruhenden Flüssigkeiten suspendierten Teilchen. *Annalen der Physik*, 322(8):549–560, 1905.

[ELS+04] S. Eisebitt, J. Luning, W. F. Schlotter, M. Lorgen, O. Hellwig, W. Eberhardt, and J. Stohr. Lensless imaging of magnetic nanostructures by x-ray spectro-holography. *Nature*, 432(7019):885–888, December 2004.

[Ewa40] P. P. Ewald. X-ray diffraction by finite and imperfect crystal lattices. *Proceedings of the Physical Society*, 52(1):167, 1940.

[Fie82] J.R. Fienup. Phase retrieval algorithms: a comparison. *Appl. Opt.*, 21(15):2758–2769, 1982.

[FNEKG09] V. Favre-Nicolin, J. Eymery, R. Koester, and P. Gentile. Coherent-diffraction imaging of single nanowires of diameter 95 nanometers. *Phys. Rev. B*, 79:195401, May 2009.

[FSSO09] R. Fung, V. Shneerson, D. K. Saldin, and A. Ourmazd. Structure from fleeting illumination of faint spinning objects in flight. *Nature Physics*, 5(1):64–67, 2009.

[GHHO74] J. W. Goodwin, J. Hearn, C. C. Ho, and R. H. Ottewill. Studies on the preparation and characterisation of monodisperse polystyrene laticee. *Colloid Polym. Sci.*, 252(6):464–471, 1974.

[Gia02] C. Giacovazzo. *Fundamentals of crystallography*. IUCr texts on crystallography. Oxford University Press, 2002.

[Gla63a] R.J. Glauber. Coherent and incoherent states of the radiation field. *Phys. Rev.*, 131:2766–2788, Sep 1963.

[Gla63b] R.J. Glauber. The quantum theory of optical coherence. *Phys. Rev.*, 130:2529–2539, Jun 1963.

[GMM+11] J. Gulden, S. O. Mariager, A. P. Mancuso, O. M. Yefanov, J. Baltser, P. Krogstrup, J. Patommel, M. Burghammer, R. Feidenhans'l, and I. A. Vartanyants. Coherent x-ray nanodiffraction on single gaas nanowires. *physica status solidi (a)*, 208(11):2495–2498, 2011.

[Goo00] J.W. Goodman. *Statistical optics*. Wiley classics library. Wiley, 2000.

[GS72] R. W. Gerchberg and W. O. Saxton. A practical algorithm for the determination of phase from image and diffraction plane pictures. *Optik*, 35(2):237–246, 1972.

[Gul08] J. Gulden. Coherent x-ray scattering on nano- and micron-scale samples at high energies. Diploma thesis, University of Rostock, 2008.

[GUM+05] T. Gorishnyy, C. K. Ullal, M. Maldovan, G. Fytas, and E. L. Thomas. Hypersonic phononic crystals. *Phys. Rev. Lett.*, 94:115501, March 2005.

[GWS+01] U. Gasser, E.R. Weeks, A. Schofield, P.N. Pusey, and D.A. Weitz. Real-space imaging of nucleation and growth in colloidal crystallization. *Science*, 292(5515):258–262, 2001.

[GYM+10] J. Gulden, O. M. Yefanov, A. P. Mancuso, V. V. Abramova, J. Hilhorst, D. Byelov, I. Snigireva, A. Snigirev, A. V. Petukhov, and I. A. Vartanyants. Coherent x-ray imaging of defects in colloidal crystals. *Phys. Rev. B*, 81:224105, June 2010.

[GYM+12] J. Gulden, O. M. Yefanov, A. P. Mancuso, R. Dronyak, A. Singer, V. Bernátová, A. Burkhardt, O. Polozhentsev, A. Soldatov, M. Sprung, and I. A. Vartanyants. Three-dimensional structure of a single colloidal crystal grain studied by coherent x-ray diffraction. *Opt. Express*, 20(4):4039–4049, February 2012.

[GYWV11] J. Gulden, O. M. Yefanov, E. Weckert, and I. A. Vartanyants. Imaging of nanocrystals with atomic resolution using high-energy coherent x-rays. *AIP Conference Proceedings*, 1365(1):42–45, 2011.

[HAS+09] J. Hilhorst, V.V. Abramova, A. Sinitskii, N.A. Sapoletova, K.S. Napolskii, A.A. Eliseev, D.V. Byelov, N.A. Grigoryeva, A.V. Vasilieva, W.G. Bouwman, K. Kvashnina, A. Snigirev, S.V. Grigoriev, and A.V. Petukhov. Double stacking faults in convectively assembled crystals of colloidal spheres. *Langmuir*, 25(17):10408, May 2009.

[HDVvB02] J.P. Hoogenboom, D. Derks, P. Vergeer, and A. van Blaaderen. Stacking faults in colloidal crystals grown by sedimentation. *The Journal of Chemical Physics*, 117(24):11320–11328, 2002.

[Hil12] J. Hilhorst. *Defects in Colloidal Crystals Identification, Characterization, and Manipulation*. PhD thesis, Universiteit Utrecht, 2012.

[HL82] J.P. Hirth and J. Lothe. *Theory of dislocations*. Krieger Pub. Co., 1982.

[HMS+09] X. Huang, H. Miao, J. Steinbrener, J. Nelson, D. Shapiro, A. Stewart, J. Turner, and C. Jacobsen. Signal-to-noise and radiation exposure considerations in conventional and diffraction x-ray microscopy. *Opt. Express*, 17(16):13541–13553, August 2009.

[HSH03] G. Huldt, A. Szke, and J. Hajdu. Diffraction imaging of single particles and biomolecules. *Journal of Structural Biology*, 144(1-2):219 – 227, 2003.

[HZJ+09] W. J. Huang, J. M. Zuo, B. Jiang, K. W. Kwon, and M. Shim. Sub-angstrom-resolution diffractive imaging of single nanocrystals. *Nat. Phys.*, 5(2):129–133, 2009.

[iMCA+08] A. Fontcuberta i Morral, C. Colombo, G. Abstreiter, J. Arbiol, and J. R. Morante. Nucleation mechanism of gallium-assisted molecular beam epitaxy growth of gallium arsenide nanowires. *Applied Physics Letters*, 92(6):063112, 2008.

[JBHC99] P. Jiang, J. F. Bertone, K. S. Hwang, and V. L. Colvin. Single-crystal colloidal multilayers of controlled thickness. *Chemistry of Materials*, 11(8):2132–2140, 1999.

[JKP+06] J. Johansson, L.S. Karlsson, C. Patrik, T. Svensson, T. Martensson, B.A. Wacaser, K. Deppert, L. Samuelson, and W.r Seifert. Structural properties of [lang]111[rang]b -oriented iii-v nanowires. *Nat Mater*, 5(7):574–580, July 2006.

[JWDS06] J. Johansson, B.A. Wacaser, K.A. Dick, and W. Seifert. Growth related aspects of epitaxial nanowires. *Nanotechnology*, 17(11):355–361, June 2006.

[JWLG+10] H.J. Joyce, J. Wong-Leung, Q. Gao, H.H. Tan, and C. Jagadish. Phase perfection in zinc blende and wurtzite iii-v nanowires using basic growth parameters. *Nano Letters*, 10(3):908–915, 2010.

[KD99] B.O. Kolbesen and Electrochemical Society. Electronics Division. *Analytical and Diagnostic Techniques for Semiconductor Materials, Devices, and Processes: Joint Proceedings of the Symposia On: ALTECH 99 : Satellite Symposium to ESSDERC 99 : Leuven, Belgium : The Electrochemical Society Symposium on Diagnostic Techniques for Semiconductor Materials and Devices*. Number Bd. 3895 in Proceedings (Electrochemical Society). Electrochemical Society, 1999.

[KG10] K. Kelton and A.L. Greer. *Nucleation in Condensed Matter: Applications in Materials and Biology*. Pergamon Materials Series. Elsevier Science, 2010.

[KH50] J. Karle and H. Hauptman. The phases and magnitudes of the structure factors. *Acta Crystallographica*, 3(3):181–187, May 1950.

[Kit06] C. Kittel. *Einführung in die Festkörperphysik*. Oldenbourg Verl., 2006.

[Kni03] J.C. Knight. Photonic crystal fibres. *Nature*, 424(6950):847–851, August 2003.

[KS80] A. M. Kondratenko and E. L. Saldin. Generation of coherent radiation by a relativistic electron beam in an undulator. *Part. Accelerators*, 10:207–216, 1980.

[Kul07] G. N. Kulipanov. Ginzburg's invention of undulators and their role in modern synchrotron radiation sources and free electron lasers. *Physics-Uspekhi*, 50(4):368, 2007.

[KVM+97] Y. Kimura, D.G. Vassylyev, A. Miyazawa, A. Kidera, M. Matsushima, K. Mitsuoka, K. Murata, T. Hirai, and Y. Fujiyoshi. Surface of bacteriorhodopsin revealed by high-resolution electron crystallography. *Nature*, 389(6647):206–211, September 1997.

[KYS+09] P. Krogstrup, J. Yamasaki, C.B. Sørensen, E. Johnson, J.B. Wagner, R. Pennington, M. Aagesen, N. Tanaka, and J. Nygård. Junctions in axial iii-v heterostructure nanowires obtained via an interchange of group iii elements. *Nano Letters*, 9(11):3689–3693, 2009.

[LA94] W. Loose and B. J. Ackerson. Model calculations for the analysis of scattering data from layered structures. *The Journal of Chemical Physics*, 101(9):7211–7220, 1994.

[LBE+10] N. D. Loh, M. J. Bogan, V. Elser, A. Barty, S. Boutet, S. Bajt, J. Hajdu, T. Ekeberg, F. R. N. C. Maia, J. Schulz, M. M. Seibert, B. Iwan, N. Timneanu, S. Marchesini, I. Schlichting, R. L. Shoeman, L. Lomb, M. Frank, M. Liang, and H. N. Chapman. Publisher's note: Cryptotomography: Reconstructing 3d fourier intensities from randomly oriented single-shot diffraction patterns [phys. rev. lett. 104, 225501 (2010)]. *Phys. Rev. Lett.*, 104:239902, Jun 2010.

[LE09] Ne-Te Duane Loh and Veit Elser. Reconstruction algorithm for single-particle diffraction imaging experiments. *Phys. Rev. E*, 80:026705, Aug 2009.

[Liu82] J. M. Liu. Simple technique for measurements of pulsed gaussian-beam spot sizes. *Opt. Lett.*, 7(5):196–198, May 1982.

[LL96] L.D. Landau and E.M. Lifšic. *Statistical physics*. Number Pt. 1. Pergamon, 1996.

[LMN+08] X. Lu, S.G.J. Mochrie, S. Narayanan, A.R. Sandy, and M. Sprung. How a liquid becomes a glass both on cooling and on heating. *Phys. Rev. Lett.*, 100:045701, January 2008.

[Mad71] J.M.J. Madey. Stimulated emission of bremsstrahlung in a periodic magnetic field. *Journal of Applied Physics*, 42(5):1906–1913, 1971.

[Mar07] S. Marchesini. A unified evaluation of iterative projection algorithms for phase retrieval. *Review of Scientific Instruments*, 78:011301, 2007.

[MCKS99] J. Miao, P. Charalambous, J. Kirz, and D. Sayre. Extending the methodology of x-ray crystallography to allow imaging of micrometre-sized noncrystalline specimens. *Nature*, 400(6742):342–344, 1999.

[MGS+10] A. P. Mancuso, Th. Gorniak, F. Staier, O. M. Yefanov, R. Barth, C. Christophis, B. Reime, J. Gulden, A. Singer, M. E. Pettit, Th. Nisius, Th. Wilhein, C. Gutt, G. Grübel, N. Guerassimova, R. Treusch, J. Feldhaus, S. Eisebitt, E. Weckert, M. Grunze, A. Rosenhahn, and I. A. Vartanyants. Coherent imaging of biological samples with femtosecond pulses at the free-electron laser flash. *New Journal of Physics*, 12(3):035003, 2010.

[MHC+03] S. Marchesini, H. He, H. N. Chapman, S. P. Hau-Riege, A. Noy, M. R. Howells, U. Weierstall, and J. C. H. Spence. X-ray image reconstruction from a diffraction pattern alone. *Physical Review B*, 68:140101, 2003.

[MHI+03] J. Miao, K.O. Hodgson, T. Ishikawa, C.A. Larabell, M.A. LeGros, and Y. Nishino. Imaging whole escherichia coli bacteria by using single-particle x-ray diffraction. *Proceedings of the National Academy of Sciences*, 100(1):110–112, 2003.

[MLD+09] S. O. Mariager, S. L. Lauridsen, A. Dohn, N. Bovet, C. B. Sørensen, C. M. Schlepütz, P. R. Willmott, and R. Feidenhans'l. High-resolution three-dimensional reciprocal-space mapping of InAs nanowires. *Journal of Applied Crystallography*, 42(3):369–375, June 2009.

[Mot51] H. Motz. Applications of the radiation from fast electron beams. *Journal of Applied Physics*, 22(5):527–535, 1951.

[MrA+07] S. O. Mariager, C. B. Sørensen, M. Aagesen, J. Nygård, R. Feidenhans'l, and P. R. Willmott. Facet structure of gaas nanowires grown by molecular beam epitaxy. *Applied Physics Letters*, 91(8):083106, 2007.

[MS97] R. P. Millane and W. J. Stroud. Reconstructing symmetric images from their undersampled fourierintensities. *Journal of the Optical Society of America A: Optics, ImageScience, and Vision*, 14(3):568–579, 1997.

[MS00] J. Miao and D. Sayre. On possible extensions of X-ray crystallography through diffraction-pattern oversampling. *Acta Crystallographica Section A*, 56(6):596–605, November 2000.

[MSR+09] A. P. Mancuso, A. Schropp, B. Reime, L.-M. Stadler, A. Singer, J. Gulden, S. Streit-Nierobisch, C. Gutt, G. Grübel, J. Feldhaus, F. Staier, R. Barth, A. Rosenhahn, M. Grunze, T. Nisius, T. Wilhein, D. Stickler, H. Stillrich, R. Frömter, H.-P. Oepen, M. Martins, B. Pfau, C. M. Günther, R. Könnecke, S. Eisebitt, B. Faatz, and N. Guerassimova. Coherent-pulse 2d crystallography using a free-electron laser x-ray source. *Phys. Rev. Lett.*, 102(3):035502, 2009.

[MSS+07] D. A. Mazurenko, X. Shan, J. C. P. Stiefelhagen, C. M. Graf, A. van Blaaderen, and J. I. Dijkhuis. Coherent vibrations of submicron spherical gold shells in a photonic crystal. *Phys. Rev. B*, 75:161102, April 2007.

[MT10] B.W.J. McNeil and N.R. Thompson. X-ray free-electron lasers. *Nat Photon*, 4(12):814–821, Dec 2010.

[MW95] L. Mandel and E. Wolf. *Optical Coherence and Quantum Optics*. Cambridge University Pres, New York, 1995.

[MYV10] A.P. Mancuso, O.M. Yefanov, and I.A. Vartanyants. Coherent diffractive imaging of biological samples at synchrotron and free electron laser facilities. *Journal of Biotechnology*, 149(4):229–237, 2010.

[NAM+04] D. J. Norris, E. G. Arlinghaus, L. Meng, R. Heiny, and L. E. Scriven. Opaline photonic crystals: How does self-assembly work? *Adv. Mat.*, 16(16):1393–1399, 2004.

[NG05] C. Nave and E.F. Garman. Towards an understanding of radiation damage in cryocooled macromolecular crystals. *Journal of Synchrotron Radiation*, 12(3):257–260, May 2005.

[NHR10] S.J. Newton, M.C.and Leake, R. Harder, and I.K. Robinson. Three-dimensional imaging of strain in a single zno nanorod. *Nature Materials*, 9(2):120–124, February 2010.

[NMI03] Y. Nishino, J. Miao, and T. Ishikawa. Image reconstruction of nanostructured nonperiodic objects only from oversampled hard x-ray diffraction intensities. *Phys. Rev. B*, 68:220101, December 2003.

[NSG+09] K.S. Napolskii, N.A. Sapoletova, D.F. Gorozhankin, A.A. Eliseev, D.Y. Chernyshov, D.V. Byelov, N.A. Grigoryeva, A.A. Mistonov, Wim G. Bouwman, K.O. Kvashnina, A.V. Lukashin, A.A. Snigirev, A.V. Vassilieva, S.V. Grigoriev, and A.V. Petukhov. Fabrication of artificial opals by electric-field-assisted vertical deposition. *Langmuir*, 26(4):2346–2351, Oct 2009.

[NSK+08] P. Nolte, A. Stierle, N. Kasper, N. Y. Jin-Phillipp, H. Reichert, A. Ruhm, J. Okasinski, H. Dosch, and S. Schoder. Combinatorial high-energy x-ray microbeam study of the size-dependent oxidation of pd nanoparticles on mgo(100). *Physical Review B (Condensed Matter and Materials Physics)*, 77(11):115444, 2008.

[NWvdS+00] R. Neutze, R. Wouts, D. van der Spoel, E. Weckert, and J. Hajdu. Potential for biomolecular imaging with femtosecond x-ray pulses. *Nature*, 406(6797):752–757, August 2000.

[Ons49] L. Onsager. The effects of shape on the interaction of colloidal particles. *Annals of the New York Academy of Sciences*, 51(4):627–659, 1949.

[PAD+02] A. V. Petukhov, D. G. A. L. Aarts, I. P. Dolbnya, E. H. A. de Hoog, K. Kassapidou, G. J. Vroege, W. Bras, and H. N. W. Lekkerkerker. High-resolution small-angle x-ray diffraction study of long-range order in hard-sphere colloidal crystals. *Phys. Rev. Lett.*, 88:208301, April 2002.

[PAM+06] D.E. Perea, J.E. Allen, S.J. May, B.W. Wessels, D.N. Seidman, and L.J. Lauhon. Three-dimensional nanoscale composition mapping of semiconductor nanowires. *Nano Letters*, 6(2):181–185, 2006.

[Paw06] J.B. Pawley. *Handbook of biological confocal microscopy*. Language of science. Springer, 2006.

[PDA+03] A. V. Petukhov, I. P. Dolbnya, D. G. A. L. Aarts, G. J. Vroege, and H. N. W. Lekkerkerker. Bragg rods and multiple x-ray scattering in random-stacking colloidal crystals. *Phys. Rev. Lett.*, 90(2):028304, 2003.

[PDAV04] A. V. Petukhov, I. P. Dolbnya, D. G. A. L. Aarts, and G. J. Vroege. Destruction of long-range order recorded with *in situ* small-angle x-ray diffraction in drying colloidal crystals. *Phys. Rev. E*, 69:031405, March 2004.

[Per09] J. Perrin. Mouvement brownien et réalité moléculaire. *Annales de Chimie et de Physique*, 18:5–104, 1909.

[Per14] J. Perrin. *Les atomes*. F. Alcan, 1914.

[PLS+99] O. Painter, R. K. Lee, A. Scherer, A. Yariv, J. D. O'Brien, P. D. Dapkus, and I. Kim. Two-dimensional photonic band-gap defect mode laser. *Science*, 284(5421):1819–1821, 1999.

[Poo04] W. Poon. Colloids as big atoms. *Science*, 304(5672):830–831, 2004.

[PvM86] P. N. Pusey and W. van Megen. Phase behaviour of concentrated suspensions of nearly hard colloidal spheres. *Nature*, 320(6060):340–342, March 1986.

[PvMB+89] P. N. Pusey, W. van Megen, P. Bartlett, B. J. Ackerson, J. G. Rarity, and S. M. Underwood. Structure of crystals of hard colloidal spheres. *Phys. Rev. Lett.*, 63(25):2753–2756, 1989.

[PWBD06] F. Pfeiffer, T. Weitkamp, O. Bunk, and C. David. Phase retrieval and differential phase-contrast imaging with low-brilliance X-ray sources. *Nature Physics*, 2(4):258–261, March 2006.

[PWV+06] M.A. Pfeifer, G.J. Williams, I.A. Vartanyants, R. Harder, and I.K. Robinson. Three-dimensional mapping of a deformation field inside a nanocrystal. *Nature*, 442(7098):63–66, July 2006.

[RASA+11] H. Redlin, A. Al-Shemmary, A. Azima, N. Stojanovic, F. Tavella, I. Will, and S. Dsterer. The flash pump-probe laser system: Setup, characterization and optical beamlines. *Nuclear Instruments and Methods in Physics Research Section A: Accelerators, Spectrometers, Detectors and Associated Equipment*, 635(1, Supplement):88 – 93, 2011.

[RF04] J. M. Rodenburg and H. M. L. Faulkner. A phase retrieval algorithm for shifting illumination. *Applied Physics Letters*, 85(20):4795–4797, 2004.

[RHC+07] J. M. Rodenburg, A. C. Hurst, A. G. Cullis, B. R. Dobson, F. Pfeiffer, O. Bunk, C. David, K. Jefimovs, and I. Johnson. Hard-x-ray lensless imaging of extended objects. *Phys. Rev. Lett.*, 98(3):034801, 2007.

[RMRC05] R. Rengarajan, D. Mittleman, C. Rich, and V. Colvin. Effect of disorder on the optical properties of colloidal crystals. *Phys. Rev. E*, 71:016615, January 2005.

[Rob86] I. K. Robinson. Crystal truncation rods and surface roughness. *Phys. Rev. B*, 33(6):3830–3836, March 1986.

[Rus03] P. Russell. Photonic crystal fibers. *Science*, 299(5605):358–362, 2003.

[RVW+01] I.K. Robinson, I.A. Vartanyants, G.J. Williams, M.A. Pfeifer, and J.A. Pitney. Reconstruction of the shapes of gold nanocrystals using coherent x-ray diffraction. *Phys. Rev. Lett.*, 87:195505, 2001.

[SAG+09] D. Spirkoska, J. Arbiol, A. Gustafsson, S. Conesa-Boj, F. Glas, I. Zardo, M. Heigoldt, M. H. Gass, A. L. Bleloch, S. Estrade, M. Kaniber, J. Rossler, F. Peiro, J. R. Morante, G. Abstreiter, L. Samuelson, and A. Fontcuberta i Morral. Structural and optical properties of high quality zinc-blende/wurtzite gaas nanowire heterostructures. *Phys. Rev. B*, 80:245325, December 2009.

[Say52] D. Sayre. Some implications of a theorem due to Shannon. *Acta Crystallographica*, 5(6):843, November 1952.

[SBF+10] A. Schropp, P. Boye, J. M. Feldkamp, R. Hoppe, J. Patommel, D. Samberg, S. Stephan, K. Giewekemeyer, R. N. Wilke, T. Salditt, J. Gulden, A. P. Mancuso, I. A. Vartanyants, E. Weckert, S. Schöder, M. Burghammer, and C. G. Schroer. Hard x-ray nanobeam characterization by coherent diffraction microscopy. *Applied Physics Letters*, 96(9):091102, 2010.

[Sch07] W. Schuelke. *Electron Dynamics by Inelastic X-Ray Scattering*. Oxford Series on Synchrotron Radiation. Oxford University Press, USA, 2007.

[SCR+08] T. Still, W. Cheng, M. Retsch, R. Sainidou, J. Wang, U. Jonas, N. Stefanou, and G. Fytas. Simultaneous occurrence of structure-directed and particle-resonance-induced phononic gaps in colloidal films. *Phys. Rev. Lett.*, 100:194301, May 2008.

[SFK+06] H. J. Schöpe, A.B. Fontecha, H. König, J.M. Hueso, and R. Biehl. Fast microscopic method for large scale determination of structure, morphology, and quality of thin colloidal crystals. *Langmuir*, 22(4):1828–1838, January 2006.

[SGA+09] L.M. Stadler, C. Gutt, T. Autenrieth, O. Leupold, S. Rehbein, Y. Chushkin, and G. Grbel. Fourier transform holography in the context of coherent diffraction imaging with hard x-rays. *physica status solidi (a)*, 206(8):1846–1849, 2009.

[Sha95] S.D. Shastri. *X-ray polarization optics and coherent nuclear resonance scattering using synchrotron radiation*. Cornell University, January, 1995.

[SHE03] J. Smajic, C. Hafner, and D. Erni. Design and optimization of an achromatic photonic crystal bend. *Opt. Express*, 11(12):1378–1384, June 2003.

[Sin12] A. Singer. *Coherence properties of third and fourth generation x-ray sources*. PhD thesis, University of Hamburg, 2012.

[SKP+05] C. G. Schroer, O. Kurapova, J. Patommel, P. Boye, J. Feldkamp, B. Lengeler, M. Burghammer, C. Riekel, L. Vincze, A. van der Hart, and M. Küchler. Hard x-ray nanoprobe based on refractive x-ray lenses. *Applied Physics Letters*, 87(12):124103, 2005.

[SLJF03] M. Soljačić, C. Luo, J.D. Joannopoulos, and S. Fan. Nonlinear photonic crystal microdevices for optical integration. *Opt. Lett.*, 28(8):637–639, April 2003.

[SSY00] E.L. Saldin, E.V. Schneidmiller, and V. Yurkov. *The Physics of Free Electron Lasers*. Advanced Texts in Physics. Springer, 2000.

[SSY+10] A.S. Salasyuk, A.V. Scherbakov, D.R. Yakovlev, A.V. Akimov, A.A. Kaplyanskii, S.F. Kaplan, S.A. Grudinkin, A.V. Nashchekin, A.B. Pevtsov, V.G. Golubev, T. Berstermann, C. Brüggemann, M. Bombeck,

and M. Bayer. Filtering of elastic waves by opal-based hypersonic crystal. *Nano Letters*, 10(4):1319–1323, 2010.

[ST07] B.E.A. Saleh and M.C. Teich. *Fundamentals of photonics*. Wiley series in pure and applied optics. Wiley-Interscience, 2007.

[Sta09] F. Staier. *Entwicklung, Bau und Test einer UHV Röntgenstreukammer für die digitale In-Line Holographie*. PhD thesis, Universität Heidelberg, 2009.

[TDM+08] P. Thibault, M. Dierolf, A. Menzel, O. Bunk, C. David, and F. Pfeiffer. High-Resolution Scanning X-ray Diffraction Microscopy. *Science*, 321(5887):379–382, 2008.

[TEJ+06] P. Thibault, V. Elser, C. Jacobsen, D. Shapiro, and D. Sayre. Reconstruction of a yeast cell from x-ray diffraction data. *Acta Cryst.*, A62(4):248–261, 2006.

[TGM06] E.L. Thomas, T. Gorishnyy, and M. Maldovan. Phononics: Colloidal crystals go hypersonic. *Nat Mater*, 5(10):773–774, October 2006.

[TNT+09] Y. Takahashi, Y. Nishino, R. Tsutsumi, et al. High-resolution diffraction microscopy using the plane-wave field of a nearly diffraction limited focused x-ray beam. *Phys. Rev. B*, 80(5):054103, 2009.

[TZN+10] Y. Takahashi, N. Zettsu, Y. Nishino, et al. Three-dimensional electron density mapping of shape-controlled nanoparticle by focused hard x-ray diffraction microscopy. *Nano Letters*, 10(5):1922–1926, 2010.

[UK83] E.E. Uzgiris and R.D. Kornberg. Two-dimensional crystallization technique for imaging macromolecules, with application to antigen-antibody-complement complexes. *Nature*, 301(5896):125–129, January 1983.

[VAB+00] Y.A. Vlasov, V.N. Astratov, A.V. Baryshev, A.A. Kaplyanskii, O.Z. Karimov, and M.F. Limonov. Manifestation of intrinsic defects in optical properties of self-organized opal photonic crystals. *Phys. Rev. E*, 61:5784–5793, May 2000.

[VBSN01] Y.A. Vlasov, X.Z. Bo, J.C. Sturm, and D.J. Norris. On-chip natural assembly of silicon photonic bandgap crystals. *Nature*, 414(6861):289–293, 2001.

[Ver95] H. Versmold. Neutron diffraction from shear ordered colloidal dispersions. *Phys. Rev. Lett.*, 75(4):763–766, July 1995.

[VJLL97] O. D. Velev, T. A. Jede, R. F. Lobo, and A. M. Lenhoff. Porous silica via colloidal crystallization. *Nature*, 389(6650):447–448, Oct 1997.

[VR01a] I.A. Vartanyants and I.K. Robinson. Partial coherence effects on the imaging of small crystals using coherent x-ray diffraction. *Journal of Physics: Condensed Matter*, 13:10593–10611(19), 2001.

[VR01b] I.A. Vartanyants and I.K. Robinson. Partial coherence effects on the imaging of small crystals using coherent x-ray diffraction. *J. Phys.: Condens. Matter*, 13(47):10593–10611, 2001.

[VR03] I.A. Vartanyants and I.K. Robinson. Imaging of quantum array structures with coherent and partially coherent diffraction. *Journal of Synchrotron Radiation*, 10(Pt 6):409–415, 2003.

[vSHP+11] M.M. van Schooneveld, J. Hilhorst, A.V. Petukhov, T. Tyliszczak, J. Wang, B.M. Weckhuysen, F.M.F. de Groot, and E. de Smit. Scanning transmission x-ray microscopy as a novel tool to probe colloidal and photonic crystals. *Small*, 7(6):804–811, 2011.

[VvB94] N.A.M. Verhaegh and A. van Blaaderen. Dispersions of rhodamine-labeled silica spheres: Synthesis, characterization, and fluorescence confocal scanning laser microscopy. *Langmuir*, 10(5):1427–1438, 1994.

[VZM+08] I. A. Vartanyants, A. V. Zozulya, K. Mundboth, O. M. Yefanov, M.-I. Richard, E. Wintersberger, J. Stangl, A. Diaz, C. Mocuta, T. H. Metzger, G. Bauer, T. Boeck, and M. Schmidbauer. Crystal truncation planes revealed by three-dimensional reconstruction of reciprocal space. *Phys. Rev. B*, 77:115317, March 2008.

[War90] B. E. Warren. *X-ray Diffraction*. Dover Publ. Inc, 1990.

[WE64] R. S. Wagner and W. C. Ellis. Vapor-liquid-solid mechanism of single crystal growth. *Applied Physics Letters*, 4(5):89–90, 1964.

[WHF05] M.M. Woolfson and F. Hai-Fu. *Physical and Non-Physical Methods of Solving Crystal Structures*. Cambridge University Press, 2005.

[WHP+08] G.J. Williams, E. Hanssen, A.G. Peele, M.A. Pfeifer, J. Clark, B. Abbey, G. Cadenazzi, M. D. de Jonge, S. Vogt, L. Tilley, and K.A. Nugent. High-resolution x-ray imaging of plasmodium falciparum-infected red blood cells. *Cytometry Part A*, 73A(10):949–957, 2008.

[WMW+07] M. Wellhöfer, M. Martins, W. Wurth, A.A. Sorokin, and M. Richter. Performance of the monochromator beamline at flash. *Journal of Optics A: Pure and Applied Optics*, 9(7):749, 2007.

[WV98] J.E.G.J. Wijnhoven and W.L. Vos. Preparation of photonic crystals made of air spheres in titania. *Science*, 281(5378):802–804, 1998.

[XFE] Adapted from the European XFEL website. (www.XFEL.eu).

[You07] T. Young. *A course of lectures on natural philosophy and the mechanical arts*. Number Bd. 1 in A Course of Lectures on Natural Philosophy and the Mechanical Arts. Johnson, 1807.

[YSM01] V. Yannopapas, N. Stefanou, and A. Modinos. Effect of stacking faults on the optical properties of inverted opals. *Phys. Rev. Lett.*, 86:4811–4814, May 2001.

Danksagung

Am Ende möchte ich den vielen Menschen danken, die mir bei dieser Arbeit geholfen und dazu beigetragen haben.

Meinem Betreuer, Prof. Dr. Edgar Weckert, möchte ich ganz besonders für die Vergabe dieses aktuellen Promotionsthemas, die vielen Diskussionen und die wertvollen Anregungen danken. Trotz größerer Aufgaben im Rahmen des Direktoriums vom DESY hatte er immer ein offenes Ohr für mein Anliegen und war selbst an so manchem Abend oder Wochenende für Diskussion über `MOLTRANS` verfügbar.

Prof. Dr. Ivan Vartaniants gilt mein herzlicher Dank für viele wissenschaftliche Diskussionen, die gemeinsame Planung und Durchführung der Experimente. Seine rigorose Art und Weise war nicht immer einfach aber nach einer Eingewöhnungszeit eine gute Motivation. Nicht zu vergessen sind auch seine persöhnlichen Einsätze bei den Messzeiten. Außerdem danke ich Prof. Dr. Henry Chapman für die Übernahme der Gutachterrolle bei der Disputation.

Die Experimente sind nur möglich geworden durch die großartige Mitarbeit der Wissenschaftler an den Beamlines ID06, ID13 und der alten ID15 am ESRF, sowie an P10 von PETRA III. Namentlich sind hier vorallem Anatoly Snigirev und Michael Sprung zu erwähnen.

Die Kolloidkristalle wurden im Van't Hoff Labor in Utrecht in der Gruppe von Prof. Andrei Petukhov gezüchtet. Aus dieser Arbeitsgruppe möchte ich Janne-Mieke Meijer danken fr die professionellen Gespräche und die gute Zusammenarbeit bei den Messungen.

Sehr viel habe ich von meinen Kollegen Dr. Adrian Mancuso und Dr. Oleksander Yefanov gelernt, welche mir vor allem viele Tipps und Tricks im Umgang mit experimentellen Daten vermittelt haben. Oleksander war auch Mitten in der Nacht immer bereit Fragen über verschiedene Kristallstrukturen zu beantworten.

Mein besonderer Dank gilt Andrej Singer, welcher mit seiner eigenen Promotion mir in den vergangenen Jahren, erst ein sehr guter Kollege, und in zwischen ein Freund geworden ist. In den vielen konstruktiven Gesprächen im gemeinsamen Büro sind häufig nützliche Ideen entsanden.

Des weiteren möchte ich Sebastian Rücker für die penible Korrektur meines Englisch danken.

Ganz herzlicher Dank gilt auch meiner Frau, meinen Eltern und der ganzen Familie, welche mich in der Zeit immer wohlwollend unterstützt haben.